EXPERIMENTAL AND MASS BALANCE CONSTRAINTS ON NEAR-SURFACE MARINE IODINE REDOX TRANSFORMATIONS

By

Alexi Schnur

A DISSERTATION

Submitted to
Michigan State University
in partial fulfillment of the requirements
for the degree of

Earth and Environmental Sciences – Doctor of Philosophy

2025

ABSTRACT

The distribution of marine iodine is closely linked to the cycling of oxygen (O_2), and its concentration in oxygenated waters has implications for ozone (O_3) destruction as part of a paleoredox proxy. While the distribution of iodine's major redox species, iodide (I^-) and iodate (IO_3^-), in the surface ocean is well-documented, the rates and mechanisms of I^- oxidation to IO_3^- remain less well-understood. Iodate in ocean waters is incorporated and preserved within marine carbonate minerals, tracing past and present redox processes and past oxygenation. Iodide formed by microbial reduction of IO_3^- in surface waters destroys O_3 and has implications for modeling of climatological cycles. Iodate reduction is thought to occur fairly quickly and leads to a disequilibrium in $[I^-]$ in surface waters, but *in situ* I^- oxidation to IO_3^- is thought to be slow and may only occur in "hotspots" of large biological influence. Due to these slow reported timescales of I^- oxidation, *ex situ* sources of movement, such as upwelling and water mass mixing may have a larger impact on iodine redox species' distribution that has been previously thought.

To calculate rates of I^- oxidation to IO_3^- and quantitatively constrain their distribution, I used three distinct techniques: 1) incubation experiments using the radiotracer ^{129}I, 2) an iodine mass balance of Pacific basin waters, and 3) an Optimum Multi-parameter Analysis (OMPA) across two field areas, 1) the Bermuda Atlantic Time Series (BATS) in the Sargasso Sea and 2) the Pacific Ocean basin at 152°W from Alaska to the Antarctic Ocean, measuring concentrations of iodine's major redox species I^- and IO_3^-, as well as some intermediates. Samples were collected as part of monthly BATS cruises in the Atlantic and as part of two GEOTRACES cruises (GP15 and GP17-OCE) across the Pacific basin.

In the first study, I tested addition of the reactive oxygen species (ROS) superoxide (O_2^-) and hydrogen peroxide (H_2O_2) in their role in iodine redox transformations through shipboard radio tracers incubations under ambient conditions as part of the Bermuda Atlantic Time Series (BATS). Incubation trials evaluated the effects of biology, light, and the presence and absence of ROS on I^- oxidation over time and at both euphotic and sub-photic depths. I calculated rates of I^- oxidation through use of the radiotracer $^{129}I^-$ ($t_{1/2}$ ~57 Mya) added to all incubations, quantified through measurement of incubations' $^{129}I/^{127}I$ ratios of individual iodine species determined using Neptune high-resolution multi-collector ICP-MS (MC-ICP-MS). Rates of I^- oxidation were found to be sluggish and under the influence of additionally occurring redox transformations, highlighting limited change in iodine redox chemistry associated with *in situ* processes.

In studies two and three, I measured iodine redox species concentrations in surface and depth profile samples from the GEOTRACES GP15 (2018) and GP17-OCE (2022) cruise transects to complete the first iodine meridional transect of the Pacific Ocean. Together with complimentary tracers (^{7}Be), I performed mass balance calculations quantifying the contributions of iodine species from *ex situ* sources in the Pacific. In addition, a water mass analysis using GP17-OCE hydrographic data provides insight into the eight water masses present in the South Pacific study region and the physical versus biogeochemical changes that contribute to iodine's distribution throughout the Pacific basin. Ultimately, my data highlight multiple mechanisms likely responsible for iodine cycling and evolution on a basin scale, with important implications for iodine's broader use as a paleoredox tracer.

This dissertation is dedicated to my parents, Eric Schnur and Jill McFellin-Schnur, for their patience, love, and unconditional support throughout my entire life.

ACKNOWLEDGEMENTS

As I began my PhD in May 2019, I had no idea the journey that it would take me on or the incredible people that I would come to know because of my time at MSU. I am thankful to each and every one of them and hope that their collective influence on my life can be summed up here in some small way.

I first want to acknowledge and thank my advisor, Dr. Dalton Hardisty, for his confidence in me, and for granting me this opportunity to become a better and more knowledgeable scientist and academic. Thank you for your encouragement and your time, from weekly meetings to conference dinners, that always led to interesting introductions, deeper discussions, and improved research questions. I am so appreciative of your willingness to provide thoughtful feedback and insight on any research question, big or small, and teaching me how to see five steps further than I ever could before. Thank you especially for your understanding in hard times and helping find avenues to shift that allowed me to reach my goals. I am glad that I could be part of helping grow your new lab.

Thank you also to the remaining members of my committee; Dr. Matthew Schrenk, Dr. Seth Jacobson, and Dr. Elena Litchman, for their guidance and support with my research and during my time at MSU. Matt, thank you for your moral support in some of my hardest times; I truly am grateful that you lent me your ear and your advice. Thank you also for the use of your lab and your student office in the Hardisty lab's early days – getting things set up in Giltner would have been much more difficult without the second "home" you provided for us. Seth, thank you for your always genuine care and critical questions that kept my research on track. Elena, although we have never been able to meet in person, I feel as though we are close in many ways! Thank you for taking a chance on a "remote" student, and for always providing a very practical perspective to research questions. I hope for the best in your return to MSU and the years ahead.

Thank you also to the best lab manager ever (this will remain undisputed): Todd Lydic. Thank you for your many hours in the clean lab running up and troubleshooting instruments, and the (seemingly hundred) texts of relief when my standard curves finished through without issue. Thank you for making sure we had the supplies we needed for our experiments, and for always being the most joyful person to work with. Your contributions to my work and the Hardisty lab cannot go understated.

I want to extend a heartfelt thank you to my good friends and lab-mates in the Hardisty lab; Dr. Keyi Cheng and Ms. Kirsten Fentzke, MSc. Keyi, we started the journey to our PhD's together in 2019, and I can't imagine a better person to have had at my side through the ups and downs of academia and the world throughout our years at MSU. I have learned so much from you over the years, and consider you a very dear friend. I am so excited to see where your journey takes you, and I know that you are going to have an amazing time in Victoria (even if you have to work with IC!). I can't thank you enough for all the support in life and research you have given me, and I hope that I managed to return the favor by at least 50%. I will at least always remember to try to never "fly the pigeon". Kirsten, we may have only worked together for 2.5 years, but it feels like I've known you for a lifetime. Thank you for our many lunches and talks, you never fail to make each day so much brighter.

A special thank you to Dr. Osama Alian, for all of our coffee talks and your "Alexi checks"; supporting me especially when I didn't know how to support myself. I certainly wouldn't be here without your encouragement and advice. I am always wishing the best for you in everything you do.

I also want to acknowledge the many wonderful people throughout the department who have been my friends and colleagues throughout the years: Dr. Jana Burke (and Mark!), Dr. Lindsay Putman, Brent Heerspink, Gabriel Nathan, Jackson Barnes, and Jenna Hynes (now at Cornell). Thank you for all the grad school knowledge, career advice, and dining hall lunches. My time at MSU would be much less full for not knowing each of you.

Thank you to my parents, Eric and Jill Schnur, for the unwavering and unconditional support, love, and advice they have given me throughout my entire life, but especially throughout the last six years. There are not enough words in the world to express how grateful I am to you, but I will try to show it to you every day of my life. Thank you for everything. I love you both so much.

Deep appreciation must be said to my family and the many friends in my "real life" who have gone on this journey with me and experienced its ups and downs second-hand. To my brother Nick, thank you for listening and supporting me, even when you think the things I do are nuts. To all of my extended family: yes, I promise I'm finally finished with school! To my friends throughout all aspects of my life, thank you for sticking it out with me. I am so excited to see where the next adventure takes us.

Lastly, I need to thank my 22-toed fur-son, FitzWilliam the orange tabby cat. Thank you for sleeping by my side every night, making sure that we both never miss breakfast, and going on many a crazy trek with me. I know that the last years have been difficult, but you have been my little rock every step of the way.

I am so grateful to have had the opportunity to further my studies at MSU and to contribute meaningful, new research to the world of science. This work was possible only through the support of so many, and I cannot express enough how grateful I am for being so loved. I am so excited for the next adventure in science and beyond.

TABLE OF CONTENTS

LIST OF SYMBOLS

[x]	Concentration of x
~	About
Δ	Change in

LIST OF ABBREVIATIONS

O_3	Ozone
I^-	Iodide
ROS	Reactive Oxygen Species
$O_2^{\bullet -}$	Superoxide
H_2O_2	Hydrogen Peroxide
BATS	Bermuda Atlantic Time Series
IO_3^-	Iodate
HOI	Hypoiodous Acid
I_2	Elemental iodine
$CaCO_3$	Calcium Carbonate
Mn^{2+}	Manganese cation
O_2	Oxygen
$t_{1/2}$	Half-life
^{129}I	Iodine-129
^{127}I	Iodine-127
nM	Nanomolar (10^{-9})
µM	Micromolar (10^{-6})
ADT	Atlantic Daylight Time (UTC-3)
µm	Micrometer (10^{-6})
SOD	Superoxide dismutase
SOTS	Superoxide thermal source
DMSO	Dimethyl sulfoxide
kU	Kilo-unit
$MnCl_2$	Manganese chloride
MCLA	Methyl cypridina luciferin analog
ASFW	Aged filtered seawater
DTPA	Diethylene-triaminepentaacetic acid
USW	Unfiltered seawater
pM	Picomolar (10^{-12})
KI	Potassium iodide
H_3NSO_3	Sulfamic Acid
nm	Nanometer (10^{-9})
I_3^-	Triiodide
ICP-MS	Inductively-coupled plasma mass spectrometer
MC-ICP-MS	Multi-collector inductively-coupled plasma mass spectrometer
DOI	Dissolved organic iodine
HCl	Hydrochloric acid
$NaHSO_3$	Sodium Bisulfate
TMAH	Tetramethyl ammonium hydroxide
TEA	Tetraethyl ammonium
KIO_3^-	Potassium iodate
TQ	Triple quad (referring to ICP-MS)
SQ	Single quad (referring to ICP-MS)
ppb	Parts per billion (10^{-9})
M	Molar

HNO_3	Nitric Acid
In	Indium
Rh	Rhodium
Cs	Cesium
µg	Microgram (10^{-6})
WHOI	Woods Hole Oceanographic Institute
Ar	Argon
Te	Tellurium
µL	Microliter (10^{-6})
V	Volt
CTD	Device that measures water conductivity, temperature, and depth
CDOM	Colored dissolved organic matter
UV	Ultraviolet
k_{SOTS}	Rate constant of SOTS
NO_x	Nitrogen Oxides
OH	Hydroxide
DOM	Dissolved organic matter
IO_2^-	Iodine dioxide
Br	Bromine
N_2O	Nitrous oxide
Fe	Iron
ODZ	Oxygen deficient zone
OMPA	Optimum Multiparameter Analysis

INTRODUCTION

An understanding of the distribution of iodine and its major redox species throughout the world's oceans is important for constraining uncertainty in climatological ozone models and has many uses as important implications for a paleoredox proxy. Iodine is also an important factor in human and environmental health, and an appreciation of its dispersal throughout the world oceans has a great impact on how this trace element is understood as it is employed for ecological benefits. Iodine speciation flux between marine surface waters and the atmosphere can have a significant effect on climatological O_3 models. Specifically, iodide (I^-) is a large destructor of tropospheric ozone (O_3) Carpenter et al., 2013, Luhar et al., 2017). Iodate (IO_3^-) is reduced by many organisms to I^-, especially in warm surface ocean waters (Bluhm et al., 2010, Chance et al., 2014, Farrenkopf and Luther 2002). Iodide is also used by microorganisms such as kelp as an antioxidant (Küpper et al., 2008), in order to keep these organisms healthy. Iodine in food contributes to overall human health through creation of thyroid hormones that assist in proper development and growth (Zimmermann 2011, Sorrenti et al 2021).

Despite its significant roles in the global environment, climate, as well as human health, the processes governing marine iodine cycling require further understanding. Specifically, current constraints on the drivers of processes that lead to the observed spatial variability of iodine speciation in surface seawater is limited. For example, despite a growing understanding of the first-order distribution of marine iodine speciation, the rates and mechanisms of iodine oxidation and reduction in the surface ocean yet remain unknown, hindering our full understanding of the importance of iodine to the applications listed above.

Profiles outlining the concentrations of I^- and IO_3^- in the surface ocean with depth and latitude are well known, and vary spatially, although differently, through the water column and across space in the surface ocean. Total dissolved iodine concentrations throughout the worlds' oceans is found to be generally constant at about 450-500 nM (Chance et al., 2014). Almost ubiquitously, concentrations of I^- in the surface ocean are found at levels of around 250 nM, and I^-'s concentration decreases with depth to nearly zero in the deep ocean. Concentrations of IO_3^- in the water column directly oppose that of I^-, starting a bit higher in well-oxygenated surface waters (around 300-350 nM) and increasing with depth to around 450 nM. At depth, iodine is nearly completely IO_3^- (Figure 1).

Iodine speciation is also known to vary predictably across distance with latitude. At low latitudes concentrations of I^- are found to be higher in surface waters than at higher latitudes, likely because of the rapid reduction of IO_3^- to I^- by high abundances of bacteria and phytoplankton near the equator (Hepach et al., 2010, Chance et al., 2014). Such I^- enrichment is also prominent in near-shore areas (Figure 2). Conversely, IO_3^- concentrations are found to be higher in surface waters at higher latitudes (in arctic/antarctic waters), where upwelling of IO_3^--rich bottom waters bring large amounts of IO_3^- to surface waters (Bluhm et al., 2011).

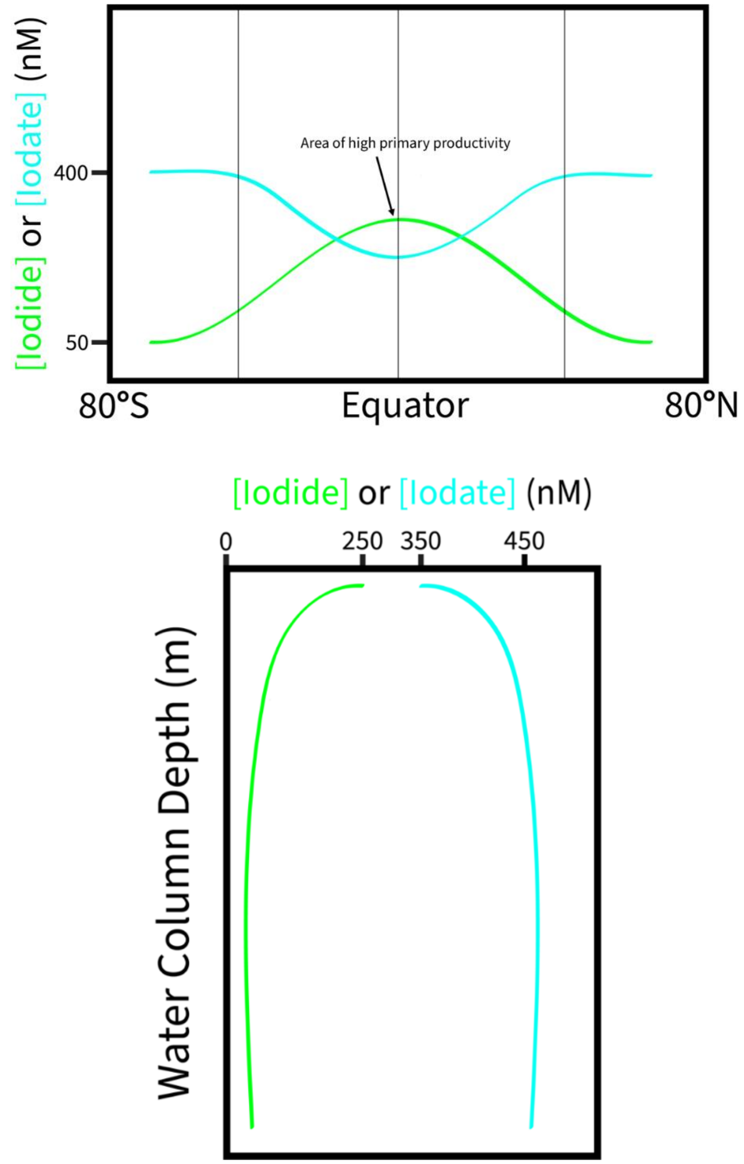

Figure 1 Simplified diagram of iodine redox species iodide (I^-) and iodate (IO_3^-) over A) latitude and B) depth in the water column. Green lines represent iodide and blue lines represent iodate.

The profiles outlining the concentrations of I^- and IO_3^- in the surface ocean over latitude and at depth are well known, however, the rates and mechanisms of *in situ* iodine oxidation and reduction remain unclear. Specifically, the aforementioned enrichment of I^- at high abundances at the expense of oxidized IO_3^- in global euphotic zones emphasized the thermodynamic disequilibrium between redox and iodine speciation, as it is the reduced iodine form. Importantly, the oxidation of I^- to IO_3^- has yet to be observed *in situ* in natural seawater, meaning, the accompanying rates, mechanisms, suspected oxidants, and the role of biology (if any) in I^- oxidation have not yet been established.

The long residence time of I^- at the sea surface is consistent with thermodynamic predictions that O_2 does not oxidize I^-, and that a stronger oxidant is needed for I^- oxidation to IO_3^- in these settings (Li et al., 2014). Strong oxidants such as superoxide (O_2^-) and hydrogen peroxide (H_2O_2), produced extracellularly by marine bacteria and phytoplankton (Sutherland et al. 2019, Li et al., 2012, Diaz et al., 2013) are thought to have impacts on this oxidation, indicating that a biological influence may be beneficial for I^- oxidation to occur. As yet, experiments assessing the potential for I^- oxidation in natural marine waters with intrinsic concentrations of reactive oxygen species (ROS) are limited, and most studies of I^- oxidation are hindered by the difficulty of tracking what are likely particularly slow rates.

In combination with slow rates of I^- oxidation, the accumulation of I^- at the sea surface is likely facilitated by phytoplankton. Phytoplankton both directly reduces IO_3^- to I^- as well as assimilates both IO_3^- and I^-, which is released to the water column during cell senescence or organic matter remineralization (Bluhm et al., 2010, Hepach et al., 2020). I^- assimilation has also been linked to the use of I^- as an antioxidant by marine bacteria and kelp (Küpper et al., 2008). Despite this productivity link, the meridional trends of I^- accumulation at the sea surface have not been directly linked to corresponding trends in biological productivity. Measurements of iodine speciation along transects of varying primary productivity in euphotic waters may aid in elucidating the role that biology plays in the accumulation of I^- at the sea surface, as well as its role in I^- oxidation. Importantly, given likely slow oxidation rates of the accumulated I^- from biological reduction (Chance et al., 2014), *ex situ* processes such as water mass transport and benthic inputs likely redistribute I^- and may likewise contribute to an increase in I^- concentrations in the surface ocean via semi-conservative mixing processes.

In this dissertation, I have addressed four specific problems related to the rates and mechanisms of iodine redox reactions and its distribution in euphotic seawaters across latitudes and depth, as well as the formation and movement of those water masses themselves, in two specific research areas – a spot point on the Bermuda Atlantic Time Series (BATS) in the Sargasso Sea and a latitudinal tract at 152°W, from Alaska to Antarctic waters across the entire open water Pacific basin from involvement in the GEOTRACES GP15 and GP17-OCE cruises (Figure 3). A time-series was conducted at BATS to determine the role of reactive oxygen species on I^- oxidation to IO_3^- using ^{129}I as a radiotracer to track rates of oxidation through measurement of $^{129}I/^{127}I$ ratios (Hardisty et al., 2020, 2021). In addition to the first full transect measurements of surface $[I^-]$ and $[IO_3^-]$ of the Pacific Ocean, both a mass balance and water mass analysis of the Southern Pacific Ocean were completed using shipboard hydrographic nutrients. Surface and depth profiles of IO_3^- and measurements of ^7Be from the GP17-OCE were used to calculated rates of upwelling and vertical diffusion, as well as an extended Optimum Multi-parameter Analysis (OMPA) with the additional nutrient IO_3^- used to attempt to track water mass movement. Rates of iodine redox transformation were constrained through a novel mass-balance approach to calculate the influence of *ex situ* parameters on iodine distribution in the surface ocean. The four specific problems assessed are:

Q1. What role do the reactive oxygen species superoxide (O_2^-) and hydrogen peroxide (H_2O_2) play in *in situ* oxidation of I^- to IO_3^-? (BATS)

Q2. Do rates of I^- oxidation and IO_3^- reduction vary with latitude? (GP17-OCE)

Q3. What is the relationship between primary productivity and sea surface iodine speciation? (BATS, GP17-OCE)

Q4. Do *ex-situ* processes such as seasonal mixing, water mass formation and transport, and benthic inputs contribute to trends of high surface I^- distribution? (GP15/GP17-OCE)

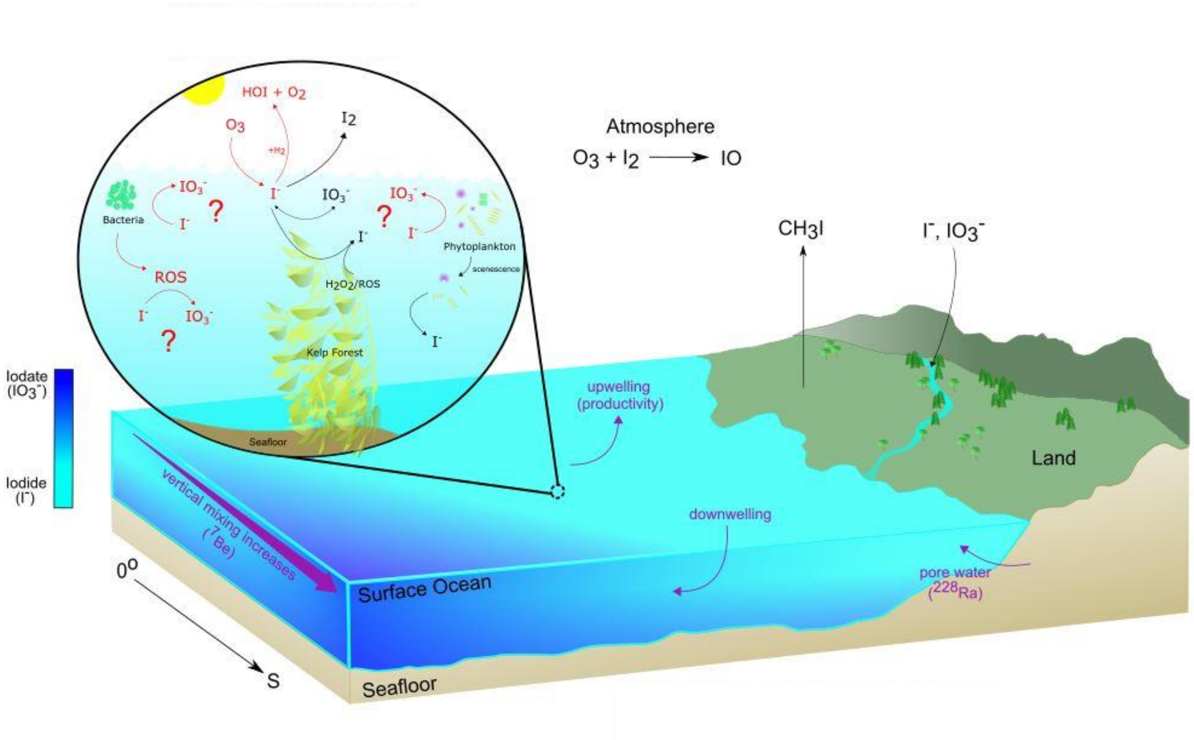

Figure 2 The Iodine cycle in the surface ocean. Inset with red text and arrows denote possible mechanisms of *in situ* iodine redox reactions in the surface ocean, possibly facilitated by biological processes. Large scale ocean with purple text and arrows denote mass balance and whole-ocean constraints possible for *ex situ* drivers of iodine distribution. Black text indicates portions of the iodine cycle not directly measured as part of this dissertation.

Knowledge on sources and distribution of I^- at the sea surface is key for a better understanding of surface ocean iodine's impact on O_3 destruction and to more accurately inform global climatological models (Macdonald et al., 2014, Ganzeveld et al., 2009, Helmig et al., 2012). Iodide in the surface ocean reacts with and destroys tropospheric ozone (O_3), releasing hypoiodious acid (HOI) and I_2 to the atmosphere (Carpenter et al., 2013, Hepach et al., 2020), which quickly photolyze to I atoms that react with O_3 to form IO (Carpenter et al., 2013), and is eventually recycled back to the ocean (Figure 2). Iodide in the sea surface is a significant O_3 sink and accounts for about one-third of the total global O_3 dry deposition flux (600-1000 Tg O_3) per year, with an accompanying flux on the order of 10^{12} per year of iodine from the surface ocean to the atmosphere (Chance et al., 2014). The reaction of O_3 with I^- at the sea surface and iodine's recycling back to the ocean occurs through two key reaction sequences

1. $H^+ + I^- + O_3 \longrightarrow HOI + O_2$

2. $H^+ + HOI + I^- \longleftrightarrow I_2 + H_2O$

and is thought to account for around 75% of observed iodine oxide (IO) levels over the Atlantic Ocean (Carpenter et al., 2013).

The majority of iodine that is present in the surface ocean is found as one of its two most abundant redox species: the reduced I^- or oxidized IO_3^-. In much of the open ocean water column, I^- concentrations are found to be inversely correlated with those of IO_3^-. However, I^- is consistently found at the ocean's oxygenated surface to be present in larger than "expected" amounts (~250 nM). Laboratory studies show that IO_3^- reduction to I^- is linked to primary production (Bluhm et al., 2010, Hepach et al., 2020, Moisan et al., 1994, Chance et al., 2007, Councell et al., 1996), however, the rates and mechanisms of I^- oxidation to IO_3^- remain unclear.

Radioactive ^{129}I ($t_{1/2}$ ~57 Mya) is found naturally in sea water at extremely low levels and is produced by breakdown of Xe by cosmic rays in the atmosphere and fission of ^{238}U in the Earth's crust (He et al., 2013, García-Toraño et al., 2018). It is also produced anthropogenically at higher levels as discharge in heavy water from nuclear power plants (Liu et al., 2016). Although waters near these discharge areas are slightly enriched in ^{129}I, [^{127}I] is still orders of magnitude higher than that of [^{129}I], making it useful as a radiotracer for oxygenation in natural seawater samples in an incubation time study. With ^{129}I added as I^- to incubation samples containing ROS, it is possible to compare *in situ* rates of IO_3^- oxidation in surface seawater containing these oxidants. If $^{129}I/^{127}I$ ratios are seen to increase, it can be known that I^- was oxidized to IO_3^- in the samples. Iodide oxidation has been shown to occur in artificial seawater mediums (Li et al., 2012, Li et al., 2014), and in acid solutions (Bray and Liebhafsky, 1931), but information on the rates and mechanisms of I^- oxidation in true seawater is lacking. Given likely very slow rates of I^- oxidation, and the known disequilibrium found in euphotic surface seawater where I^- is found in concentrations higher than expected, it is likely that stronger oxidants, such as superoxide (O_2^-) and its reduced product, hydrogen peroxide (H_2O_2), are important factors needed for the oxidation of I^-, even in well-oxygenated waters.

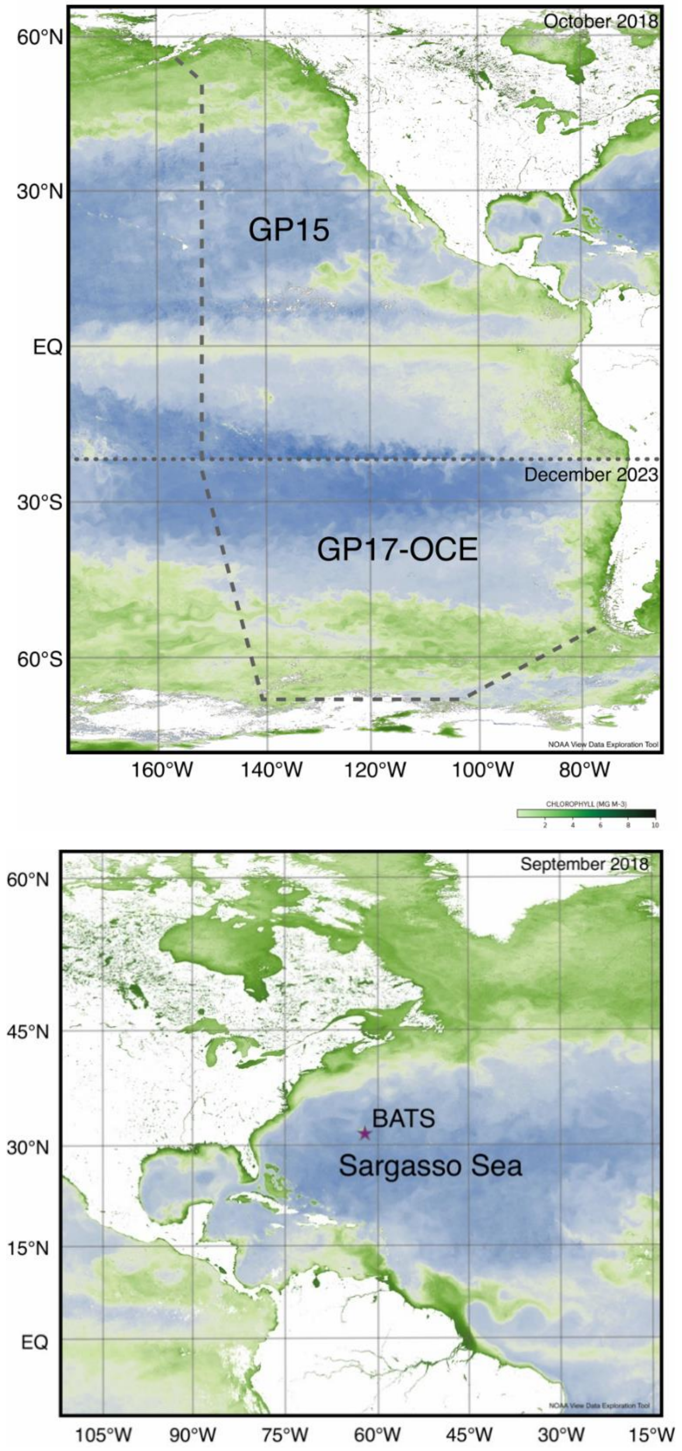

Figure 3 Map of sampling locations for A) Bermuda Atlantic Time Series (BATS) incubation and B) GEOTRACES GP15 and GP17-OCE mass balance and OMPA analyses. Note that BATS sampling occurred at BATS and Hydrostation S sampling sites (covered by purple star), while GEOTRACES cruises each had many sampling sites (GP15 – 54 FISH, GP17-OCE – 53 FISH, 38 stations) and general cruise tracks are outlined by gray dotted line.

Superoxide and hydrogen peroxide are known to be produced extracellularly by phytoplankton through the reduction of O_2 outside the cell (Sutherland et al., 2019, Diaz et al., 2013, Li et al., 2014). In addition, the presence of H_2O_2 and O_2^- produced by bacteria has been shown to oxidize I^- to I_3^- and I_2 (Li et al., 2014, Wong et al., 2008). Experiments that assess the potential for these strong oxidants to impact I^- oxidation at the sea surface are hindered by the difficulty of tracking slow rates of I^- oxidation. The unique insights illuminated here from incubation data from the 2018 BATS cruise (Chapter 1) provide a guide for future work over a larger ocean transect to determine the facility of ROS in the iodine cycle, where potentially slow rates of I^- oxidation can be elucidated.

It is likely that areas of high primary productivity, may be "hotspots" of *in situ* IO_3^- production. Iodate accumulates to higher than average levels in these areas (Chance et al., 2014), and is subsequently distributed by *ex situ* sources of water movement such as upwelling and water mass mixing. The combination of these *in situ* hotspots of formation and *ex situ* methods of distribution may lead to those trends in iodine redox species distribution that are well documented and are vetted again with the samples measured in this study.

In near-surface, oxygenated, euphotic waters, I^- concentrations increase towards the equator, while IO_3^- concentrations tend to decrease (Figure 1). As this trend is exacerbated in near-shore waters where rates of primary production are high, it is likely that the role of biology in iodine redox transformations is larger than previously thought. Within compiled data of this trend, the Pacific has been historically under-characterized. Data from GEOTRACES GP15 and GP17-OCE completed a full Pacific transect of iodine measurements, for a full understanding of this trend across varying gradients of primary productivity (Figure 2). The GP17-OCE cruise also provided data on the "essential parameter" ^{7}Be, whose vertical profile is a function of vertical mixing and which could share key similarities to euphotic I^- in open ocean waters. With measurements of ^{7}Be, seasonal mixing in ocean waters was traced through calculation of vertical mixing and upwelling rates (Kadko 2017, Haskell et al., 2015, Kadko and Prospero, 2011). These vertical mixing and upwelling rates are necessary for a mass balance approach to calculate the influence of *ex situ* parameters on iodine distribution in the surface ocean.

In addition to the extracellular production of strong oxidants that may aid in I^- oxidation, bacteria and phytoplankton are known to intracellularly reduce IO_3^- to I^- in culture (Hepach et al., 2020, Moisan et al., 1994, Bluhm et al., 2010, Chance et al., 2007, Councell et al., 1996). Like the opposite oxidation reaction, the mechanisms for this reduction are not well known. Although previously suggested as responsible for IO_3^- reduction, recent studies have shown IO_3^- reduction by these species even when nitrate is not a limiting factor (Hepach et al., 2020) or when nitrate reductase is deactivated (Waite and Truesdale 2003). Depletion of IO_3^- in vertical profiles has also been suggested to be caused by bacteria's uptake of IO_3^-. During logarithmic growth, IO_3^- uptake has been shown to exceed I^- production, leading to a deficit or a case of "missing iodine" (Hepach et al., 2020) in the iodine mass balance. During senescence, this I^- is finally released back into the water column. Hepach et al., 2020 indicates a lag between high primary production and I^- "production", or release into surrounding waters. Determination of the level of influence of primary production on the iodine mass balance is paramount to constraining current observed trends of I^- distribution. No study has directly compared rates of Net Community Production along a transect to that of iodine speciation to determine the potential role of productivity in regulating meridional iodine trends (e.g. Jansen et al., 2020). GP17-OCE has provided that opportunity and allowed for a direct comparison of iodine species' distribution in the open ocean with known rates of primary production and export production across large gradients

In combination with *in situ* parameters of I^- oxidation, *ex situ* processes such as seasonal mixing, water mass formation and movement and benthic inputs from upwelling to coastal systems may contribute to observed surface I^- concentrations (Figure 2). Seasonal mixing rates towards higher latitudes and near the poles tend to be greater than in equatorial systems (Oka et al., 2007). Therefore, the residence time of euphotic I^- at lower latitudes can be shown to be longer than in the less-stratified polar waters. Together, the measurement of IO_3^- and use of ^{7}Be-determined upwelling rates has allowed for quantification of *ex situ* contributions to I^- distribution patterns at the sea surface through a mass balance approach, and a deeper insight into *ex situ* processes driving well-known meridional iodine distribution trends.

The formation, influence, and movement of water masses of the Southern Pacific Ocean can also be tracked using hydrographic data recorded shipboard from the GP17-OCE cruise and an extended Optimum Multi-parameter Analysis (eOMPA). Eight water masses were found to have been transversed by GP17-OCE along the "latitudinal" (at 152°W) and "longitudinal" (at 67°S) sections of its transect. All major water masses encountered were analyzed for relative contribution to the Southern Ocean environment by calculation through pyOMPA. The formation and movement of these water masses throughout the South Pacific has major implications for the *ex situ* methods of nutrient and trace metal distribution, including that of iodine species in the Southern Ocean.

GP17-OCE traveled from Papeete, Tahiti south to the ice edge in the Western Amudsen Sea, then crossing to Punta Arenas, Chile for sampling of TEI's (Figure 2). Input from geochemical "hotspots" such as high primary productivity, oxygen deficient zones (ODZs), and pore waters for most of this transect in the open ocean were few, and vertical mixing, as expected, did show itself to have been the primary control on distribution for IO_3^-, the only iodine redox species measured across depth for this transect.

Both the BATS and GEOTRACES GP15 and GP17-OCE cruises have provided unique and distinct opportunities to advance our understanding of the contributions of *in situ* and *ex situ* processes driving iodine mass balance in surface seawater, along with producing an extensive and well-constrained iodine mass balance in a large ocean basin and record of the contributions of major water masses in the Southern Pacific Ocean, with a focus on three key hypotheses for this dissertation:

1. *In situ* rates of I^- oxidation are directly related to concentrations of strong oxidants in well-oxygenated, photic, near-surface ocean waters
2. *In situ* rates of primary production and related nutrient availability act as the initial driver of euphotic IO_3^-/I^- disequilibrium
3. *Ex situ* processes, including seasonal vertical mixing and upwelling, redistribute iodine species and drive latitudinal trends of iodine distribution

The three chapters discussing these themes here within are presented in manuscript form; the first being published in *Frontiers in Marine Science*, and the second and third moving toward journal selection.

REFERENCES

Bluhm, K., Croot, P., Wuttig, K., & Lochte, K. (2010). Transformation of iodate to iodide in marine phytoplankton driven by cell senescence. *Aquatic Biology*. https://doi.org/10.3354/ab00284

Bluhm, K., Croot, P. L., Huhn, O., Rohardt, G., & Lochte, K. (2011). Distribution of iodide and iodate in the Atlantic sector of the southern ocean during austral summer. *Deep-Sea Research Part II: Topical Studies in Oceanography*. https://doi.org/10.1016/j.dsr2.2011.02.002

Carpenter, L. J., Chance, R. J., Sherwen, T., Adams, T. J., Ball, S. M., Evans, M. J., Hepach, H., Hollis, L. D. J., Hughes, C., Jickells, T. D., Mahajan, A., Stevens, D. P., Tinel, L., & Wadley, M. R. (2021). Marine iodine emissions in a changing world. *Proceedings of the Royal Society A*, *477*(2247). https://doi.org/10.1098/RSPA.2020.0824

Carpenter, L. J., MacDonald, S. M., Shaw, M. D., Kumar, R., Saunders, R. W., Parthipan, R., Wilson, J., & Plane, J. M. C. (2013). Atmospheric iodine levels influenced by sea surface emissions of inorganic iodine. *Nature Geoscience*. https://doi.org/10.1038/ngeo1687

Chance, R., Baker, A. R., Carpenter, L., & Jickells, T. D. (2014). The distribution of iodide at the sea surface. In *Environmental Sciences: Processes and Impacts*. https://doi.org/10.1039/c4em00139g

Chance, R., Malin, G., Jickells, T., & Baker, A. R. (2007). Reduction of iodate to iodide by cold water diatom cultures. *Marine Chemistry*. https://doi.org/10.1016/j.marchem.2006.06.008

Councell, T. B., Landa, E. R., & Lovley, D. R. (1997). Microbial reduction of iodate. *Water, Air, and Soil Pollution*. https://doi.org/10.1023/A:1018370423790

Diaz, J. M., Hansel, C. M., Voelker, B. M., Mendes, C. M., Andeer, P. F., & Zhang, T. (2013). Widespread production of extracellular superoxide by heterotrophic bacteria. *Science*, *340*(6137), 1223–1226. https://doi.org/10.1126/science.1237331

Farrenkopf, A. M., & Luther, G. W. (2002). Iodine chemistry reflects productivity and denitrification in the Arabian Sea: Evidence for flux of dissolved species from sediments of western India into the OMZ. *Deep-Sea Research Part II: Topical Studies in Oceanography*. https://doi.org/10.1016/S0967-0645(02)00038-3

Ganzeveld, L., Helmig, D., Fairall, C. W., Hare, J., & Pozzer, A. (2009). Atmosphere-ocean ozone exchange: A global modeling study of biogeochemical, atmospheric, and waterside turbulence dependencies. *Global Biogeochemical Cycles*. https://doi.org/10.1029/2008GB003301

García-Toraño, E., Altzitzoglou, T., Auerbach, P., Bé, M. M., Bobin, C., Cassette, P., Chartier, F., Dersch, R., Fernández, M., Isnard, H., Kossert, K., Lourenço, V., Nähle, O., Nonell, A., Peyrés, V., Pommé, S., Rozkov, A., Sánchez-Cabezudo, A., & Sochorová, J. (2018). The half-life of 129I. *Applied Radiation and Isotopes*, *140*. https://doi.org/10.1016/j.apradiso.2018.06.007

Hardisty, D. S., Horner, T. J., Wankel, S. D., Blusztajn, J., & Nielsen, S. G. (2020). Experimental observations of marine iodide oxidation using a novel sparge-interface MC-ICP-MS technique. *Chemical Geology*. https://doi.org/10.1016/j.chemgeo.2019.119360

Hardisty, D. S., Horner, T. J., Evans, N., Moriyasu, R., Babbin, A. R., Wankel, S. D., Moffett, J. W., & Nielsen, S. G. (2021). Limited iodate reduction in shipboard seawater incubations from the Eastern Tropical North Pacific oxygen deficient zone. *Earth and Planetary Science Letters*, *554*, 116676. https://doi.org/10.1016/j.epsl.2020.116676

Haskell, W. Z., Kadko, D., Hammond, D. E., Knapp, A. N., Prokopenko, M. G., Berelson, W. M., & Capone, D. G. (2015). Upwelling velocity and eddy diffusivity from 7Be measurements used to compare vertical nutrient flux to export POC flux in the Eastern Tropical South Pacific. *Marine Chemistry*, *168*, 140–150. https://doi.org/10.1016/j.marchem.2014.10.004

He, P., Hou, X., Aldahan, A., Possnert, G., & Yi, P. (2013). Iodine isotopes species fingerprinting environmental conditions in surface water along the northeastern Atlantic Ocean. *Scientific Reports 2013 3:1*, *3*(1), 1–8. https://doi.org/10.1038/srep02685

Hepach, H., Hughes, C., Hogg, K., Collings, S., & Chance, R. (2020). Senescence as the main driver of iodide release from a diverse range of marine phytoplankton. *Biogeosciences*. https://doi.org/10.5194/bg-17-2453-2020

Helmig, D., Lang, E. K., Bariteau, L., Boylan, P., Fairall, C. W., Ganzeveld, L., Hare, J. E., Hueber, J., & Pallandt, M. (2012). Atmosphere-ocean ozone fluxes during the TexAQS 2006, STRATUS 2006, GOMECC 2007, GasEx 2008, and AMMA 2008 cruises. *Journal of Geophysical Research Atmospheres*. https://doi.org/10.1029/2011JD015955

Kadko, D. (2017). Upwelling and primary production during the U.S. GEOTRACES East Pacific Zonal Transect. *Global Biogeochemical Cycles*. https://doi.org/10.1002/2016GB005554

Küpper, F. C., Carpenter, L. J., McFiggans, G. B., Palmer, C. J., Waite, T. J., Boneberg, E.-M., Woitsch, S., Weiller, M., Abela, R., Grolimund, D., Potin, P., Butler, A., Luther, G. W., Kroneck, P. M. H., Meyer-Klaucke, W., & Feiters, M. C. (2008). Iodide accumulation provides kelp with an inorganic antioxidant impacting atmospheric chemistry. *Proceedings of the National Academy of Sciences*. https://doi.org/10.1073/pnas.0709959105

Li, H. P., Daniel, B., Creeley, D., Grandbois, R., Zhang, S., Xu, C., Ho, Y. F., Schwehr, K. A., Kaplan, D. I., Santschi, P. H., Hansel, C. M., & Yeager, C. M. (2014). Superoxide production by a manganese-oxidizing bacterium facilitates iodide oxidation. *Applied and Environmental Microbiology*. https://doi.org/10.1128/AEM.00400-14

Li, H. P., Yeager, C. M., Brinkmeyer, R., Zhang, S., Ho, Y. F., Xu, C., Jones, W. L., Schwehr, K. A., Otosaka, S., Roberts, K. A., Kaplan, D. I., & Santschi, P. H. (2012). Bacterial production of organic acids enhances H2O 2-dependent iodide oxidation. *Environmental Science and Technology*. https://doi.org/10.1021/es203683v

Liu, D., Hou, X., Du, J., Zhang, L., & Zhou, W. (2016). 129I and its species in the East China Sea: Level, distribution, sources and tracing water masses exchange and movement. *Scientific Reports*, *6*. https://doi.org/10.1038/srep36611

Luhar, A. K., Galbally, I. E., Woodhouse, M. T., & Thatcher, M. (2017). An improved parameterisation of ozone dry deposition to the ocean and its impact in a global climate-chemistry model. *Atmospheric Chemistry and Physics*. https://doi.org/10.5194/acp-17-3749-2017

Macdonald, S. M., Gómez Martín, J. C., Chance, R., Warriner, S., Saiz-Lopez, A., Carpenter, L. J., & Plane, J. M. C. (2014). A laboratory characterisation of inorganic iodine emissions from the sea surface: Dependence on oceanic variables and parameterisation for global modelling. *Atmospheric Chemistry and Physics*. https://doi.org/10.5194/acp-14-5841-2014

Moisan, T. A., Dunstan, W. M., Udomkit, A., & Wong, G. T. F. (1994). THE UPTAKE OF IODATE BY MARINE PHYTOPLANKTON. *Journal of Phycology*. https://doi.org/10.1111/j.0022-3646.1994.00580.x

Oka, E., Talley, L. D., & Suga, T. (2007). Temporal variability of winter mixed layer in the mid-to high-latitude North Pacific. *Journal of Oceanography*, *63*(2). https://doi.org/10.1007/s10872-007-0029-2

Sorrenti, S., Baldini, E., Pironi, D., Lauro, A., D'orazi, V., Tartaglia, F., Tripodi, D., Lori, E., Gagliardi, F., Praticò, M., Illuminati, G., D'andrea, V., Palumbo, P., & Ulisse, S. (2021). Iodine: Its role in thyroid hormone biosynthesis and beyond. In *Nutrients* (Vol. 13, Issue 12). https://doi.org/10.3390/nu13124469

Sutherland, K. M., Wankel, S. D., & Hansel, C. M. (2020). Dark biological superoxide production as a significant flux and sink of marine dissolved oxygen. *Proceedings of the National Academy of Sciences of the United States of America*. https://doi.org/10.1073/pnas.1912313117

Wadley, M. R., Stevens, D. P., Jickells, T. D., Hughes, C., Chance, R., Hepach, H., Tinel, L., & Carpenter, L. J. (2020). A Global Model for Iodine Speciation in the Upper Ocean. *Global Biogeochemical Cycles*, *34*(9), e2019GB006467. https://doi.org/10.1029/2019GB006467

Wong, G. T. F., & Zhang, L. S. (2008). The kinetics of the reactions between iodide and hydrogen peroxide in seawater. *Marine Chemistry*. https://doi.org/10.1016/j.marchem.2007.04.007

Zimmermann, M. B. (2011). The role of iodine in human growth and development. In *Seminars in Cell and Developmental Biology* (Vol. 22, Issue 6). https://doi.org/10.1016/j.semcdb.2011.07.009

CHAPTER 1: RATES AND PATHWAYS OF IODINE SPECIATION TRANSFORMATIONS AT THE BERMUDA ATLANTIC TIME SERIES

1.1: Abstract

The distribution of iodine in the surface ocean – of which iodide-iodine is a large destructor of tropospheric ozone (O_3) – can be attributed to both *in situ* (i.e., biological) and *ex situ* (i.e., mixing) drivers. Currently, uncertainty regarding the rates and mechanisms of iodide (I^-) oxidation render it difficult to distinguish the importance of *in situ* reactions vs *ex situ* mixing in driving iodine's distribution, thus leading to uncertainty in climatological ozone atmospheric models. It has been hypothesized that reactive oxygen species (ROS), such as superoxide ($O_2^{\bullet -}$) or hydrogen peroxide (H_2O_2), may be needed for I^- oxidation to occur at the sea surface, but this has yet to be demonstrated in natural marine waters. To test the role of ROS in iodine redox transformations, shipboard isotope tracer incubations were conducted as part of the Bermuda Atlantic Time Series (BATS) in the Sargasso Sea in September of 2018. Incubation trials evaluated the effects of ROS ($O_2^{\bullet -}$, H_2O_2) on iodine redox transformations over time and at euphotic and sub-photic depths. Rates of I^- oxidation were assessed using a $^{129}I^-$ tracer ($t_{1/2}$ ~15.7 Myr) added to all incubations, and $^{129}I/^{127}I$ ratios of individual iodine species (I^-, IO_3^-). Our results show a lack of I^- oxidation to IO_3^- within the resolution of our tracer approach – i.e., <2.99 nM/day, or <1091.4 nM/yr. In addition, we present new ROS data from BATS and compare our iodine speciation profiles to that from two previous studies conducted at BATS, which demonstrate long-term iodine stability. These results indicate that *ex situ* processes, such as vertical mixing, may play an important role in broader iodine species' distribution in this and similar regions.

1.2: Introduction

Iodine is a redox-sensitive element that is found ubiquitously in the surface ocean at an average concentration of about 450 nM (Elderfield and Truesdale, 1980; Chance et al., 2014; Moriyasu et al., 2023). Knowledge of the distribution of iodine's two major redox species – iodide (I^-) and iodate (IO_3^-) – at the sea surface is important for our understanding of iodine's role in atmospheric cycles through the destruction of ozone (O_3) by I^-, a significant O_3 sink (Carpenter et al., 2013; Chance et al., 2014; Luhar et al., 2017). The destruction of O_3 by $I^{\bullet}$ releases hypoiodous acid (HOI) and I_2 to the atmosphere, which photolyzes to I atoms and continues to break down atmospheric O_3 (Carpenter et al., 2013). An understanding of the rates and mechanisms that contribute to the distribution of I^- and IO_3^- at the sea surface can aid in our understanding of tropospheric O_3 destruction and its importance in the cycles of global climate change and impact on air quality.

In well-oxygenated portions of the open ocean, IO_3^- is found at levels exceeding 250 nM at the surface, increasing in concentration with depth in sub-photic waters (>350 nM). In much of the open ocean water column, I^- concentrations are found to be inversely correlated with [IO_3^-]; however, I^- is consistently found to be present in larger amounts (up to 250 nM) than would be expected if O_2 were the direct oxidant of I^- in fully oxygenated surface waters (Chance et al., 2014). Indeed, O_2 is not thermodynamically favored to fully oxidize I^- to IO_3^- and the oxidant responsible for the reaction is unknown (Luther et al., 1995; Luther, 2023). Given multiple known pathways of IO_3^- reduction, it is clear however that I^- oxidation is occurring within marine waters but is likely sluggish (1.5-560 nM/yr) (Campos et al., 1996; Edwards and Truesdale, 1997; Truesdale et al., 2001b; Žic and Branica, 2006; He et al., 2013; Hardisty et al., 2020; Hughes et al., 2021). For example, *in situ* reduction of IO_3^- to I^- by phytoplankton and bacteria is known to be a major pathway through which I^- accumulates in areas of generally high primary productivity, such as upwelling zones and along coasts (Bluhm et al., 2010). Some iodine may be assimilated and later released during cell senescence (Hepach et al., 2020) and may account for “missing iodine” that is found in mass balance calculations of these areas.

The extracellular production of reactive oxygen species (ROS) by oxygenic photo- and heterotrophic bacteria promotes a variety of cell functions (Hansel and Diaz, 2021) and may also aid in the oxidation of I^- in surface waters. Extracellular $O_2^{\bullet-}$ production by these bacteria varies as a function of species, where it ranges from 0.1-3.7 amol cell^{-1} h^{-1} (heterotrophs) to 4.3-13,400 amol cell^{-1} h^{-1} (oxygenic phototrophs) (Diaz et al., 2013; Sutherland et al., 2020). Similarly, bacteria and phytoplankton are also sources of H_2O_2 to the marine environment, both through the secretion of intracellular pools and extracellular production. Extracellular $O_2^{\bullet-}$ production by Roseobacter sp. AzwK-3b – 15-20% of coastal bacterial communities (Bond et al., 2020) – was shown in cell cultures to promote I^- oxidation in the absence of Mn^{2+}, which is preferentially oxidized (Li et al., 2014; Hansel et al., 2019) (Figure 1.1). Oxidation is thought to be completed extracellularly through the aid of these ROS (Li et al., 2014). This mechanism has yet to be tested under ambient marine conditions.

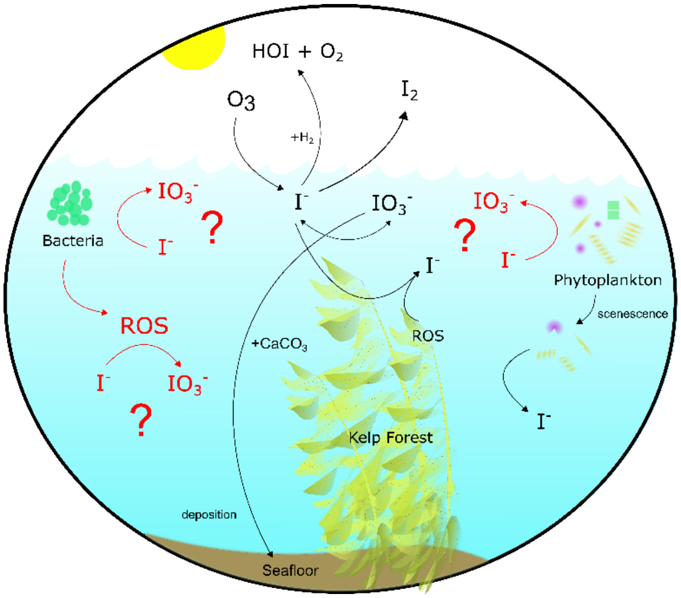

Figure 1.1 Iodine cycling in the modern surface ocean. Processes highlighted in red were examined in this study.

Here, we performed shipboard ^{129}I radiotracer incubations under ambient seawater conditions to investigate the role of ROS in I$^-$ oxidation processes at the Bermuda Atlantic Time Series (BATS) in September 2018. ^{129}I has a half-life of ~15.7 Ma and is therefore useful as a tracer on timescales of decades or less (Hardisty et al., 2020; Hardisty et al., 2021). To build on previous studies, the ROS H$_2$O$_2$ and O$_2^{\bullet-}$ were added to experiments at levels analogous to natural seawater concentrations to investigate their effect on oxidation of I$^-$ to IO$_3^-$, or vice versa. In addition, we have measured iodine speciation and O$_2^{\bullet-}$ in depth profiles from the BATS and the adjacent Hydrostation S. Our iodine speciation is compared to previous measurements from 1993 to 1994 and 1984 to 1985 (Jickells et al., 1988; Campos et al., 1996), thus providing the first long-term intercomparison for marine iodine.

1.3: Methods

1.3.1: Sample Collection

Seawater was collected from the Bermuda Atlantic Time Series (BATS) and Hydrostation S sites in the Sargasso Sea in September 2018. Depth profile investigations at BATS were taken at 32.343°N 64.594°W at 21 separate depths between 1 m and 4500 m. Hydrostation S samples were taken at 32.165°N 64.501°W at 10 depths between 1 m and 500 m. Incubation water was taken from two depths (1 m and 240 m) and collected into four carboys (two euphotic (1 m) and two subphotic (240 m)) between 20:30 and 22:30 ADT. One carboy from each depth was filtered using a 0.2 μm filter to remove bacteria and other biology and particles while another was left unfiltered. ^{129}I ($t_{1/2} \cong 15.7$ My) (Eckert and Ziegler Isotope Products ©) (Hardisty et al., 2020; Hardisty et al., 2021), was added directly to each of the carboys at a targeted concentration of ~70 nM $^{129}I^-$ for investigating iodine redox reactions in natural seawater over time. $^{129}I^-$ was added before aliquoting the carboy water for individual incubations to ensure homogenous $^{129}I^-$ concentrations at t_0 for all incubations. 200 ml from each carboy were fractionated into separated incubation containers. Samples for t_0 were immediately subsampled from spiked incubation containers, with this and subsequent (t_1, t_2, t_f) subsamples being ~50 ml. All subsamples were immediately filtered at 0.2 μm to end interaction with biology after sampling. Subsamples were refrigerated and stored at 4°C until they returned to Michigan State University and were frozen for storage. Campos (1997) showed that seawater samples stored refrigerated (4°C) or frozen (-20°C) did not show signs of degradation in total iodine measurements over a one-to-three-year period – well over the eight-month timeframe in which measurement of these samples began after collection.

1.3.2: Incubation setup

Five incubation factors were used to create 20 incubation trials using a ship-deck light-filtering incubator to mimic at-depth light filtration, cooled with a continuous resupply of ambient surface seawater and stored in translucent and amber high-density polyethylene (HDPE) Nalgene bottles for dark incubations: each done in triplicate (Table 1.1). Factors included: 1) filtering of samples through a 0.2 μm syringe filter, meant as a control to screen filtered seawater of bacteria and macro-organisms and particles, kept in either the light or the dark depending on incubation, (Campos et al., 1996; Farrenkopf et al., 1997; Hardisty et al., 2020); 2) addition of $O_2^{\bullet -}$ dismutase (SOD) to incubations both filtered and unfiltered, but all left in the dark, intended as a control to remove ambient $O_2^{\bullet -}$ in seawater (Li et al., 2012; Diaz et al., 2013; Sutherland et al., 2020); 3) addition of superoxide thermal source (SOTS) or hydrogen peroxide (H_2O_2) to filtered samples kept in the dark in separate experiments, both suspected of being able to aid in oxidation of I^- to IO_3^- in seawater; 4) unfiltered water in the dark to determine the role, if any, of photochemical reactions that may cause the reduction of IO_3^- to I^- in the presence of organic matter (Spokes and Liss, 1996; Chance et al., 2014); 5) additions of $MnCl_2$ to iterations of the above in order to consider the potential of preferential Mn^{2+} oxidation relative to I^-. Note that controls 2 and 5 were only relevant if I^- oxidation was detected in the other controls.

Superoxide thermal source was kept frozen (-80°C) until it was added daily by pipette to incubations 11 and 19 (Table 1.1) as a combination of 1 ml dimethyl sulfoxide (DMSO) +1 mg SOTS (3028 μM SOTS) (Cayman Chemicals, CAS number 223507-96-8) and diluted to 15 μM SOTS within seawater samples, which provides ≥25 nM $O_2^{\bullet-}$ at the surface water temperatures at BATS and Hydrostation S (Heller and Croot, 2010). This was made fresh daily immediately before adding to samples and added daily to account for natural decay. The $O_2^{\bullet-}$ concentration of the SOTS stock was not analyzed but $O_2^{\bullet-}$ concentration was analyzed in one experiment a few hours post-SOTS addition – to allow to reach steady state concentrations – to confirm $O_2^{\bullet-}$accumulation. Hydrogen peroxide (30%) was added at a volume targeting 50 nM H_2O_2 in each solution. SOD was added by pipette daily – thus accounting for decay and titration via potentially newly formed $O_2^{\bullet-}$ within the incubations – from a stock concentration of 4 kU/ml to incubations to produce samples with SOD concentration of 0.32 kU/ml. Given potential long oxidation timescales of I^-, all incubations were performed over a 140-hour time period, with subsamples collected for iodine species measurement at t_0, ~t_{40}, ~t_{88}, and ~t_{140} hours.

Depth Zone (1m or 240m)	**Photic**	**Photic**	**Photic**	**Photic**	**Subphotic**	**Subphotic**
Light Condition (Light/Dark)	Light	Dark	Light	Dark	Dark	Dark
Treatment (Filtered/Unfiltered)	Unfiltered	Unfiltered	Filtered	Filtered	Unfiltered	Filtered
Control	#1	**#3**	**#6**	**#8**	**#13**	**#16**
+Superoxide Dismutase (SOD)		#4		#9	#14	#17
+Manganese Chloride ($MnCl_2$)	#2	#5	#7	#10	#15	#18
+Superoxide Thermal Source (SOTS)				**#11**		**#19**
Hydrogen Peroxide (H_2O_2)				**#12**		**#20**

Table 1.1 Factor setup and inclusion for all 20 incubation trials and controls. Photic samples are from 1 m depth, while subphotic samples are from 240 m depth. Filtered samples were filtered through a 0.2 μm filter for removal of bacteria and macroorganisms. Each incubation number consists of 12 samples; four timepoints sampled in triplicate. Bolded sample numbers in table indicate data for those incubations illustrated in this publication.

1.3.3: Analytical Methods

1.3.3.1: Superoxide

The steady-state concentration of $O_2^{\bullet-}$ was determined as previously described with some minor modifications (Sutherland et al., 2020). Water samples were collected using 12 L Ocean Test Equipment bottles on a 24-position Sea-Bird CTD rosette. Samples were transferred into dark, acid washed bottles and measured between 30 minutes and six hours of the collection time. Thirty minutes was chosen as a sample delay period because it is greater than 10 half-lives of

$O_2^{\bullet -}$ in typical marine waters, meaning that any $O_2^{\bullet -}$ remaining is the result of light-independent $O_2^{\bullet -}$ production by microbial communities in the bottles (Roe et al., 2016). Samples collected above the thermocline were incubated on deck with continuously flowing surface water (28.2°C and 29.2°C at Hydrostation S and BATS, respectively) and samples below the thermocline were incubated at 4°C.

Superoxide concentrations were measured using an FeLume Mini (Waterville Analytical) and the $O_2^{\bullet -}$-specific chemiluminescent probe methyl cypridina luciferin analog (MCLA, Santa Cruz Biotechnology, Rose et al., 2008) stored at 4°C. Recent work using these methods has demonstrated that filtration of natural seawater can produce additional $O_2^{\bullet -}$ (Roe et al., 2016). To avoid introducing this bias into sample measurements, we used the following equation:

$$[O_2^{\bullet -}]_{sample} = [O_2^{\bullet -}]_{USW} - [O_2^{\bullet -}]_{AFSW}$$

where $[O_2^{\bullet -}]_{USW}$ represents the measured concentration of $O_2^{\bullet -}$ in unfiltered seawater (USW) and $[O_2^{\bullet -}]_{AFSW}$ represents the concentration of $O_2^{\bullet -}$ in aged (>24 hours) filtered (0.2 µm Sterivex filter) seawater (AFSW) amended with 75 µM diethylene-triaminepentaacetic acid (DTPA) to complex any metals present in the sample. Each measurement consisted of running a 25 mL USW sample through the FeLume system (3 mL/min) for several minutes until a steady signal was recorded. After a steady signal was recorded, 2 µL superoxide dismutase (SOD; Superoxide Dismutase from bovine erythrocytes >3,000 U/mg, Sigma, stock prepared in DI water to 4,000 U/mL) was added to the sample to quench all $O_2^{\bullet -}$ in the sample. The same procedure was followed for the AFSW samples. The reported $O_2^{\bullet -}$ concentrations represent the difference between the USW and the AFSW concentrations, the latter allowing us to eliminate the portion of the measured signal due to MCLA auto-oxidation in each particular sample matrix. Calibration curves were generated daily from three or more paired observations of time-zero $O_2^{\bullet -}$concentration (dependent variable) and chemiluminescence (independent variable) using linear regression. Separate calibration curves were used for each of the two storage temperatures. Because chemiluminescence values were baseline-corrected, regression lines were forced through the origin. Calibrations yielded highly linear curves (typically $R^2 > 0.9$), with a typical sensitivity of one chemiluminescence unit per pM $O_2^{\bullet -}$.

1.3.3.2: Spectrophotometry

Iodate was measured using the spectrophotometric method outlined in Jickells et al. (1988), using 10% potassium iodide (KI) solution and 1.5 M sulfamic acid (H_3NSO_3). 10% KI was made fresh daily. Samples were measured using a VWR UV-Vis Scanning 3100 PC spectrophotometer and accompanying UV-Vis Analyst software using VWR® Two-Sided Disposable Plastic Cuvettes for measurements within the visible range (300-900 nm), path length 10 mm. Fisherbrand® Semi-Micro Quartz Cuvettes (Cat. No. 14-958-126) for wavelengths 200-2500 nm, were used for repeated measurements of samples 3.5 years after the initial IO_3^- measurements, with similar results obtained.

Jickells' (1988) method of IO_3^- reaction with excess I^- in acidic conditions yields triiodide (I_3^-) and is specific to IO_3^- (Jickells et al., 1988; Moriyasu et al., 2020; Moriyasu et al., 2023). Triiodide in reacted samples was measured at a ~320 nm trough, with the lowest point being found between 300 and 350 nm, peak at 350 nm, and secondary trough at 400 nm ($A(IO_3^-)_x$). The concentrations of IO_3^- ($nMIO_3^-$) were calculated from these values using the equation:

$$nM_{IO_3-} = A(IO_3^-)_{350} - ((A(IO_3^-)_{\sim 320} + A(IO_3^-)_{400})/2) * m_{standard\ curve}$$

where $m_{standard\ curve}$ is the value of the slope of the standard curve created with potassium iodate (KIO_3^-), calculated between zero and 500 nM KIO_3^- and calibrated using standard additions of KIO_3^- to seawater.

1.3.3.3: Ion Chromatography

We used a previously established ion-exchange chromatography method (Wong and Brewer, 1977; Hou et al., 1999; Hou et al., 2001; Hou et al., 2007; Hou et al., 2009; Hardisty et al., 2020; Hardisty et al., 2021; Moriyasu et al., 2023) to separate I^-, IO_3^-, and DOI from natural seawater samples. Iodide fractions were measured via ICP-MS for I^- concentrations (see section 1.3.3.4) since yields are known to reach ~100% (Hardisty et al., 2020), and then subsequently measured for $^{129}I/^{127}I$ ratios via MC-ICP-MS (see section 1.3.3.5). Previous IO_3^- yields have been found to commonly be between 90-95% (Hou et al., 1999; Hou et al., 2001; Hou et al., 2007; Hou et al., 2009), thus, IO_3^- and DOI fractions were only measured for $^{129}I/^{127}I$ ratios and not used to quantify concentrations from ICP-MS. Spot-checks on IO_3^- fractions were completed on ICP-MS to test reproducibility between spectrophotometric and ICP-MS measurements, with 82 to >100% agreement between methods for $[IO_3^-]$ measured (Table 1.2). Glass columns used for iodine redox species separation were packed with PYREX glass wool and 1 ml (volumetric) AG1-X8 resin that was cleaned of any residual iodine after packing using one full ion-exchange chromatography "cleaning" procedure (substituting sample for 18.2 MΩ-cm water) before samples were run through columns for collection of iodine redox species using the same chromatography procedure.

About 10 ml of each sample – which was quantified gravimetrically before addition – were used during each procedure.

The ion chromatography procedure specifically elutes I^- from the seawater matrix. Iodate and DOI were independently separated prior to the I^- elution step. The DOI and IO_3^- fractions were then reduced to I^- using concentrated hydrochloric acid (HCl) and 0.3 M sodium bisulfite ($NaHSO_3$) at pH <2 (Hou et al., 1999; Hou et al., 2009; Reifenhaüser and Heumann, 1990; Hardisty et al., 2020). Samples were left overnight and then run through ion exchange chromatography columns the next day, using the same I^- elution procedure described above in an eluent of 18% TMAH/2 M HNO_3. Like the samples, the eluent mass was determined gravimetrically, which together were used for determining concentrations, when relevant. The eluent was then directly diluted for measurement via ICP-MS and/or MC-ICP-MS.

For quality control, a 200 ppb I^- solution diluted from a 1000 ± 4 ug/ml I^- solution in 1% tetraethyl ammonium (TEA) (I^-, DOI) or KIO_3^- (IO_3^-) standard was run alongside samples through columns as a monitor of iodine elution efficiency from columns to estimate yields. At least two 18.2 MΩ-cm water blanks were also run as monitors of contamination with sample sets. At least one sample replicate was also included in each column set for assessment of reproducibility between column runs.

1.3.3.4: ICP-MS

[$^{127}I^-$] was measured by a Thermoscientific iCap triple-quad inductively coupled plasma mass spectrometer (ICP-MS-TQ) using Qtegra software version 2.10.3324.131 in both single-quad (SQ) and triple-quad (TQ) mode with O_2 reaction cell gas. A Teledyne ASX 520 autosampler was used to deliver liquid solution to the ICP-MS. Samples analyzed by ICP-MS were diluted 1:20 or 1:40 in a 0.9% tetramethyl ammonium hydroxide (TMAH)/0.1 M nitric acid (HNO_3) or 0.45% TMAH/0.05 M HNO_3 solution, respectively. The same dilutions were used for ICP-MS rinse solutions. Data was corrected relative to the internal standards In, Rh, and Cs. Internal standards used were from Inorganic Ventures© – In was a 1001 ± 3 ug/ml solution in 2% HNO_3; Rh was a 999 ± 5 ug/ml solution in 15% HCl; and Cs was a 1000 ± 4 ug/ml solution in 0.1% HNO – to create a 5 ppb internal standard solution that was spiked into each measured sample directly or using an inline mixing chamber. The ^{127}I standard used for creating standard curves and column standard samples was a 1000 ± 4 ug/ml I^- solution in 1% tetraethylammonium (TEA).

1.3.3.5: MC-ICP-MS ratios ($^{129}I/^{127}I$)

Iodine isotope ratios ($^{129}I/^{127}I$) were measured at Woods Hole Oceanographic Institution (WHOI) via a ThermoFinnegan Neptune MC-ICP-MS according to Hardisty et al. (2020). Specific ion beams mass/charge (m/z) were monitored for Te (126, 128, 130) and Xe (126, 128, 129, 130, 131, 132) isotopes, as well as ^{132}Ba and ^{127}I and ^{129}I in faraday cups L3-L1 and H1-H3 with m/z 129 in the center position. Tuning was completed before running samples each morning to optimize beam intensity. A 500 ppb Te solution (Inorganic Ventures©) was used to account for mass bias corrections. Corrections needed for isobaric interferences were tracked via ^{131}Xe.

We utilized a gas-based "sparge" method for iodine sample introduction and desolvation with a 300 uL/min quartz nebulizer for Ar carrier gas Te solution introduction, using a regular sample cone and x-type skimmer cone (Hardisty et al., 2020; Hardisty et al., 2021). 30 ml Teflon vials, outfitted with pre-formed "sparge caps" that allowed for Ar gas flow through the sample, held ≤6 ml sample (solution containing fractions representing I^-, DOI, or IO_3^-). Teflon vials used for running samples were cleaned before use with each sample in 50% nitric acid for >3 hours at 90°C, then rinsed with 18.2 MΩ-cm water and allowed to air dry in hood until next use. Teflon tubing connecting samples to the Neptune intake were changed regularly to inhibit cross-contamination between sample runs. Before connection to the torch, Ar gas flow rate was decreased to ~0.1 L min^{-1} and Ar was run through the connected sample for one minute to purge air out of the sample container before connecting to the torch. After the sample was connected to the torch, the gas rate was increased to ~1.2 L min^{-1}. Te signal was monitored for stabilization, increasing to a value of 3-7 V. The sample run was started after Te signal stabilized, and then 4 ml concentrated 70% HNO_3 was added upstream of the sample vial to induce volatilization of iodine samples. The sum of nitric and iodine eluent was kept <10 ml to allow for headspace to prevent bubbling over, which can inadvertently introduce liquid upstream of the sample vial, preventing sample measurement. Data were corrected as described in Hardisty et al. (2020), for a final $^{129}I/^{127}I$ ratio and standard deviation output.

1.4: Results

1.4.1: Iodine speciation and superoxide in depth profiles

Depth profiles of I^- and IO_3^- (nM), $O_2^{\bullet-}$ (pM), temperature (°C), and dissolved oxygen (µM) at BATS and Hydrostation S are detailed in Figure 1.2 and show predictable changes throughout depth of IO_3^- and I^-. The dark, particle-associated superoxide steady-state concentration at BATS and Hydrostation S span 4-720 pM through the water column between 1 m and 4553 m at BATS and Hydrostation S sampling sites. Superoxide concentrations were highest between the surface and 1000 meters and fall within the range of previously reported water column values (Hansard et al., 2010; Rusak et al., 2011; Roe et al., 2016). Temperature and dissolved oxygen values are available from cruise CTD data at http://batsftp.bios.edu/. Depth profiles of I^- and IO_3^- mirror that of previous studies of iodine in an oxygenated seawater, with I^- accumulation in the surface elevated at the expense of IO_3^- and with iodine below the euphotic zone being almost completely IO_3^- except for the bottom water sample at 4500 m which has relatively elevated I^-. We also show I^- and IO_3^- reported from previous studies at BATS which were limited to shallower depths (2500 m) than that studied here (4500 m).

It is notable that there appears to be elevated superoxide concentrations at some intermediate water sample depths (e.g., 500 m). This is somewhat at odds with the expectation that light-independent superoxide production will scale with cell abundance and activity. While we did not measure additional biological parameters that might allow us to interpret these concentrations, it is apparent that elevated superoxide concentration do coincide with significant dissolved oxygen gradients. It is possible that elevated superoxide is either a direct or indirect result of remineralization processes occurring at these depths.

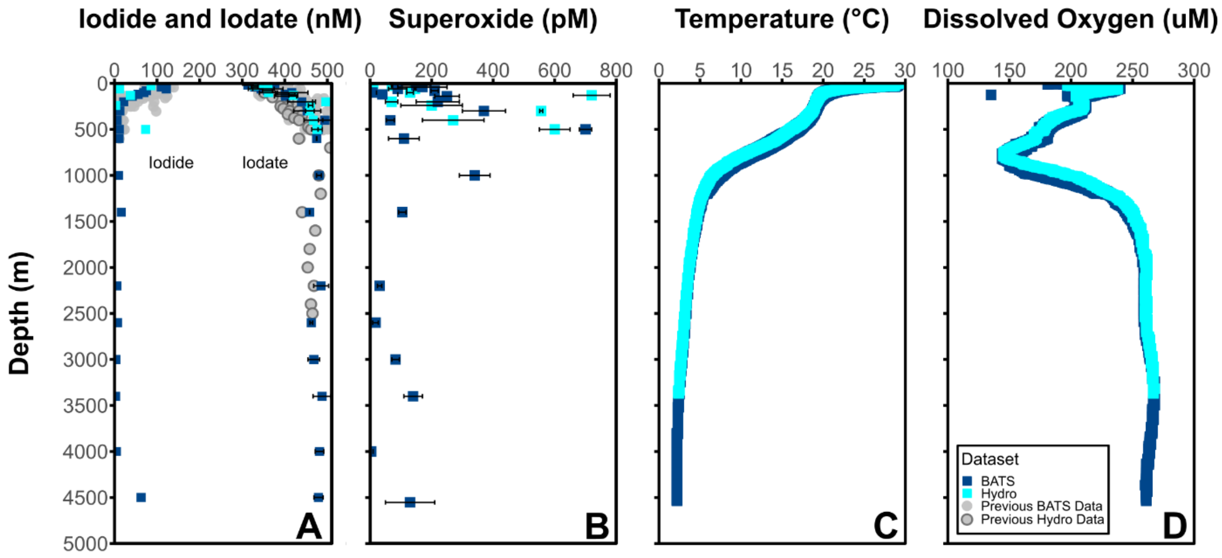

Figure 1.2 Concentrations of A) I^- (left) and IO_3^- (right) (nM) and B) $O_2^{\bullet-}$ (pM) at BATS (blue square) and Hydrostation S (cyan square) stations. Average C) temperature (ºC) and D) dissolved oxygen (µM) from BATS and Hydrostation S stations also included.

1.4.2: Iodine measurements from incubations

In incubation samples, initial [IO_3^-] values measured spectrophotometrically were found to be within the range of 209 nM to 452 nM, while I^- separated from incubation samples via ion-exchange chromatography was found to be in the range of 92 nM to 235 nM from ICP-MS measurements (Table 1.2, Figures 1.3–1.5). Iodate values were spot-checked via exchange chromatography and ICP-MS and were found to be consistent with spectrophotometric measurements but showed a larger standard deviation in most cases, consistent with potential variability in yields (Table 1.2). It is interesting to note that, in some cases, filtered conditions have a lower measured [IO_3^-] than unfiltered conditions (Figure 1.3A, subphotic depth).

Measured [I^-] shows no change over time in any of the incubations investigated (Figures 1.4–1.6). This is also true for [IO_3^-] for most incubation trials; however, IO_3^- values in incubations that included sequential additions of $O_2^{\bullet-}$ (10 nM/24 hrs) and H_2O_2 (50 nM/48 hrs) showed a decrease in [IO_3^-] over time, from 309 nM to 249 nM and 255 nM to 204 nM, respectively. Given an interference causing a baseline shift in these incubations (discussed in Supplementary Information), these samples were corrected for by selecting the minimum trough value between 300 nm and 350 nm for spectrophotometer concentration calculations (section 1.3.3.2) instead of the exact 320 nm value, which was impacted and artificially increased by the interference shift. With correction, a decrease in IO_3^- concentration was still observed. Since there was no corresponding increase in [I^-] or decrease in $^{129}I^-/^{127}I^-$, which would be anticipated for $^{127}IO_3^-$ reduction to I^-, this could indicate reduction of IO_3^- to an iodine intermediate not identified in this study. That said, it more likely reflects interferences from SOTS degradation products which have an overlapping absorbance range with I_3 near 320 nm. Specifically, 4-Formyl Benzoic acid is a degradation product of SOTS-1 (Ingold et al., 1997; Konya et al., 2000; Heller and Croot, 2010) and ROS-induced oxidation products of CDOM have overlapping absorption peaks. Notably, the SOTS degradation products do not account for the same observations made for the same trend observed in H_2O_2 observations. Importantly, we acknowledge that the spectrophotometric IO_3^- measurement is highly prone to interferences (Truesdale, 1978; Luther et al., 1988). Seawater background measurements at 350 nm have the potential to correct these interferences (Hepach et al., 2020; Jones et al., 2023).

Note that the controls with addition of SOD and $MnCl_2$ (meant to test the potential to stop I^- oxidation via scrubbing of superoxide or added preferred electron donor) were only relevant if

I^- oxidation was observed in other controls, so are not considered further. These data are available in Supplementary Table 1.1.

DOI was not a focus of this study but was quantified in some instances for concentration (Table 1.2) as well as for $^{129}I/^{127}I$ ratios in incubations (described in the next section). We note that DOI concentrations in measured incubations (~7.5-9.5% of total dissolved iodine) were larger than we anticipated for open ocean areas where DOI is commonly negligible or uncharacterized (Wong and Cheng, 1998). DOI has previously been found to account for up to 10% of the total iodine pool in coastal areas (Chance et al., 2014).

Incubation	Sample Set	Redox	Timepoint	Spectrophotometry (nM)	ICP-MS (nM)
8	162 (single)	IO_3^-	t0	319 (n=1)	274 ± 42 (n=2)
11	196-198 (average)	IO_3^-	t0	309 ± 32 (n=3)	252 ± 51 (n=3)
11	205-207 (average)	IO_3^-	t_f (142.5 h)	249 ± 8 (n=3)	252 ± 100 (n=3)
12	210 (single)	IO_3^-	t0	255 (n=1)	229 ± 20 (n=2)
12	208-210 (average)	IO_3^-	t0	255 ± 11 (n=3)	229 ± 35 (n=3)
12	217-218, 315 (average)	IO_3^-	t_f (143.25 h)	209 ± 18 (n=3)	233 ± 5 (n=3)
8	162 (single)	DOI	t_0	-	46 ± 3 (n=2)
12	210 (single)	DOI	t_0	-	38 ± 7 (n=2)

Table 1.2 IO_3^- and DOI spot-check measurements compared via spectrophotometry and ICP-MS.

1.4.3: $^{129}I/^{127}I$ isotope ratios

While all incubations were measured for $[IO_3^-]$, we did not measure $^{129}I/^{127}I$ ratios for all incubations. This is because of the lack of variation observed in $^{129}I/^{127}I$ for the targeted ROS and other incubations. Measured $^{129}I/^{127}I$ ratios measured from chosen incubation experiments show no change over time beyond error bars in any of the incubations investigated (Figures 1.3–1.5). This includes IO_3^-, I^-, and DOI. This also includes the $^{129}I/^{127}I$ of I^- in the ROS-based incubations where a decrease in spectrophotometrically quantified $[IO_3^-]$ was observed.

Initial $^{129}I/^{127}I$ ratios were consistent for measured I^- samples, which was expected given that the spike was added to a larger stock volume of seawater that was then aliquoted for the incubations. Average $^{129}I/^{127}I$ ratios for I^- at t_0 ranged from 0.29 ± 0.004 to 0.32 ± 0.002 at the surface. Initial isotope ratios for IO_3^- range from 0.0016 ± 0.0006 to 0.088 ± 0.0005 and 0.0008 ± 0.0001 to 0.002 ± 0.0002 for 1 m (photic) and 240 m (subphotic) depths, respectively, with incubation 8 (photic, dark, filtered) being a slight outlier at 0.07 ± 0.00024. It is notable that ^{129}I was observed in both the DOI and IO_3^- fractions, though it was added as I^-. Initial IO_3^- and DOI values were still predictably quite low, as Hardisty et al. (2020) demonstrated the spike is mostly $^{129}I^-$ with only minor $^{129}IO_3^-$, with the same being expected for DOI. Initial DOI values ranged between 0.005 ± 0.002 and 0.01 ± 0.003, with incubation 8 again being a slight outlier at 0.05 ± 0.004 (Figure 1.4).

1.4.4: Calculating I^- oxidation rates and constraining uncertainty

While oxidation was not observed, we quantified the maximum possible rates that would maintain our time series for $^{129}I/^{127}I$ of IO_3^- within the error (1 s.d.). Maximum daily gross rates of I^-oxidation determined by incubation conditions were calculated using isotope mass balance equations outlined in Hardisty et al. (2020). Average and standard deviation of triplicate initial and final incubation timepoint spectrophotometer measurements of $^{127}[IO_3^-]$, ICP-MS measurements of $^{127}[I^-]$, and MC-ICP-MS measurements of I^- $^{129}I/^{127}I$ ratios and IO_3^- $^{129}I/^{127}I$ ratios were used to first calculate the total IO_3^- created from I^- oxidation in incubations between t_0 to t_{140} (t_{final}). These calculations were then used to determine the rate (nM/day) of I^- oxidation to IO_3^-.

$$R_{iodide_t} = \frac{^{129}\Delta[iodide]_t}{^{127}\Delta[iodide]_t} \qquad \textit{Equation 1.1}$$

$$R_{iodate_t} = \frac{^{129}\Delta[iodide]_t}{^{127}[iodate]_i + {}^{127}\Delta[iodide]_t} \qquad \textit{Equation 1.2}$$

$$\Delta[iodate] = {}^{129}\Delta[iodide]_t + {}^{127}\Delta[iodide]_t \qquad \textit{Equation 1.3}$$

The $^{127}[iodate]_i$ (initial $[IO_3^-]$ pre-spike addition) and the isotope ratios of I^- and IO_3^- at a given time t (R_{iodide_t} and R_{iodate_t}, respectively) are measured (Equations 1.1, 1.2). Since I^- oxidation to IO_3^- is the only quantifiable source of ^{129}I to R_{iodate_t} and negligibly fractionated, we can assume that changes in R_{iodate_t} from ^{129}I and ^{127}I are from I^- oxidation (i.e., Δ[iodate] in Equation 1.3) are contributed at an isotope ratio equivalent to R_{iodide_t} (Equation 1.1). As such, Equation 1.1 can be rearranged to solve for $^{127}\Delta[iodide]_t$ which can be substituted into Equation 1.2 to solve for $^{129}\Delta[iodide]_t$. Plugging $^{129}\Delta[iodide]_t$ into Equation 1.1 then allows to solve for $^{127}\Delta[iodide]_t$ which then can be used in Equation 1.3 to solve for Δ[iodate]. Based on the measured standard deviations of R_{iodide_t}, R_{iodate_t}, $^{127}[iodate]_i$ values and the hours of the incubation, we can then solve for the rate of I^- oxidation to IO_3^- taking place in the incubations in nM/day (Table 1.3).

Incubation	**Incubation Parameters**	**Maximum Rate from averages of first and final timepoints**
3	Photic, dark, unfiltered	0.94 nM/day ± 0.30
8	Photic, dark, filtered	2.99 nM/day ± 0.53
11	Photic, dark, filtered, +SOTS	0.45 nM/day ± 0.28
12	Photic, dark, filtered, +H_2O_2	0.92 nM/day ± 0.24

Table 1.3 Constrained rate measurements of I^- oxidation to IO_3^- in control incubations (incubations 3 and 8) and those with addition of SOTS (incubation 11) and H_2O_2 (incubation 12). Rates could only be calculated for incubations that included all parameters necessary for equations (1.1, 1.2, and 1.3).

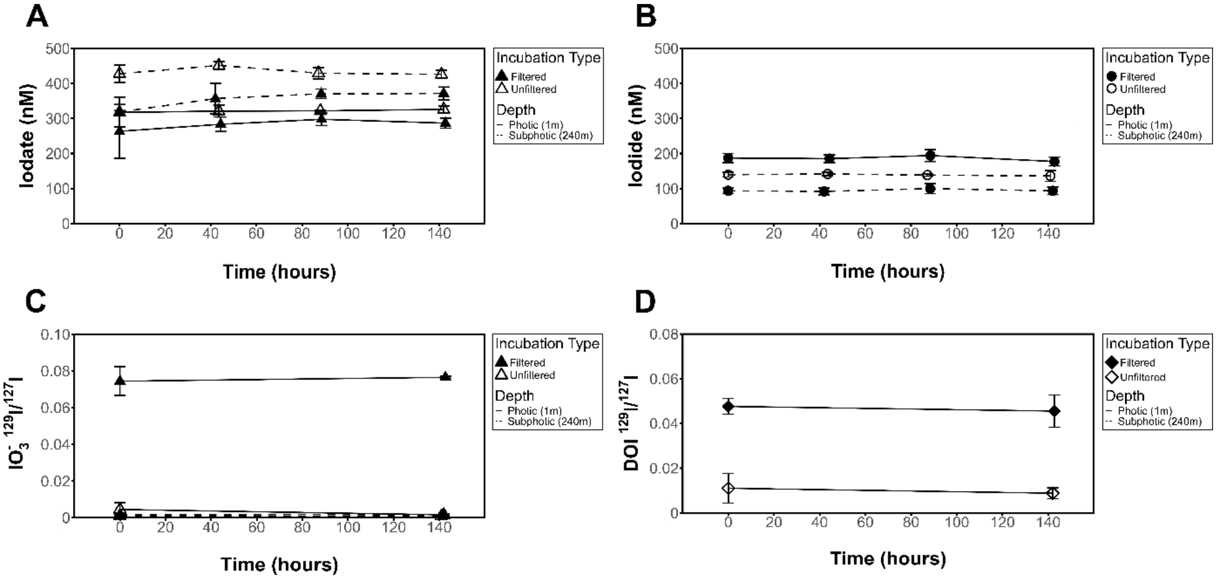

Figure 1.3 Influence of 0.2μm filter on [IO_3^-], [I^-], IO_3^- $^{129}I/^{127}I$ ratios, and DOI $^{129}I/^{127}I$ ratios for dark incubations. No change seen in A) [IO_3^-], B) [I^-], C) $^{129}I/^{127}I$ IO_3^- isotope ratio, or D) $^{129}I/^{127}I$ DOI isotope ratio results in filtered (incubations 8 and 16) or unfiltered (incubations 3 and 13) experiments.

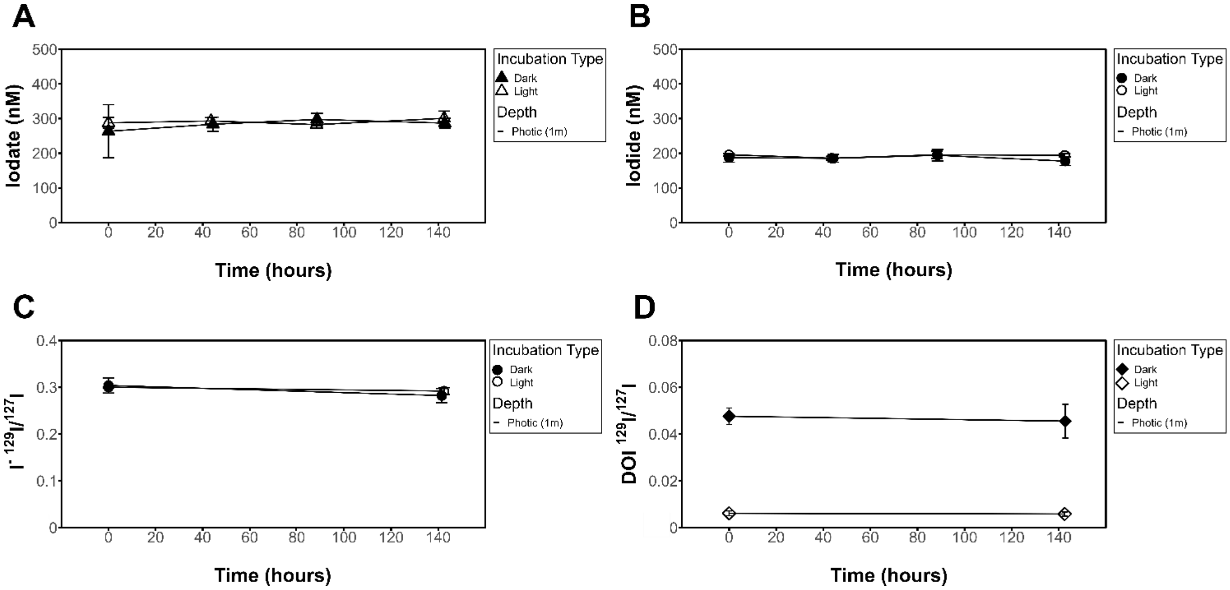

Figure 1.4 Influence of light on filtered seawater for [IO_3^-], [I^-], I^- $^{129}I/^{127}I$ ratios, and DOI $^{129}I/^{127}I$ ratios. No change seen in A) [IO_3^-], B) [I^-], C) $^{129}I/^{127}I$ I^- isotope ratio, or D) $^{129}I/^{127}I$ DOI isotope ratio results in light (incubation 6) vs dark (incubation 8) experiments.

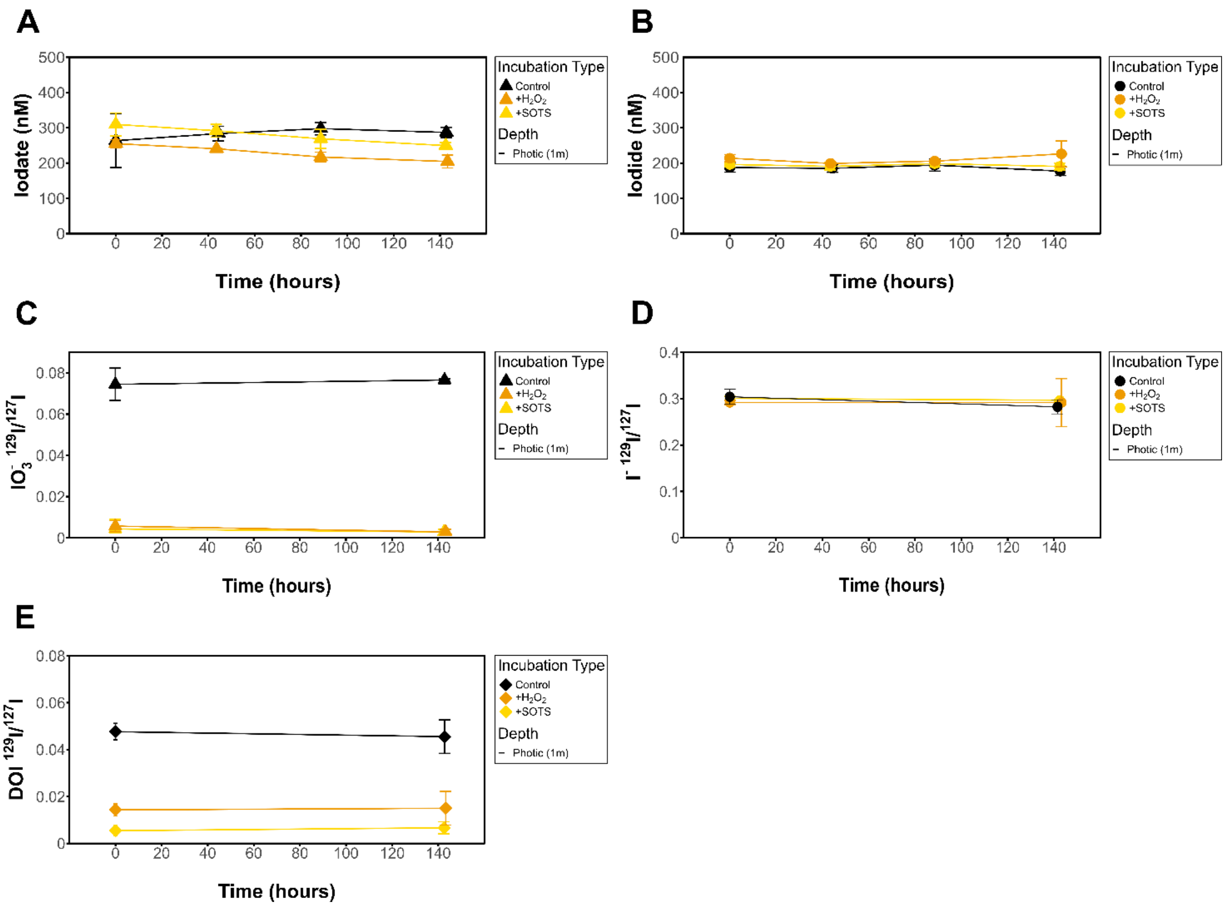

Figure 1.5 Influence of H_2O_2 and SOTS on filtered [IO_3-], [I$^-$], IO_3^- $^{129}I/^{127}I$ ratios, I$^-$ $^{129}I/^{127}I$ ratios, and DOI $^{129}I/^{127}I$ ratios for dark incubations.

1.5: Discussion

We measured the iodine speciation of shipboard incubations performed as part of the Bermuda Atlantic Time Series (BATS) in the Sargasso Sea in September of 2018, as well as depth profiles of [IO_3^-] and [I$^-$] from both BATS and Hydrostation S stations. Depth profiles repeat a typical trend for iodine redox species in surface waters, including increases in I$^-$ at the sea surface and nearly complete IO_3^- below the euphotic zone (Figure 1.2). Incubation treatments described above (Table 1.1) tested the significance of the presence of the ROS $O_2^{\bullet-}$ (added as SOTS) and H_2O_2 on IO_3^- and I$^-$ concentrations in natural seawater settings.

1.5.1: Temporal and methodological iodine comparison

This is the first report of $O_2^{\bullet-}$ at BATS, although iodine speciation at BATS and Hydrostation S has been previously reported through investigations of depth profiles of [I$^-$] and [IO_3^-] over time to a depth of up to 2500 m (Jickells et al., 1988; Campos et al., 1996)

(Figure 1.2A, Figure 1.6). The similarities between measured iodine speciation profiles provide some constraints on the reproducibility of variable iodine speciation techniques used between labs. Our current measured data for depth profiles of IO_3^- and I^- at BATS generally agree with that of Campos et al. (1996) and demonstrate little change in iodine speciation with time. We also extended those investigations here to the bottom waters at 4500 m. While not the focus here, we note that our new bottom water data additionally show elevated I^-, consistent with other studies demonstrating likely benthic I^- fluxes in abyssal plains (Francois, 1987a; Francois, 1987b; Kennedy and Elderfield 1987a; Kennedy and Elderfield 1987b; Moriyasu et al., 2023).

Our data from Hydrostation S also generally overlaps with the range observed in Jickells et al. (1988); however, we note that our I^- data have a range that extends below that of these previous data. One explanation is that Jickells et al. (1988) measured I^- via difference between total iodine – determined via a UV-oxidation technique – and the spectrophotometrically measured IO_3^-, as was done here. Note that the opposite is true for Campos et al. (1996), who reduced IO_3^- to I^- and calculated IO_3^- via difference following voltametric analysis (Total I – I^-). For both cases, given that total iodine includes organic iodine, this implies the potential that DOI is contributing to either the I^- or IO_3^- pool, depending on the technique. While not thoroughly evaluated in this study, we note that DOI concentrations in measured incubations were up to 10% of the total iodine pool, so this could explain the difference between ours and earlier studies.

Alternatively, the difference is Hydrostation S data ranges between the two studies could reflect real changes in hydrography or primary production. For the seasonal study of Jickells et al. (1988), these previous seasonal IO_3^- lows and I^- high values were generally observed in the summer and interpreted to reflect more limited water mass exchange, which allows the combination of local Bermuda inshore inputs and primary productivity to limit IO_3^- availability. In the absence of a seasonal iodine context, it is difficult to explain the differences from our September 2018 data, but it is likely that increased water mass exchange – increasing the supply of high IO_3^- and low I^- from deeper waters and the Sargasso Sea generally – plays an important role. For example, the similarities in our 2018 BATS and Hydrostation S data suggest the potential for increased hydrographic exchange between these two sites. Further, the September 2018 sampling overlapped with the passage of Hurricane Florence 750 miles southeast of Bermuda on September 9th, 2018. While the mixed layer depth from September 2018 is like that of previous years, hurricanes have been documented to influence nutrient and other chemical parameters via increased mixing (Babin et al., 2004).

We note that while seasonal iodine variations may be driven by variations in primary productivity and mixed layer depth, other factors may contribute to longer-term evolution of iodine speciation. Specifically, Hughes et al. (2021) demonstrate that I^- oxidation to IO_3^- may be linked to nitrification, which is sensitive to a range of factors – e.g., light, O_2, temperature, pH, and photochemically produced ROS (Pajares and Ramos, 2019; Morris et al., 2022). Given the baseline iodine speciation conditions documented here and in previous studies, BATS may be an ideal location to track potential future changes in iodine speciation linked to predictions of evolving nitrification from global warming and ocean acidification (Bemen et al., 2012). To our knowledge, the only other locations with multiple iodine measurements are from the Black Sea (Wong and Brewer, 1977; Luther and Campbell, 1991; Truesdale et al., 2001a) and Baltic Sea (Hou et al., 2001; Truesdale et al., 2001b; Aldahan et al., 2007; Truesdale et al., 2013), but iodine speciation changes there will additionally be sensitive to the well-known presence of hypoxia and euxinia.

1.5.2: Limitations of experimental approach

Prior to interpretations, it is important to discuss the limitations of our experimental and analytical approaches. First, while isotope ratio variations (or lack thereof) form the basis of our interpretations, we note that variability in triplicate measurements in isotopes and concentrations measured via ICP-MS and spectrophotometry all contribute to the uncertainty of our rate calculations (Table 1.3). As previously mentioned, we acknowledge that the spectrophotometric method of measuring [IO_3^-] is prone to interferences and relatively low precision (Truesdale, 1978; Luther et al., 1988). For example, variation observed in the IO_3^- concentration but not in

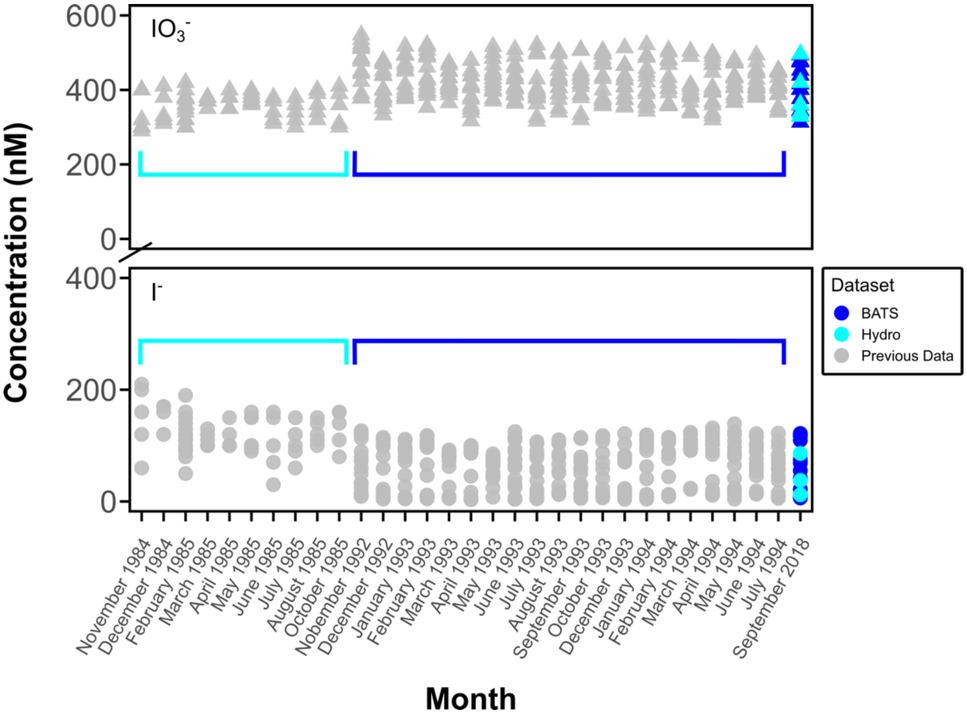

Figure 1.6 Comparison of previous BATS and Hydrostation S monthly concentration data of I$^-$ (●) and IO_3^- (▲). Data from Campos et al., 1996 (BATS) and Jickells et al. 1988 (Hydrostation S) (gray symbols, surface to 200 m (Hydrostation S) and to 600 m (BATS)) and this study (blue and cyan symbols, surface to 600 m).

IO_3^- isotope ratios for the ROS-amended incubations (Figure 1.5) is likely attributed to interferences and not iodine species variations (see Supplementary Information). That said, beyond this example, there was general agreement between IO_3^- concentration and iodine isotope trends in this study and between ours and previously measured IO_3^- concentrations at Hydrostation S and BATS (Figures 1.2 and 1.6).

Another important limitation is the duration of the experiments, which likely induced bottle effects in unfiltered conditions. For example, a subset of our experiments was unfiltered in order to retain particles and native biological communities, but changes in community composition is well known within prolonged bottle experiments, even within 24 hours (or Berg et al., 1999). Our experiments lasted ~140 hours (due to the known sluggish iodine oxidation kinetics) and the biological communities of unfiltered controls were not monitored. As there were no nutrient enrichments in our unfiltered incubations, it is likely that native cells underwent physiological changes that altered the balance between phytoplankton and bacteria. While not observed here, such a turnover could have shifted the balance between iodine oxidation and reduction, or commenced cell senescence, which favors I^- release (e.g., Bluhm et al., 2010). This places a limitation on our ability to interpret biologically induced iodine oxidation and reduction in unfiltered incubations; however, biological turnover is not a factor in our filtered controls testing additional oxidation-reduction pathways.

An additional limitation on our experiments is uncertainty regarding the superoxide concentrations and decay rate in the SOTS amended incubations. Specifically, the superoxide concentration and decay rate were not quantified directly in these incubations. That said, SOTS was added at a concentration estimated to produce an excess superoxide (25-55 nM instantaneous superoxide) relative to the natural waters of BATS (Figure 1.2). The instantaneous superoxide concentration can be estimated from temperature-dependent decay constants – $4.3\text{-}9.9\text{x}10^{-5}$ s^{-1} at 28.2-29.2°C (Heller and Croot, 2010) – and the observed superoxide decay constant from analogous oligotrophic waters (0.01 s^{-1}; (Roe et al., 2016)). While experiments were conducted in a shipdeck chamber continuously refilled with local surface water, the temperature was not directly monitored; however, we note that the biggest uncertainty in kSOTS comes from uncertainty in the values at a given temperature and not from the temperature range. Regardless, the conservative estimate of 25 nM superoxide is still in excess of that measured in water column profiles from this study (Figure 1.2).

1.5.3: Rates of I^- oxidation

Understanding the rates of I^- oxidation to IO_3^- is essential for already applied marine iodine cycling models (Lu et al., 2018; Wadley et al., 2020), but direct constraints are limited. In this study, all incubations showed no discernible change in $[IO_3^-]$, $[I^-]$, or the $^{129}I/^{127}I$ of IO_3^- beyond uncertainties over the timeframe of the incubations (~140 hours) (Figures 1.3–1.5).

While direct observations of IO_3^- production from I^- remains an important goal, our use of a radiotracer still allows us to place novel constraints on the maximum rates of I^- oxidation to IO_3^- based on the limitations of our analytical uncertainties (Table 1.3). Specifically, a lack of change seen over time in these incubations in both concentration and $^{129}I/^{127}I$ ratios are used to constrain a rate of <2.99 nM/day ± 0.53 nM/day. Previously calculated values of I^- oxidation have been reported from BATS from mass balance studies to be between 0.74 and 18 nM/day (Table 1.4). The value calculated for our incubation studies fits well in this range (Table 1.2), supporting previous claims that oxidation of I^- to IO_3^- is slow in natural seawaters (Hardisty et al., 2020; Carpenter et al., 2021).

Further, we observe non-negligible ^{129}I in the initial post-spike sample for both the IO_3^- and DOI incubation pools. Hardisty et al. (2020) made a similar observation and provided some evidence that the iodine-129 spike, while overwhelmingly I^-, contains some oxidized iodine. An alternative explanation is that the IO_3^- or iodine intermediates rapidly form upon addition to seawater or other solutions. This observation implies the potential for near instantaneous formation of $^{129}IO_3^-$ or DOI upon addition of spike to samples. Since the increase in $^{129}I/^{127}I$ was not ongoing, this would require rapid quenching of an existing oxidant in seawater, thus inhibiting further oxidation.

Location	Rate	Method	Source
Bermuda Atlantic Time Series	<0.44-2.99 nM/day	^{129}I doped seawater incubations	This study
Bermuda Atlantic Time Series	0.74 nM/day	Seasonal mass balance	Campos et al., 1996
Bermuda Atlantic Time Series	<4-18 nM/day*	Predicted from measured nitrification rates	Hughes et al., 2021; Newell et al., 2013
Martha's Vineyard Sound	0.32-0.52 nM/day	^{129}I doped seawater incubations	Hardisty et al., 2020
Pacific Gyre	1.53 nM/day	Seasonal mass balance	Campos et al., 1996
Eastern Tropical Pacific	$5.3\pm0.5\times10^{-4}$ nM/day	1-Dimensional iodide oxidation model	Moriyasu et al., 2023

**Calculated based on BATS nitrification rates (Newell et al., 2013) and IO_3^- production rate 2-9 times that of nitrification (Hughes et al., 2021)*

Table 1.4 Previously reported daily I^- oxidation rates.

1.5.4: Role of reactive oxygen species in I- oxidation to IO_3^- in natural seawater

We provide here the most detailed and direct constraints to date of the potential for the ROS $O_2^{\bullet-}$ (added as the chemical source SOTS) and H_2O_2 to oxidize I^- to IO_3^- in natural seawater. To the point, in our incubations with added $O_2^{\bullet-}$ and H_2O_2, no oxidation of I^- to IO_3^- was observed in BATS seawater, as shown in $^{129}I/^{127}I$ ratios of IO_3^- (Figure 1.5). We emphasize that this does not completely rule out the role of ROS in I^- oxidation broadly. Below we consider the implications of these results in coordination with previous studies evaluating the role, if any, of ROS on iodine cycling.

First, it is possible that ROS is preferentially reacting with dissolved organic matter or another component of seawater (e.g., Mn, NOx) (Wuttig et al., 2013; Li et al., 2014; Sutherland et al., 2021). We did not constrain alternative electron acceptors here but given the oligotrophic nature of BATS and known low dissolved Mn (Wu et al., 2014), this would imply that preferential extracellular $O_2^{\bullet-}$ scavenging relative to I^- is common throughout most of the ocean, and intracellular ROS have been shown to be a significant oxygen sink (Sutherland et al., 2021), hence diminishing the likely role of $O_2^{\bullet-}$ in marine I^- oxidation more broadly. Some evidence for preferential reaction of ROS with other redox-active species may come from the interference observed for our spectrophotometric measurements of IO_3^-. Second, thermodynamic calculations predict that $O_2^{\bullet-}$ alone forms iodine intermediates and cannot fully oxidize I^- to IO_3^-, so it is likely that iodine intermediates such as I_2, HOI, or DOI, instead of IO_3^-, in samples with excess H_2O_2 or SOTS added, are forming. This implies a potential role of ROS in iodine redox species cycling but contrasts previous findings. As discussed in detail in Luther (2023), reactions with $O_2^{\bullet-}$ and I^- forms I_2 and subsequently I_2^- (Bielski et al., 1985; Schwarz and Bielski, 1986). I_2 reacts quickly with organic matter to form DOI, which may act as a bottleneck in some environments to titrate I_2 and prevent subsequent oxidation (e.g., Hardisty et al., 2020). Since the $^{129}I/^{127}I$ ratio of DOI did not change in experiments (Figure 1.5E), it implies relatively little, if any, oxidation to intermediates forming DOI. Beyond this, $O_2^{\bullet-}$ is not favorable to subsequently oxidize I_2/I_2^- to form IO_3^-. Instead, •OH or O_3 are required for subsequent HOI formation, and OH, O_3, and H_2O_2 can then oxidize to IO_2^-, and then subsequently to IO_3^-. O_3 is not prevalent beyond the marine micro-layer and thus is unlikely responsible for I^- oxidation elsewhere in seawater.

Ultimately, these thermodynamic considerations imply that combinations of $O_2^{\bullet-}$ and H_2O_2, and perhaps OH radicals produced during their reduction, are necessary for complete oxidation from I^- to IO_3^- via ROS. Therefore, ROS most likely play a minor, if any, role in IO_3^- formation given the combination of: slow predicted kinetics (e.g., Wong and Zhang, 2008), limited ROS in seawater relative to iodine, the up to four step oxidation sequence each consuming ROS ($I^- \rightarrow I_2 \rightarrow HOI \rightarrow IO_2^- \rightarrow IO_3^-$), abundance of DOM and other preferred electron acceptors/donor – such as Br and Mn – for ROS, titration of HOI with DOM, and the likelihood of back reactions of iodine intermediates to I^-.

1.5.5: Constraints on other redox pathways

The lack of change in [IO_3^-], [I^-] or $^{129}I/^{127}I$ isotope ratios over the incubation period (~140 hours) (Figure 1.4) for the incubations exposed to dark vs light conditions additionally provide constraints on the likelihood of iodine redox reaction pathways. First, interactions between light and organic matter represent an abiotic pathway for ROS production (Morris et al., 2022). If $^{129}IO_3^-$ formation had been observed in the light experiments, an abiotic ROS mechanism could have been inferred from a lack of $^{129}IO_3^-$ in both the dark and light +SOD controls. Second, natural light is also suggested to aid in photo-reduction of IO_3^- in seawater, although it is not known how important this reduction pathway may be for I^- accumulation in the surface ocean (Spokes and Liss, 1996; Chance et al., 2014). Conversion of IO_3^- to I^- observed in both isotopes and concentrations would provide evidence for such a pathway, but this was not observed in this study.

1.5.6: Implications for marine iodine redox cycling and distributions

Our results support mounting evidence that iodine cycling in some ocean regions, if not more broadly, may be considered semi-conservative. From this perspective, given the relatively oligotrophic conditions at BATS (Lipschultz et al., 2002), it is perhaps not surprising that IO_3^- production may be slow or isolated to specific depths or even seasons. For example, laboratory cultures have identified nitrification as a possible pathway of IO_3^- production, which occurs specifically at the nitrite maximum at BATS and other similar localities (Newell et al., 2013; Hughes et al., 2021). In addition, Luther (2023) provides thermodynamic constraints that OH is a powerful oxidant capable of producing IO_3^-. Oxygenated waters supporting dissolved Fe – such as hydrothermal plumes, some low oxygen zones, and the benthic boundary layer – produce elevated •OH via Fenton chemistry, which could oxidize I^- to IO_3^- (e.g., Shaw et al., 2021). Luther (2023) also suggests that O_3 and N_2O can form IO_3^-, indicating that marine microlayer (Carpenter et al., 2021) and the oxycline of oxygen deficient zones (Babbin et al., 2015) may be important for IO_3^- production, respectively. Lastly, IO_3^- reduction in surface waters is more clearly linked to phytoplankton, which show seasonal distributions at BATS (Michaels et al., 1994; Michaels and Knap, 1996; DuRand et al., 2001).

Ex situ mixing of source waters from "hotspots" of high primary productivity, oxygen deficient zones, and pore waters may initiate iodine speciation gradients in surface waters whose rates of change slow as water masses extend to the open ocean from coastal or productive settings. As a result, water mass mixing may have a more dramatic effect on the distribution of iodine species in the open surface ocean than previously known. For example, Chance et al. (2020) and Chance et al. (2010) provided some evidence that diffusion/advection of IO_3^- from below the mixed layer may be important for controlling surface ocean IO_3^- abundance. Even in oxygen deficient zones, Hardisty et al. (2021) provide evidence that below the oxycline that IO_3^- has the potential to reflect water mass mixing, as opposed to clear *in situ* IO_3^- reduction.

1.6: Conclusions

We performed shipboard incubation experiments of seawater at the Bermuda Atlantic Time Series in the Sargasso Sea. These included natural concentrations of iodine and the reactive oxygen species $O_2^{\bullet-}$ and H_2O_2 to better understand the mechanisms of oxidation of I^- to IO_3^- in surface seawaters and better constrain the rates at which oxidation of I^- to IO_3^- takes place in the open ocean. We provided evidence that rates of I^- oxidation are extremely slow, if anything, on a daily timescale. We explicitly tested the potential for iodine redox reaction with ROS, which did not oxidize I^- within the resolution of our analytical uncertainty.

Based on the sluggish iodine oxidation rates, it is likely that *ex situ* sources of transportation, such as water mass mixing and vertical diffusion, are more important in the distribution of iodine redox species from “hotspots” of formation, such as areas of very high biogeochemical activity, ODZ’s, and pore waters (Hardisty et al., 2021). This study and similar continuing work will help to inform atmospheric models of O_3 destruction and paleoredox models of IO_3^- incorporation with carbonates for measurement of I/Ca values.

REFERENCES

Aldahan, A., Possnert, G., Alfimov, V., Cato, I., and Kekli, A. (2007). Anthropogenic 129I in the Baltic Sea. Nucl. Instruments Methods Phys. Research Section B: Beam Interact. Materials Atoms 259 (1), 491–495. doi: 10.1016/j.nimb.2007.01.242

Babbin, A. R., Bianchi, D., Jayakumar, A., and Ward, B. B. (2015). Rapid nitrous oxide cycling in the suboxic ocean. Science 348 (6239), 1127–1129. doi: 10.1126/SCIENCE.AAA8380/SUPPL_FILE/BABBIN-SM.PDF

Babin, S. M., Carton, J. A., Dickey, T. D., and Wiggert, J. D. (2004). Satellite evidence of hurricane-induced phytoplankton blooms in an oceanic desert. J. Geophys. Res.- Oceans 109, Artn c03043. doi: 10.1029/2003JC001938

Beman, M. J., Popp, B. N., and Alford, S. E. (2012). Quantification of ammonia oxidation rates and ammonia-oxidizing archaea and bacteria at high resolution in the Gulf of California and eastern tropical North Pacific Ocean. Limnology Oceanography 57 (3), 711–726. doi: 10.4319/lo.2012.57.3.0711

Berg, G. M., Glibert, P. M., and Chen, C. C. (1999). Dimension effects of enclosures on ecological processes in pelagic systems. Limnol. Oceanogr. 44, 1331–1340. doi: 10.4319/lo.1999.44.5.1331

Bielski, B. H. J., Cabelli, D. E., Arudi, R. L., and Ross, A. B. (1985). Reactivity of HO2/ O–2 radicals in aqueous solution. J. Phys. Chem. Reference Data 14 (4), 1041. doi: 10.1063/1.555739

Bluhm, K., Croot, P., Wuttig, K., and Lochte, K. (2010). Transformation of iodate to iodide in marine phytoplankton driven by cell senescence. Aquat. Biol. 11, 1–15. doi: 10.3354/ab00284

Bond, R. J., Hansel, C. M., and Voelker, B. M. (2020). Heterotrophic bacteria exhibit a wide range of rates of extracellular production and decay of hydrogen peroxide. Front. Mar. Sci. 7. doi: 10.3389/FMARS.2020.00072/BIBTEX

Campos, M. L. A. M. (1997). New approach to evaluating dissolved iodine speciation in natural waters using cathodic stripping voltammetry and a storage study for preserving iodine species. Mar. Chem. 57, 107–117. doi: 10.1016/S0304-4203(96) 00093-X

Campos, M. L. A. M**.**, Farrenkopf, A. M., Jickells, T. D., and Luther, G. W. (1996). A comparison of dissolved iodine cycling at the Bermuda Atlantic Time-series Station and Hawaii Ocean Time-series Station. Deep Sea Res. Part II: Topical Stud. Oceanography. 43, 455–466. doi: 10.1016/0967-0645(95)00100-x

Carpenter, L. J., Chance, R. J., Sherwen, T., Adams, T. J., Ball, S. M., Evans, M. J., et al. (2021). Marine iodine emissions in a changing world. Proc. R. Soc. A 477 (2247), 20200824. doi: 10.1098/RSPA.2020.0824

Carpenter, L. J., MacDonald, S. M., Shaw, M. D., Kumar, R., Saunders, R. W., Parthipan, R., et al. (2013). Atmospheric iodine levels influenced by sea surface emissions of inorganic iodine. Nat. Geosci. 6, 108–111. doi: 10.1038/ngeo1687

Chance, R., Baker, A. R., Carpenter, L., and Jickells, T. D. (2014). "The distribution of iodide at the sea surface," in Environmental Sciences: Processes and Impacts. (Piccadilly, London: Royal Society of Chemistry) 118, 171–181. doi: 10.1039/c4em00139g

Chance, R., Tinel, L., Sarkar, A., Sinha, A. K., Mahajan, A. S., Chacko, R., et al. (2020). Surface inorganic iodine speciation in the Indian and southern oceans from 12°N to 70°S. Front. Mar. Sci. 7. doi: 10.3389/FMARS.2020.00621/BIBTEX

Chance, R., Weston, K., Baker, A. R., Hughes, C., Malin, G., Carpenter, L., et al. (2010). Seasonal and interannual variation of dissolved iodine speciation at a coastal Antarctic site. Mar. Chem. doi: 10.1016/j.marchem.2009.11.009

Diaz, J. M., Hansel, C. M., Voelker, B. M., Mendes, C. M., Andeer, P. F., and Zhang, T. (2013). Widespread production of extracellular superoxide by heterotrophic bacteria. Science 340 (6137), 1223–1226. doi: 10.1126/science.1237331

DuRand, M. D., Olson, R. J., and Chisholm, S. W. (2001). Phytoplankton population dynamics at the Bermuda Atlantic Time-series station in the Sargasso Sea. Deep Sea Res. Part II: Topical Stud. Oceanography 48 (8–9), 1983–2003. doi: 10.1016/S0967-0645(00)00166-1

Edwards, A., and Truesdale, V. W. (1997). Regeneration of inorganic iodine species in Loch Etive, a natural leaky incubator. Estuarine Coast. Shelf Sci. 45 (3), 357–366. doi: 10.1006/ECSS.1996.0185

Elderfield, H., and Truesdale, V. W. (1980). On the biophilic nature of iodine in seawater. Earth Planetary Sci. Lett. 50, 105–114. doi: 10.1016/0012-821X(80)90122-3

Farrenkopf, A. M., Dollhopf, M. E., Chadhain, S. N., Luther, G. W., and Nealson, K. H. (1997). Reduction of iodate in seawater during Arabian Sea shipboard incubations and in laboratory cultures of the marine bacterium Shewanella putrefaciens strain MR-4. Mar. Chem. 57, 347–354. doi: 10.1016/S0304-4203(97)00039-X

Francois, R. (1987a). The influence of humic substances on the geochemistry of iodine in nearshore and hemipelagic marine-sediments. Geochimica Et Cosmochimica Acta 51, 2417–2427. doi: 10.1016/0016-7037(87)90294-8

Francois, R. (1987b). Iodine in marine sedimentary humic substances. Sci. Total Environ. 62, 341–342. doi: 10.1016/0048-9697(87)90519-5

Hansard, S. P., Vermilyea, A. W., and Voelker, B. M. (2010). Measurements of superoxide radical concentration and decay kinetics in the Gulf of Alaska. Deep-Sea Res. I 57, 1111–1119. doi: 10.1016/j.dsr.2010.05.007

Hansel, C. M., and Diaz, J. M. (2021). Production of extracellular reactive oxygen species by marine biota. Annu. Rev. Mar. Sci. 2021 (13), 177–200. doi: 10.1146/ annurev-marine-041320

Hansel, C. M., Diaz, J. M., and Plummer, S. (2019). Tight regulation of extracellular superoxide points to its vital role in the physiology of the globally relevant roseobacter clade. MBio 10 (2), e02668-18. doi: 10.1128/MBIO.02668-18/SUPPL_FILE/ MBIO.02668-18-ST003.PDF

Hardisty, D. S., Horner, T. J., Evans, N., Moriyasu, R., Babbin, A. R., Wankel, S. D., et al. (2021). Limited iodate reduction in shipboard seawater incubations from the Eastern Tropical North Pacific oxygen deficient zone. Earth Planetary Sci. Lett. 554, 116676. doi: 10.1016/j.epsl.2020.116676

Hardisty, D. S., Horner, T. J., Wankel, S. D., Blusztajn, J., and Nielsen, S. G. (2020). Experimental observations of marine iodide oxidation using a novel sparge- interface MC-ICP-MS technique. Chem. Geology. 532, 119360. doi: 10.1016/ j.chemgeo.2019.119360

He, P., Hou, X., Aldahan, A., Possnert, G., and Yi, P. (2013). Iodine isotopes species fingerprinting environmental conditions in surface water along the northeastern Atlantic Ocean. Sci. Rep. 3 (1), 1–8. doi: 10.1038/srep02685

Heller, M. I**.**, and Croot, P. L. (2010). Application of a superoxide (O 2 –) thermal source (SOTS-1) for the determination and calibration of O 2 – fluxes in seawater. Analytica Chimica Acta 667, 1–13. doi: 10.1016/j.aca.2010.03.054

Hepach, H., Hughes, C., Hogg, K., Collings, S., and Chance, R. (2020). Senescence as the main driver of iodide release from a diverse range of marine phytoplankton. Biogeosciences. 17, 2453–2471. doi: 10.5194/bg-17-2453-2020

Hou, X., Aldahan, A., Nielsen, S. P., and Possnert, G. (2009). Time series of 129I and 127I speciation in precipitation from Denmark. Environ. Sci. Technol. 43 (17), 6522– 6528. doi: 10.1021/ES9012678

Hou, X., Aldahan, A., Nielsen, S. P., Possnert, G., Nies, H., and Hedfors, J. (2007). Speciation of 129I and 127I in seawater and implications for sources and transport pathways in the North Sea. *Environ. Sci. Technol.* 41, 5993-5999. Doi: 10.1021/ es07057X

Hou, X., Dahlgaard, H., and Nielsen, S. P. (2001). Chemical speciation analysis of 129I in seawater and a preliminary investigation to use it as a tracer for geochemical cycle study of stable iodine. Mar. Chem. 74, 145–155. doi: 10.1016/S0304-4203(01) 00010-X

Hou, X., Dahlgaard, H., Rietz, B., Jacobsen, U., Nielsen, S. P., and Aarkrog, A. (1999). Determination of chemical species of iodine in seawater by radiochemical neutron activation analysis combined with ion-exchange preseparation. Analytical Chem. 71 (14), 2745–2750. doi: 10.1021/AC9813639

Hughes, C., Barton, E., Hepach, H., Chance, R., Pickering, M. D., Hogg, K., et al. (2021). Oxidation of iodide to iodate by cultures of marine ammonia-oxidising bacteria. Mar. Chem. 234, 104000. doi: 10.1016/J.MARCHEM.2021.104000

Ingold, K. U., Paul, T., Young, M. J., and Doiron, L. (1997). Invention of the first azo compound to serve as a superoxide thermal source under physiological conditions: Concept, synthesis, and chemical properties. J. Of Am. Chem. Soc. 119, 12364–12365. doi: 10.1021/ja972886l

Jickells, T. D., Boyd, S. S., and Knap, A. H. (1988). Iodine cycling in the Sargasso Sea and the Bermuda inshore waters. Mar. Chem. 24, 61–82. doi: 10.1016/0304-4203(88) 90006-0

Jones, M. R., Chance, R., Dadic, R., Hannula, H. R., May, R., Ward, M., et al. (2023). Environmental iodine speciation quantification in seawater and snow using ion exchange chromatography and UV spectrophotometric detection. Anal. Chim. Acta, 1239. doi: 10.1016/j.aca.2022.340700

Kennedy, H. A., and Elderfield, H. (1987a). Iodine diagenesis in non-pelagic deep-sea sediments. Geochimica et Cosmochimica Acta 51, 2505–2514. doi: 10.1016/0016-7037 (87)90301-2

Kennedy, H. A., and Elderfield, H. (1987b). Iodine diagenesis in pelagic deep-sea sediments. Geochimica Et Cosmochimica Acta 51, 2489–2504. doi: 10.1016/0016-7037 (87)90300-0

Konya, K. G., Paul, T., Lin, S., Lusztyk, J., and Ingold, K. U. (2000). Laser flash photolysis studies on the first superoxide thermal source. First direct measurements of the rates of solvent-assisted 1,2- hydrogen atom shifts and a proposed new mechanism for this unusual rearrangement1. J. Am. Chem. Soc. 122, 7518–7527. doi: 10.1021/ ja993570b

Li, H. P., Daniel, B., Creeley, D., Grandbois, R., Zhang, S., Xu, C., et al. (2014). Superoxide production by a manganese-oxidizing bacterium facilitates iodide oxidation. Appl. Environ. Microbiol. 80, 2693–2699. doi: 10.1128/AEM.00400-14

Li, H. P., Yeager, C. M., Brinkmeyer, R., Zhang, S., Ho, Y. F., Xu, C., et al. (2012). Bacterial production of organic acids enhances H2O 2-dependent iodide oxidation. Environ. Sci. Technol. 46, 4837–4844. doi: 10.1021/es203683v

Lipschultz, F., Bates, N. R., Carlson, C. A., and Hansell, D. A. (2002). New production in the Sargasso Sea: History and current status. Global Biogeochemical Cycles 16 (1), 1–1. doi: 10.1029/2000GB001319

Lu, W., Ridgwell, A., Thomas, E., Hardisty, D. S., Luo, G., Algeo, T. J., et al. (2018). Late inception of a resiliently oxygenated upper ocean. Science. 361, 174–177. doi: 10.1126/science.aar5372

Luhar, A. K., Galbally, I. E., Woodhouse, M. T., and Thatcher, M. (2017). An improved parameterisation of ozone dry deposition to the ocean and its impact in a global climate-chemistry model. Atmospheric Chem. Phys. 17, 3749–3767. doi: 10.5194/ acp-17-3749-2017

Luther, G. W. I. (2023). Review on the physical chemistry of iodine transformations in the oceans. Front. Mar. Sci. 10, 1721–1724. doi: 10.3389/FMARS.2023.1085618

Luther, G. W., and Campbell, T. (1991). Iodine speciation in the water column of the Black Sea. Deep Sea Research Part A. Oceanographic Res. Papers. 38, S875–S882. doi: 10.1016/s0198-0149(10)80014-7

Luther, G. W., Swartz, C. B., and Ullman, W. J. (1988). Direct determination of iodide in seawater by Cathodic stripping square wave voltammetry. Analytical Chem. 60 (17). doi: 10.1021/ac00168a017

Luther, G. W., Wu, J., and Cullen, J. B. (1995). Redox Chemistry of Iodine in Seawater. (Washington, D.C.: American Chemical Society), 135–155. doi: 10.1021/BA-1995-0244.CH006

Michaels, A. F., and Knap, A. H. (1996). Overview of the U.S. JGOFS Bermuda Atlantic Time-series study and the hydrostation S program. Deep-Sea Res. Part II: Topical Stud. Oceanography 43 (2–3), 157–198. doi: 10.1016/0967-0645(96)00004-5

Michaels, A. F., Knap, A. H., Dow, R. L., Gundersen, K., Johnson, R. J., Sorensen, J., et al. (1994). Seasonal patterns of ocean biogeochemistry at the U.S. JGOFS Bermuda Atlantic time-series study site. Deep-Sea Res. Part I. 41, 1013–1038. doi: 10.1016/0967- 0637(94)90016-7

Moriyasu, R., Evans, N., Bolster, K. M., Hardisty, D. S., and Moffett, J. W. (2020). The Distribution and Redox Speciation of Iodine in the Eastern Tropical North Pacific Ocean. Global Biogeochem Cycles 34 (2). doi: 10.1029/2019GB006302

Moriyasu, R., Bolster, K. M., Hardisty, D. S., Kadko, D. C., Stephens, M. P., and Moffett, J. W. (2023). Meridional survey of the central pacific reveals iodide accumulation in equatorial surface waters and benthic sources in the abyssal plain. Global Biogeochem. Cycles 37 (3), e2021GB007300. doi: 10.1029/2021GB007300

Morris, J. J., Rose, A. L., and Lu, Z. (2022). Reactive oxygen species in the world ocean and their impacts on marine ecosystems. Redox Biol. 52, 102285. doi: 10.1016/ j.redox.2022.102285

Newell, S. E., Fawcett, S. E., and Ward, B. B. (2013). Depth distribution of ammonia oxidation rates and ammonia-oxidizer community composition in the Sargasso Sea. Limnology Oceanography 58 (4), 1491–1500. doi: 10.4319/LO.2013.58.4.1491

Pajares, S., and Ramos, R. (2019). Processes and microorganisms involved in the marine nitrogen cycle: knowledge and gaps. Front. Mar. Sci. 6. doi: 10.3389/ fmars.2019.00739

Reifenhäuser, C., and Heumann, K. G. (1990). Development of a definitive method for iodine speciation in aquatic systems. Fresenius J. Anal. Chem. 336 (7), 559–563. doi: 10.1007/BF00331416/METRICS

Roe, K. L., Schneider, R. J., Hansel, C. M., and Voelker, B. M. (2016). Measurement of dark, particle-generated superoxide and hydrogen peroxide production and decay in the subtropical and temperate North Pacific Ocean. Deep-Sea Res. I 107, 59–69. doi: 10.1016/j.dsr.2015.10.012

Rose, A. L., Webb, E. A., Waite, T. D., and Moffett, J. W. (2008). Measurement and implications of nonphotochemically generated superoxide in the equatorial pacific ocean. Environ. Sci. Technol. 42 (7), 2387–2393. doi: 10.1021/ES7024609/SUPPL_FILE/ ES7024609-FILE003.PDF

Rusak, S. A., Peake, B. M., Richard, E., Nodder, S. D., and Cooper, W. J. (2011). Distributions of hydrogen peroxide and superoxide in seawater east of New Zealand. Mar. Chem. 127, 155–169. doi: 10.1016/j.marchem.2011.08.005

Schwarz, H. A., and Bielski, B. H. J. (1986). Reactions of HO2 and O2- with iodine and bromine and the I2- and I atom reduction potentials. J. Phys. Chem. 90 (7), 1445– 1448. doi: 10.1021/J100398A045/ASSET/J100398A045.FP.PNG_V03

Shaw, T. J., Luther, G. W., Rosas, R., Oldham, V. E., Coffey, N. R., Ferry, J. L., et al. (2021). Fe-catalyzed sulfide oxidation in hydrothermal plumes is a source of reactive oxygen species to the ocean. Proc. Natl. Acad. Sci. United States America 118 (40), e2026654118. doi: 10.1073/PNAS.2026654118/SUPPL_FILE/PNAS.2026654118.SAPP.PDF

Spokes, L. J., and Liss, P. S. (1996). Photochemically induced redox reactions in seawater, II. Nitrogen and iodine. Mar. Chem. 54, 1–10. doi: 10.1016/0304-4203(96) 00033-3

Sutherland, K. M., Grabb, K. C., Karolewski, J. S., Plummer, S., Farfan, G. A., Wankel, S. D., et al. (2020). Spatial heterogeneity in particle-associated, light-independent superoxide production within productive coastal waters. J. Geophys. Res. Oceans 125, e2020JC016747. doi: 10.1029/2020JC016747

Sutherland, K. M., Grabb, K. C., Karolewski, J. S., Taenzer, L., Hansel, C. M., and Wankel, S. D. (2021). The redox fate of hydrogen peroxide in the marine water column. Limnology Oceanography 66 (10), 3828–3841. doi: 10.1002/LNO.11922

Sutherland, K. M., Wankel, S. D., and Hansel, C. M. (2020). Dark biological superoxide production as a significant flux and sink of marine dissolved oxygen. Proc. Natl. Acad. Sci. United States America. doi: 10.1073/pnas.1912313117

Truesdale, V. W. (1978). The automatic determination of iodate- and total-iodine in seawater. Mar. Chem. 6 (3), 253–273. doi: 10.1016/0304-4203(78)90034-8

Truesdale, V. W., Nausch, G., and Baker, A. (2001a). The distribution of iodine in the Baltic Sea during summer. Mar. Chem. 74, 87–98. doi: 10.1016/S0304-4203(00)00115-8

Truesdale, V. W., Nausch, G., and Waite, T. J. (2013). The effects of the 2001 Barotropic intrusion of bottom-water upon the vertical distribution of inorganic iodine in the Gotland Deep. Continental Shelf Res. 55, 155–167. doi: 10.1016/j.csr.2013.01.005

Truesdale, V. W., Watts, S. F., and Rendell, A. R. (2001b). On the possibility of iodide oxidation in the near-surface of the Black Sea and its implications to iodine in the general ocean. Deep Sea Res. Part I: Oceanographic Res. Papers 48 (11), 2397–2412. doi: 10.1016/S0967-0637(01)00021-8

Wadley, M. R., Stevens, D. P., Jickells, T. D., Hughes, C., Chance, R., Hepach, H., et al. (2020). A global model for iodine speciation in the upper ocean. Global Biogeochemical Cycles 34 (9), e2019GB006467. doi: 10.1029/2019GB006467

Wong, G. T. F., and Brewer, P. G. (1977). The marine chemistry of iodine in anoxic basins. Geochimica Cosmochimica Acta. 41, 151–159. doi: 10.1016/0016-7037(77)90195-8

Wong, G. T. F., and Cheng, X. H. (1998). Dissolved organic iodine in marine waters: Determination, occurrence and analytical implications. Mar. Chem. 59, 271–281. doi: 10.1016/S0304-4203(97)00078-9

Wong, G. T. F., and Zhang, L. S. (2008). The kinetics of the reactions between iodide and hydrogen peroxide in seawater. Mar. Chem. 111, 22–29. doi: 10.1016/ j.marchem.2007.04.007

Wu, J., Roshan, S., and Chen, G. (2014). The distribution of dissolved manganese in the tropical–subtropical North Atlantic during US GEOTRACES 2010 and 2011 cruises. Mar. Chem. 166, 9–24. doi: 10.1016/J.MARCHEM.2014.08.007

Wuttig, K., Heller, M. I., Croot, P. L., and Biogeochemistry, M. (2013). Pathways of Superoxide (O 2 –) Decay in the Eastern Tropical North Atlantic. (Washington, D. C.: American Chemical Society). doi: 10.1021/es401658t

Žic, V., and Branica, M. (2006). The distributions of iodate and iodide in Rogoznica Lake (East Adriatic Coast). Estuarine Coast. Shelf Sci. 66 (1–2), 55–66. doi: 10.1016/

APPENDIX

S.1 Assessing effects of H_2O_2 on potassium iodate (KIO_3^-) in artificial seawater

An artifact of incubations doped with ROS (SOTS, H_2O_2) was noticed to shift the 320 nm absorbance value of IO_3^- samples from BATS +ROS incubations to greater values. Specifically, there was a shift in the known I_3^- absorbance curve trough at 320 nm to a higher absorbance value and longer wavelength over time ($t_0 \rightarrow t_f$), whereas control samples (photic, dark, filtered, with no addition of ROS (incubations 8)) showed no such shift (Supplementary Figure 1.1A). This feature was seen exclusively in incubations with added SOTS and H_2O_2 at both photic and subphotic depths. Importantly, +SOTS (incubations 11 and 19) and +H_2O_2 (incubations 12 and 20) measured again, nearly five years after collection and 3.5 years after initial spectrophotometric measurement, preserved the same trough shift as measured previously. It is possible that this shift in the curve location could artificially increase nMIO_3^- values for these samples (Supplementary Figure 1.1B and 1.1C) and "flatten the curve" which then indicates that ROS incubations decreased in [IO_3^-] over time. To confirm this interference was a result of SOTS and H_2O_2 addition specifically, we performed laboratory experimental incubations using concentration of H_2O_2 ([50 nM]) in both 18.2 MΩ-cm water and artificial seawater (Instant Ocean Reef Crystals) with 500 nM KIO_3^- added. These experimental incubations, along with respective controls without H_2O_2 addition, were performed over a six-day time period similar to that used for original BATS incubations, with four time points collected over six days (t_0-t_4) and frozen (-20°C) until analyzed with the same spectrophotometric method described for BATS incubation samples, described in section 1.3.3.2. Both 18.2 MΩ-cm water and artificial seawater samples with and without added H_2O_2 in this experiment showed no change in trough location, similar to that of incubation 8 "control" samples measured previously. Therefore, it is likely that interactions within natural seawater with added ROS are causing the change seen in BATS incubations. We also note small "notches" that appear around 370 nm in all measurements. While uncertain of the source, our calculations utilize values from 320 nm, 350 nm, and 400 nm exclusively for IO_3^- concentration calculations, and therefore this distinctive pattern is unlikely impacting our results.

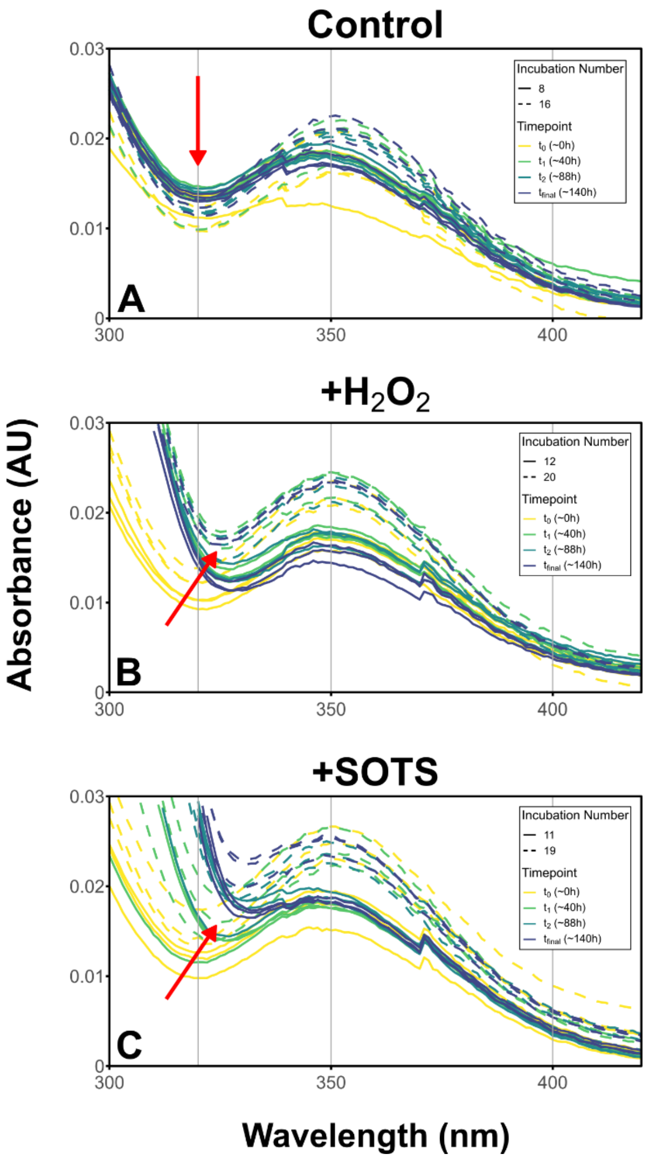

Supplementary Figure 1.1 Spectrophotometer absorbance curves for A) incubation 8 (control), B) incubations 11 and 19 (+SOTS), and C) incubations 12 and 20 (H_2O_2) from t_0 to t_f. Note the shift in trough location (red arrow) for +SOTS and $+H_2O_2$ incubations at both 1 m (photic) and 240 m (subphotic) depths. This shift was not observed in 18.2 MΩ-cm water and artificial seawater laboratory incubations with increased [ROS].

*Chapter 1 of this dissertation was previously published in *Frontiers in Marine Science* under a Creative Commons Attribution License:

Schnur AA, Sutherland KM, Hansel CM and Hardisty DS (2024) Rates and pathways of iodine speciation transformations at the Bermuda Atlantic Time Series. Front. Mar. Sci. 10:1272870. doi: 10.3389/fmars.2023.1272870

CHAPTER 2: MASS BALANCE CONSTRAINTS ON EUPHOTIC IODINE SPECIATION FROM GEOTRACES PACIFIC MERIDIONAL TRANSECTS

2.1: Abstract

Understanding the distribution of euphotic iodine in the ocean is necessary because of its importance in models of the oxygen cycle – including as a primary tropospheric ozone (O_3) sink and tracer of modern and ancient oxygen deficient zones (ODZs). The distribution of iodine species – the oxidized and reduced iodate (IO_3^-) and iodide (I^-), respectively – in oxic, euphotic ocean settings generally displays an increase in I^- and corresponding decrease in IO_3^- at low latitudes and approaching shorelines. Sub-photic waters are nearly completely IO_3^-. These trends are well known, however, their driving mechanisms are not well resolved, thus impeding quantitative understanding of iodine cycling in these areas. For example, I^- is produced *in situ* at the sea surface through phytoplankton reduction of IO_3^-, but I^- re-oxidation is not well understood and seemingly relatively slow, which implies that *ex situ* conservative mixing processes may be an under-appreciated euphotic IO_3^- source. To quantitatively constrain euphotic iodine speciation trends in the Pacific Ocean basin, we measured iodine redox species concentrations in combinations of surface and depth profiles from the GEOTRACES GP15 (September 2018) and GEOTRACES GP17-OCE (December 2022) cruise transects from Alaska to Tahiti and Tahiti to Chile (56°N to 67°S), respectively, to complete the a high-resolution surface meridional transect of iodine with latitude and depth in the Pacific Ocean. Iodine species vary in euphotic waters related to distinct biological zones, surface water masses, and climatological fronts. Together with complimentary tracers (e.g., ^{7}Be, Net Community Production (NCP)), we performed mass balance calculations quantifying the contributions of iodine species from *ex situ* sources such as upwelling and vertical diffusion in the Pacific via estimates of iodine incorporation into primary producers (I:C ratio) and measured IO_3^- concentrations through the water column. Our estimated phytoplankton I:C ratio of $1.2\text{x}10^{-2}$ in the South Pacific is found to be higher than previously reported values between 10^{-3} and 10^{-5}, while a calculated euphotic IO_3^- production flux of 0.23 mmol m^{-2} d^{-1} fits well with previously reported values in the Pacific Gyre. Together, these data demonstrate iodine variations related to non-redox specific physical and biogeochemical processes that offer important insights into the controls on IO_3^- distribution on a basinal scale in modern and ancient marine settings.

2.2: Introduction

Understanding the distribution of iodine in the surface ocean is important for the interpretation of iodine's role in other widespread phenomena, such as those associated with the cycling of oxygen and paleoredox processes. For example, because the oxygenated iodine species IO_3^- is incorporated into the lattice of carbonate minerals, carbonate-bound iodine has been widely applied as a tracer of ancient marine oxygen (Lu et al., 2010, Hardisty et al., 2014). Iodide at the sea surface is also a major sink for O_3, as I^- reduces O_3 to O_2 and forms iodine oxide (IO), which is then released back to the atmosphere (Carpenter et al., 2013, Luhar et al., 2017).

Understanding the drivers of latitudinal trends of iodine redox species' distribution at the sea surface is important for models of tropospheric O_3 and dissolved oxygen (Cheng et al, 2024, Wadely et al., 2020). In near-surface, oxygenated, euphotic waters, I^-, iodine's reduced species, concentrations are elevated at low latitudes, while IO_3^-, iodine's oxidized species, follows the opposite pattern (Chance et al., 2014). As this trend is exacerbated in near-shore waters where rates of primary production are high, it is thought that the role of biology in iodine redox transformations, such as the rapid reduction of IO_3^- to I^- by bacteria and phytoplankton in surface waters (Hepach et al., 2020, Chance et al., 2014), is important to explain basin-wide trends in iodine concentration. However, given likely slow rates of I^- oxidation (Hardisty et al., 2020, Schnur et al., 2024), it is likely that *ex situ* sources of iodine redox species distribution, such as seasonal mixing, water mass transport, and benthic inputs from upwelling and coastal systems, may contribute to observed surface iodine redox species concentrations more than previously thought. Seasonal mixing towards higher latitudes tends to be greater than in equatorial regions, therefore, the residence time of euphotic I^- at lower latitudes is longer than in less-stratified polar waters. However, constraints on reduction and oxidation rates, as well as the impacts of mixing, are limited.

Bacteria and phytoplankton are known to reduce IO_3^- to I^- in culture (Hepach et al., 2020, Moisan et al., 1994, Bluhm et al., 2010, Chance et al., 2007, Councell et al., 1997). The mechanisms and function of IO_3^- assimilation and/or reduction are not completely understood. For example, IO_3^- reduction via nitrate reductase has been previously suggested (Amachi et al., 2007, Tsunogai and Sase 1969), but recent studies have shown IO_3^- reduction by these species even when nitrate is not a limiting factor (Hepach et al., 2020) or when nitrate reductase is deactivated (Waite and Truesdale 2003, Hung and Wong 2005). Depletion of IO_3^- in surface waters of vertical profiles has also been suggested to be caused by bacteria's uptake of IO_3^-. During logarithmic growth, IO_3^- uptake has been shown to exceed I^- production, leading to a deficit or a case of "missing iodine" (Hepach et al., 2020) in the iodine mass balance. During senescence, this I^- is finally released back into the water column, indicating a lag between high primary production and I^- "production". Determination of the level of influence of primary production on the iodine mass balance is vital to constraining current observed trends of I^- distribution. Previous studies have not directly compared rates of Net Community Production (NCP) along a transect to that of iodine speciation to determine the potential role in regulating meridional iodine trends (e.g. Janssen et al., 2020). We compare rates of NCP to total vertical mixing of IO_3^- in the water column in the South Pacific here.

The assimilation of iodine in phytoplankton and bacterial biogeochemical cycles can be understood through ratios of iodine relative to leading Redfield ratio nutrients, such as carbon, nitrogen, and phosphorous (106:16:1). Values of total iodine are compared with those of carbon in phytoplankton here (I:C, $\sim 1 \times 10^{-4}$) (Elderfield and Truesdale 1980, Wadley et al., 2020, Chance et al., 2010, Jickells et al., 1988) to demonstrate the extent to which primary producers use iodine in the surface ocean. I:C ratios can be used to understand the importance of iodine assimilation and regeneration by biology in euphotic waters as it pertains to the iodine cycle and IO_3^- reduction.

Iodate formation in surface waters is known to be slow (Hardisty et al., 2020, Schnur et al., 2024, Moriyasu et al., 2023, Wadley et al., 2020, Luther et al., 1995) and is likely not formed ubiquitously across the world oceans, but punctuated within "hotspots" in space or time. Because these mechanisms of *in situ* I^- oxidation to IO_3^- (i.e. oxidation by extracellular reactive oxygen species (ROS) (Sutherland et al., 2020, Schnur et al., 2024) or by nitrifying bacteria (Hughes et al., 2021)) are likely not the leading factor in iodine redox species distribution, it is important to consider *ex situ* methods of water mass movement that likely move IO_3^- from these areas of formation into waters that would likely not otherwise have IO_3^- incorporation. Upwelling and vertical diffusion likely have a strong effect on this movement, as iodine is known to be found almost completely as IO_3^- at depth, so the upward movement of deep waters to the surface would likely have a large effect specifically on IO_3^- concentrations in surface waters. However, the rates of this movement are yet unconstrained.

As part of two complimenting cruises, measurements of iodine from GEOTRACES GP15 and GP17-OCE together provide an extremely high-resolution view of the Pacific Ocean basin relative to previous studies in any world ocean and widen our breath of understanding for euphotic iodine redox variations across areas of both *in situ* and *ex situ* influences. This is important especially in the Pacific, as it is generally under-characterized (Figure 2.4) in regards to iodine. Several studies in recent years have revealed iodine's importance and cycling complexities within the Pacific through high-resolution transects covering regional ODZs (Moriyasu et al., 2023, Moriyasu et al., 2020, Cutter et al., 2018 Evans et al., 2024), however, more studies are needed from well-oxygenated settings that characterize most of the ocean.

A major part of the GEOTRACES mission is to understand the distribution and cycles of trace elements and their isotopes (TEIs). As part of the "key" parameters for GP17-OCE, ^{7}Be was measured to calculate the impact of *ex situ* vertical flux of nutrients and TEIs into and from the mixed layer. These measured values of ^{7}Be were used in combination with the value of the mixed layer depth (MLD) for each station to measure the upwelling (w) and vertical diffusion (K_z) rates of individual stations along the GP17-OCE transect. ^{7}Be ($t_{1/2}$ = 53.3 days) can be used in conjunction with IO_3^- distribution in the water column to quantify the movement of iodine from deeper waters to the surface, as it is known that I^- oxidation to IO_3^- does not occur quickly, and possibly not ubiquitously (Schnur et al., 2024), in the surface ocean. Moriyasu et al. (2023) completed similar calculations from two stations during GP15 which provide an initial framework that we expand in our study. NCP – measuring the difference between gross community production and respiration of organisms – was also measured, and is also used for calculations of a mass balance of the Southern Pacific Ocean, specifically in calculation of an I^- oxidation rate (F_{ox}) and iodine/carbon (I:C) ratio for the South Pacific, here.

We are completing measurements of IO_3^- across the entire surface of the GP17-OCE transect with applications for ^{7}Be , NCP, and IO_3^- depth profiles measured at 12 stations (GP17-OCE only) and surface iodine measurements at 109 stations from across GP15 and GP17-OCE. These data, combined with IO_3^- depth profile values from GP15 from Moriyasu et al., 2023 – provide a full understanding of iodine across the Pacific Ocean at 152°W from 56°N to 67°S. We interpret these sea surface iodine speciation trends in the context of regional primary producers, nutrient dynamics, and circulation. For the southern Pacific, we perform a mass balance to calculate a phytoplankton iodine:carbon (I:C) ratio and I^- oxidation flux (F_{ox}).

2.3: Methods

2.3.1 Sample collection

In this study, we measured surface water IO_3^- , I^-, and dissolved organic iodine (DOI) from the combined GP15 and GP17-OCE transects and depth profiles of IO_3^- from GP17-OCE, which are combined with those previously published from GP15 (Moriyasu et al., 2023). Northern Pacific surface seawater samples (GP15) were collected by the R/V *Roger Revelle* from 36 stations and 18 intermediate stations (surface FISH samples only) between the Alaskan shelf and Papeete, Tahiti (Figure 2.1) between the dates of September 18, 2018 – November 24, 2018, using a towed fish ("Geo-fish") extended off the side of the ship in conjunction with the ship's flow-through seawater system at 0 m. Surface FISH samples were taken within one hour of arrival at both profile stations and midway between profile stations. A total of 54 surface-only samples were collected for trace element – including iodine speciation – measurements using the Go-fish and stored in 60 ml, semi-opaque, wide-mouth HDPE bottles that were sealed with parafilm. GP15 completed a meridional transect from 56°N to 20°S following a path directly south along 152°W. Fresh seawater was directed through Teflon tubing to a filtration manifold in the shipboard main lab clean bubble. Seawater was filtered sequentially through a 0.45 µm, 10" filtration cartridge then a 0.2 µm, 10" cartridge and directly sampled for contamination-prone TEI's, including iodine. Samples were frozen at -20°C and stored upright and in the dark for transport from Papeete, Tahiti, and stayed frozen through transport back to Michigan State University where they remained frozen for storage until iodine redox species measurement occurred nine months later. It has been reported that frozen samples show no signs of total iodine degradation over the duration of one-to-three-year periods assessed (Campos 1997, Farrenkopf et al., 1997, Hou et al., 2001, Jickells et al., 1988).

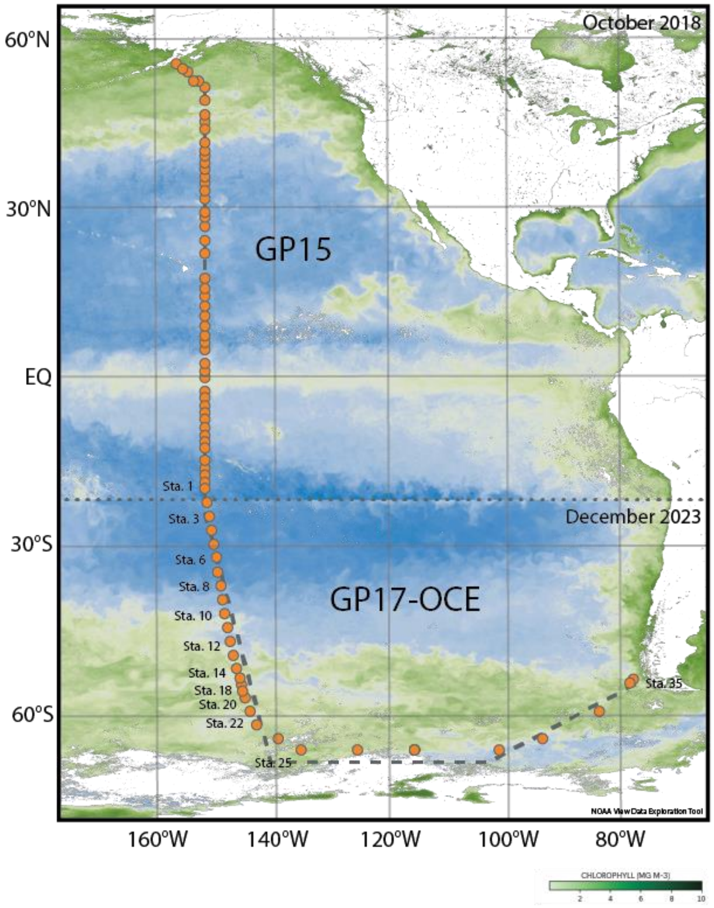

Figure 2.1 Station map of combined GEOTRACES GP15 (RR1814) and GP17-OCE cruises. Dashed line denotes GP15 cruise end/GP17-OCE cruise beginning stations. Stations with ^{7}Be measurements are denoted by station number. Chlorophyll data from NOAA View Data Exploration Tool.

Southern Pacific seawater samples (GP17-OCE) were collected by the R/V *Roger Revelle* from 54 stations linking Papeete, Tahiti, and Punta Arenas, Chile (Figure 2.1), between the dates of December 1, 2022 – January 25, 2023, from an onboard CTD using SIO STS 36-place yellow rosette and bottles. Samples were collected for iodine speciation measurements from the GEOTRACES Trace Element Carousel sampling system (GTC) rosette, in opaque, amber, 125 ml high-density polyethylene (HDPE) Nalgene bottles that were pre-rinsed three times with 18.2 MΩ water (MQ) before shipment on GEOTRACES GP17-OCE. GP17-OCE completed a meridional transect from 20°S to 67°S, beginning with a "crossover" station with GP15 at 20°S 152°W. At 67°S, a switch to a zonal transect was completed, turning north towards Punta Arenas on January 12th. FISH sampling was completed at all stations sampled for depth profiles and also at six individual "FISH only" stations in-between depth profile stations. FISH samples were taken at a depth of three meters and serve as a surface sample for all depth profiles (Figure 2.4). Stations where depth profiles were collected were classified as Demi, Full-24, or Super, with 12, 24, or 36 samples collected for each, respectively, and one ending shelf station with six samples collected. Samples were filtered using Acropak-500 0.8/0.2 µm capsule filters for removal of biological or particulate material. Samples were frozen and stored upright in coolers for transport from Punta Arenas, Chile to Michigan State University where they were kept frozen in storage until iodine redox species measurement occurred.

2.3.2 Analytical Methods

2.3.2.1 Spectrophotometry

60 ml (GP15) and 125 ml (GP17-OCE) sample bottles were briefly thawed and ~10 ml from all were subset in 15 or 50 ml Falcon tubes, respectively, for measurement on spectrophotometer before the remaining ~50/~115 ml were re-frozen for storage. Iodate from all surface (FISH) (GP15) and FISH and depth profile samples from stations measured for ^{7}Be (GP17-OCE) (stations 1, 3, 6, 8, 10, 12, 14, 18, 20, 22, 25, and 35) were measured using Jickells' (1988) spectrophotometric method at a 2.5 ml final sample volume, as outlined in Schnur et al., 2024. 10% KI used in the method was made fresh daily for sample measurements, while 1.5 M sulfamic acid (H_3NSO_3) was made fresh monthly, as needed. A standard curve slope ($m_{standardcurve}$) was recorded daily with known samples between zero and 500 nM potassium iodate (KIO_3^-) in DI water measured. Triiodide (I_3^-) produced from the reaction described above is specific to IO_3^- (Jickells 1988, Moriyasu et al., 2020, Moriyasu et al., 2023). Iodate peaks and troughs were measured between 320 and 400 nm $(A(IO_3^-)_x)$ for calculation of IO_3^- nM values $(nM_{IO_3^-})$ in samples using the equation:

$$nM_{IO_3^-} = (A(IO_3^-)_{350} - (A(IO_3^-)_{320} + A(IO_3^-)_{400})/2) * m_{s\tan dard\ curve}$$

Standard curve slopes and absorbance values at specified nm values were used to calculate nM [IO_3^-] values for all samples. Measurements were made on a VWR UV-Vis Scanning 3100 PC spectrophotometer and accompanying UV-Vis Analyst software using VWR®.

GP15 surface FISH samples were measured using two-sided disposable plastic cuvettes for measurements within the visible range (300-900 nm), path length 10 mm. Duplicates of samples were run with good consistency and agreement. GP17-OCE FISH and depth profile samples were measured similarly, all in duplicate, using Fisherbrand® Semi-Micro Quartz Cuvettes (Cat. No. 14-958-126), path length 200-2500 nm.

2.3.2.2 Ion Chromatography and ICP-MS

Dissolved Organic Iodine (DOI) was measured in all surface samples from GP15. Iodide was measured in all surface samples from GP15 and GP17-OCE, but not in depth profiles of GP17-OCE. To separate I^- and DOI from seawater samples, a previously established ion-exchange chromatography method was used, as is described in Chapter 1 of this dissertation (Schnur et al., 2024, Wong and Brewer, 1977, Hou e al., 1999, Hou et al., 2007, Hou et al., 2009, Hardisty et al., 2020, Hardisty et al., 2021, Moriyasu et al., 2023). Separated I^- and DOI fractions were measured via ICP-MS as I^- in each sample described above. Yields from I^- measurements on ICP-MS are known to reach ~100% (Hardisty et al., 2020). Glass columns used for iodine redox species separation were packed with PYREX glass wool and 1 ml (volumetric) AG1-X8 resin that was cleaned of any residual iodine after packing using one full ion-exchange chromatography "cleaning" procedure (substituting sample for 18.2 MΩ-cm water) before samples were run through columns for collection of iodine redox species using the same chromatography procedure. About 10 ml of each sample – of which the mass was quantified gravimetrically before addition – were used during each procedure.

The ion chromatography procedure specifically elutes I^- from the seawater matrix. DOI was separated from whole seawater via specific chromatography steps (Hardisty et al., 2020) and reduced to I^- before ion chromatography eluded DOI as I^- for measurement. For quality control, at least one 200 ppb I^- solution diluted from a 1000 ± 4 ug/ml I^- solution in 1% tetraethyl ammonium (TEA) standard was run alongside samples through columns as a monitor of iodine elution efficiency from columns to estimate yields. At least two 18.2 MΩ-cm water blanks were also run as monitors of contamination with sample sets. At least one sample replicate was also included in each column set for assessment of reproducibility between column runs.

Iodide concentrations for GP15 and GP17-OCE samples were measured after separation by column chromatography using a Thermoscientific iCap triple-quad inductively coupled plasma mass spectrometer (ICP-MS-TQ) using Qtegra software version 2.10.3324.131 in both single-quad (SQ) and triple-quad (TQ) mode with O_2 reaction cell gas. A Teledyne ASX520 autosampler was used to deliver liquid solution to ICP-MS. Samples were diluted 1:20 or 1:40 in a 0.9% tetramethyl ammonium hydroxide (TMAH)/0.1 M nitric acid (HNO3) or 0.45% TMAH/0.05 M HNO_3 solution, respectively. The same dilutions were used for ICP-MS rinse solutions. Data was corrected relative to the internal standards In, Rh, and Cs. Internal standards used were from

Inorganic Ventures© – In was a 1001 ± 3 µg/ml solution in 2% HNO3; Rh was a 999 ± 5 µg/ml solution in15% HCl; and Cs was a 1000 ± 4 µg/ml solution in 0.1% HNO – to create a 5 ppb internal standard solution that was spiked into each measured sample directly or using an inline mixing chamber. The I^- standard used for creating standard curves and column standard samples was a 1000 ± 4 µg/ml I^- solution in 1% tetraethylammonium (TEA).

2.3.3 Mass Balance of the Southern Pacific Ocean

2.3.3.1 Regression for determining iodine oxidation and organic assimilation

For the GP17 stations only, iodine-carbon (I:C) ratios and I^- oxidation rates (F_{ox}) are calculated via a mass balance from IO_3^- values across the euphotic zone (Equation 2.1). Equation 2.1 assumes that upwelling (w), vertical diffusion (K_z), and primary production (NCP and $r_{I:C}$) and oxidation/reduction (F_{ox}) are the main factors impacting the iodine cycle in these waters. The equation and parameters used to estimate I:C and F_{ox} are adapted for iodine from Kadko 2017's description of ^{7}Be values over depth in the open Pacific Ocean water column, using values of IO_3^- over depth and at the base of the euphotic zone ($[IO_3^-{}_{euph}]$) and using calculated values of NCP (Figure 2.2). By assuming steady state, this equation can be simplified to form of a linear line, where the merged upwelling/advection term (F_{mix}) and NCP are y and x respectively, and are measured parameters that can be used to solve for the slope and intercept ($r_{I:C}$ and F_{ox}, respectively).

$$F_{net} = 0 = \left\{ w * [IO_3^-]_{euph} + K_z * \left(\frac{\delta IO_3^-}{\delta z}\right)_{euph} \right\} - NCP * r_{I:C} + F_{ox} \qquad \textit{Equation 2.1}$$

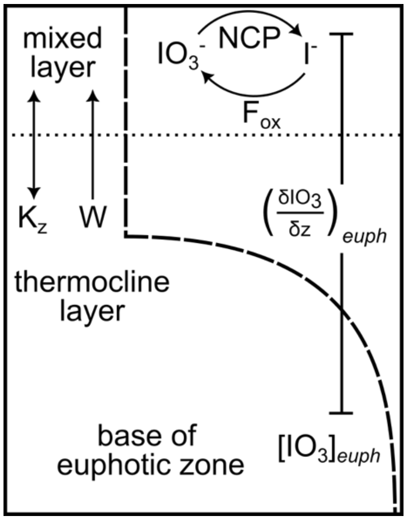

Figure 2.2 Representation of values used in Equation 2.1 for mass balance calculation. Dotted line indicated depth of the mixed layer, while top solid line represents air-sea boundary. Base of euphotic zone is represented by bottom solid line of figure.

This equation assumes that a single value for an I:C ratio and oxidation/reduction rate are fully representative of the whole transect, which is represented by a linear regression of values of calculated NCP and F_{mix}, equaling the first section of Equation 2.1, which includes values for upwelling (w), vertical diffusion (K_z), [IO_3^-] at the base of the euphotic zone, and [IO_3^-] over depth from the base of the mixed layer to the base of the euphotic zone (Equation 2.2). Details for the origin of w and K_z are given in section 2.3.3.2.

In this regression, the calculated value for the regression slope is $r_{I:C}$ – the rate at which iodine is incorporated into primary producers. The intercept is F_{ox}, the IO_3^- formation rate in mmol m^{-2} d^{-1}. Contributions of IO_3^- were calculated using concentrations of IO_3^- at the base of the euphotic zone ($[IO_3^-]_{euph}$), IO_3^- concentrations over a gradient ($\left(\frac{\delta IO_3^-}{\delta z}\right)_{euph}$), and calculated NCP used to find the I:C ratio (iodine that has been incorporated into primary producers, bacteria and phytoplankton ($r_{I:C}$)), and the oxidation rate of I^- (F_{ox}) (Equation 2.1). The base of the euphotic zone was established at each station individually using a deterministic approach of fluorescence through the water column, where the end of the euphotic zone is signaled by a return to the level of noise after fluorescence peak, in most cases, a return to ~0.017 V (Figure 2.5) (Kadko 2017, Marra et al., 2014). The closest available iodine sample from each calculated depth was used to determine gradients of iodine concentration over depth. Gradients were simply calculated using:

$$\frac{[IO_3^-]_z - [IO_3^-]_H}{z_z - z_H} \quad \textit{Equation 2.2}$$

where z is the bottom of the particle production zone (PPZ) (Kadko 2017) or the depth at which the measured fluorescence returns to background from peak (Figure 2.5), and H is the measured MLD for the station (Table 2.3).

2.3.3.2 ^{7}Be as a means of assessing upwelling (w) and vertical diffusion (K_z) rates

^{7}Be was measured at 12 vertical profile stations (Figure 2.1) and data is available: https://www.bco-dmo.org/project/920228?&order=field_deployment_name&sort=desc. Calculated values of upwelling (w) and vertical diffusion (K_z) were provided via collaboration. Below we summarize these calculations and implications for iodine.

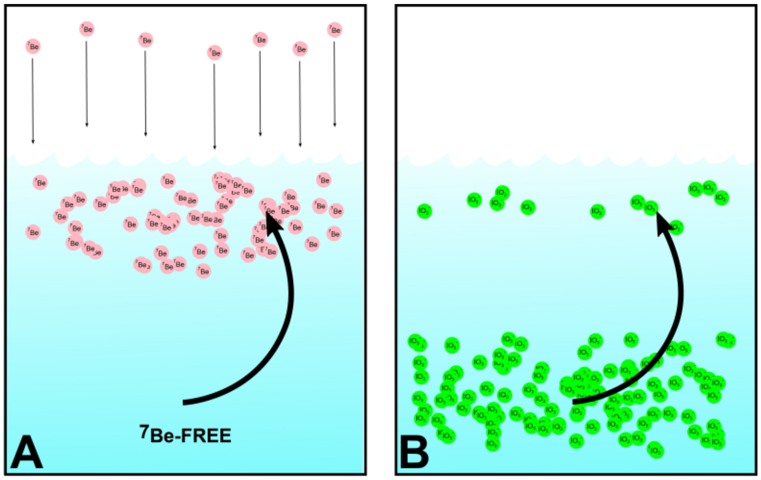

Figure 2.3 ^{7}Be ($t_{1/2}$ ~53 days) can be used to infer upwelling (w) and vertical diffusion (K_z) rates as a result of dilution in water column [^{7}Be] from upwelled ^{7}Be-free deep waters (A). The flux of IO_3^- into IO_3^--poor euphotic waters from rich deep waters can be traced using ^{7}Be calculated w and K_z values (B).

The mixing portion of Equation 2.1 requires constraints on vertical diffusion and advection. ^{7}Be can be used as this tracer. ^{7}Be is deposited on the sea surface through precipitation and stays condensed there as its short half-life ($t_{½}$ ~53 days) does not allow for diffusion to deeper depths (Figure 2.3). While upwelling of ^{7}Be-free bottom waters occurs through mixing in the water column, the resulting dilution of ^{7}Be in surface waters can be used to infer upwelling (w) and vertical diffusion (K_z) rates using methods from Kadko et al., 1996, 2011, 2017, and 2020. Using the inventory of ^{7}Be through the water column at specific GP17-OCE stations and knowledge of the mixed layer depth (MLD) at these stations (Table 2.3), it is possible to calculate the rate of upwelling and vertical diffusion occurring at these sites. These rates directly affect the distribution of trace elements, such as iodine, in the Pacific basin. With them, we are able to predict the total advected and diffused IO_3^- through the water column and calculate the overall oxidation rate and uptake of iodine into primary producers (I:C), thereby determining the mass balance of iodine for the Southern Pacific basin (section 2.3.3.1, Equation 2.1).

Site-specific measurements of MLD and [^{7}Be] for both the bulk station and just below the mixed layer, and a known decay constant of 0.13 day^{-1} were used for calculation of the basin mass balance by first being used to calculate upwelling (w) and vertical diffusion (K_z) rates at these specific stations (Kadko and Olson, 1996, Kadko 2017). Calculations by collaborators were completed using the procedure of Kadko and Olson (1996), starting with the one-dimensional numerical model:

$$^7Be(z) = \quad ^7Be_0 e^{-(\lambda/K_z)^{1/2} z} \qquad \textit{Equation 2.3}$$

Where ^{7}Be(z) is the ^{7}Be activity at any depth (z) below the mixed layer, $^7Be_0$ is the ^{7}Be activity at the base of the mixed layer, λ is the decay constant of ^{7}Be described above, and K_z is the apparent vertical diffusion coefficient.

Outside the equatorial region, the one-dimension numerical model described by Equation 2.3 and a Monte Carlo method using these calculations to determine the best fit K_z was used for calculations at each station, where K_z is assumed constant over depth and time. The model to calculate initial K_z values was initialized with a zero ^{7}Be inventory on January 1, 2018, and run until the sampling date nine to 11 months later; for more than five half-lives of the isotope. For the Monte Carlo approach, a random value of F (where F = λ*inventory) for Equation 2.5 was chosen based on its measured mean and standard deviation (assuming a normal distribution). A value of K_z was chosen between 0 and 15x10^{-5} m^2/s in 0.5x10^{-5} m^2/s increments (30 K_z values) and the depth profile of ^{7}Be concentration was determined. K_z values producing the least root mean square deviation were recorded. This technique was repeated for n = 10000 model runs with varying values of F. The resulting mean and standard deviation of best fit K_z values was determined. Equation 2.4 below describes the calculations done for ^{7}Be depreciation over the first 150 m of the water column (represented by 150 boxes (i) of 1 m depth (z) each at Δt = 0.005 d), while Equation 2.5 is used to explain all depths deeper than 150 m.

$$\Delta C_1 \; = \{ \frac{F}{z} - \lambda \bullet C_1 \; + K_z \bullet [C_2 - \; C_1] \, \} \bullet \Delta t_2 \qquad \textit{Equation 2.4}$$

$$\Delta C_i \; = \{ - \lambda \bullet C_i \; + K_z \bullet \frac{[C_{i+1} - 2 \bullet C_i + C_{i-1}]}{z_{i2}} \} \bullet \Delta t_3 \quad \textit{Equation 2.5}$$

MLDs for these calculations were obtained from the Japan Agency for Marine-Earth Science and Technology Mixed Layer Data Set of Argo Grid Point Value (JAMSTEC MILA GPV), which provides monthly average MLD from Argo profile data on a 1° x 1° grid (Hosodo, 2010).

It is also possible to determine vertical diffusion rates calculated by nonlinear regression of [^{7}Be] with depth below the mixed layer (Figure 2.2), with a single station (here, station 25) designated as an offshore “non-upwelling” station by way of the methods of Kadko 2017, where the ^{7}Be inventory is non-decreasing or changes the least for all of the stations measured. These calculations were done in parallel, and values for K_z and were found to be corresponding to those from collaborators for all stations. Calculation of K_z was begun using a one-dimensional vertical advection-diffusion equation, as described in Kadko (2017):

$$C_z = C_0 e^{-\alpha * (z-H)} \qquad \textit{Equation 2.6}$$

where H is equal to the found mixed layer depth (MLD) of the station, C_0 is equal to a constant [^{7}Be] within the mixed layer, and C_z is equal to the [^{7}Be] at any depth below the mixed layer, which eventually decays to zero at some depth z. The value of α that is calculated from the nonlinear regression of Equation 2.6 is used for the derivation of K_z in the method of Kadko 2017.

Upwelling (w) values were determined using the equation:

$$w = \left(\frac{1}{C_0}\right) * \left(f - (\lambda * C_{inv})\right) \qquad \textit{Equation 2.7}$$

Where λ is the ^{7}Be decay constant, 0.13 day^{-1}, and f is λ multiplied by the ^{7}Be inventory of the chosen “non-upwelling” station. The change in inventory of ^{7}Be of individual upwelling stations relative to that of the designated “non-upwelling” station allows us to determine the upwelling rate, as it is used to assume the unchanging atmospheric flux of ^{7}Be into the surface layer (Kadko 2017). Changes due to horizontal advection were not considered for these calculations. Our results compare well to similar studies (Table 2.1) using this and similar methods for calculation of upwelling in open ocean regions.

Site	Upwelling rate (m/d) with 0 m/s horizontal advection rate	Citation
Peruvian Coastal Upwelling Region	0-3	Kadko 2017
South Pacific Ocean basin	0-3.71	This study; Stephens and He (2024)
Coastal Peru and Mauritania	0.95-2.42	Steinfeldt et al., 2015

Table 2.1 Comparison of range of upwelling rates found between this and previous studies.

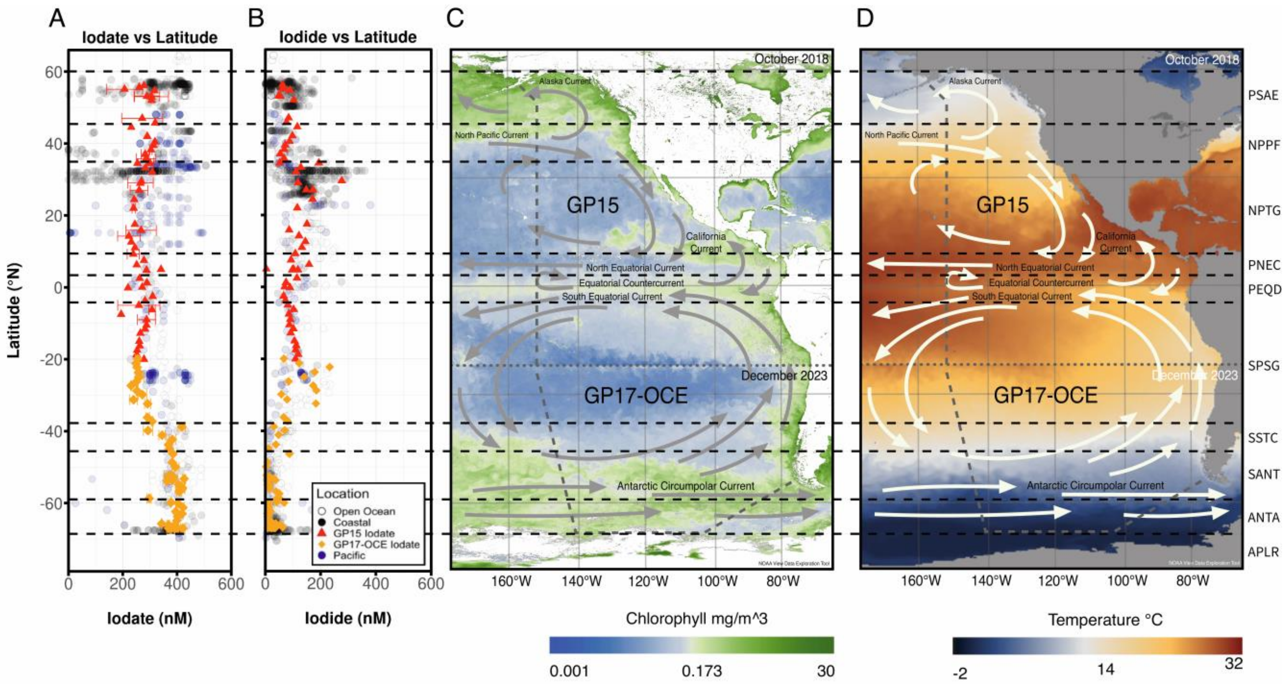

Figure 2.4 Measured GP15 (red triangle) and GP17 (orange diamond) surface A) IO_3^-, and B) I^- concentrations overlayed on Chance et al., 2014, Sherwen et al., 2019, and Huang et al., 2005 iodine latitudinal profile data; Cruise tracks of GP15 (RR1814) and GP17-OCE overlaid on C) chlorophyll distribution and D) sea surface temperature at time of sampling throughout basin. Latitudinal lines are equal through the entire figure, starting from the left. Major ocean currents possibly impacting iodine distribution outlined in gray with pointed direction. Gray vertical/horizontal dashed line denotes GP15 cruise end/GP17-OCE cruise beginning stations. Yellow horizontal dashed lines indicate changes in Longhurst (Longhurst, 2007) regime for biogeochemical provinces (indicated right) that GP15 and GP17-OCE traversed during cruises.

Zone	Full Name	Biome
PSAE	Eastern Pacific subantarctic gyres	Westerly
NPPF	North Pacific polar front	Westerly
NPTG	North Pacific Tropical gyre	Trade Wind
PNEC	North Pacific equatorial counter current	Trade Wind
PEQD	Pacific equatorial divergence	Trade Wind
SPSG	South Pacific gyre	Trade Wind
SSTC	South subtropical convergence	Westerly
SANT	Subantarctic water ring	Westerly
ANTA	Antarctic	Polar
APLR	Austral polar	Polar

Table 2.2 Full names and assigned biomes of Longhurst biogeochemical zones traversed by GP15 and GP17-OCE as found in Figure 2.4.

2.4: Results

2.4.1 Iodine speciation

2.4..1.1 FISH iodine speciation across a full Pacific meridional transect (GP15 and GP17-OCE)

Iodine speciation is reported here for the Pacific Ocean basin from 56°N to 67°S, completing a high-resolution iodine meridional transect of the Pacific Ocean at 152°W. Surface ocean values of I^-, IO_3^-, and DOI are reported for GP15 (red triangles) and $[I^-]$ and $[IO_3^-]$ are reported for GP17-OCE (orange diamonds) (Figure 2.4, Figure 2.9). These values reported alongside previous iodine data from the Pacific (Chance et al., 2014, Sherwen et al., 2019, Huang et al., 2005), provide further context and allow for comparison of iodine species' concentrations over time and in a similar basin. New GP15 and GP17-OCE $[IO_3^-]$ and $[I^-]$ data reported here generally overlap with previously reported Pacific iodine species trends and allow for a critical interpretation of iodine in the undercharacterized Pacific Ocean at a single longitude. DOI measured over the GP15 latitudinal transect shows that there is an active DOI pool of iodine in the surface ocean in the North Pacific, and that pool may be higher in concentration than previously thought for the open ocean (Wong and Cheng 1998, Chance et al., 2020).

2.4.1.2 Iodine speciation in depth profiles (GP17-OCE, GP15; 0-500 m)

Depth profiles of $[IO_3^-]$ (nM) from stations where ^{7}Be was also measured (stations 1, 3, 6, 8, 10, 12, 14, 18, 20, 22, 25, and 35) are detailed in Figures 2.6 and 2.7. Stations show predictable change over latitude for IO_3^- distribution with depth, with values at lower latitudes reaching ~400 nM consistently in deeper waters (Chance et al., 2014). Profiles show typical outlines of iodine through the water column, as IO_3^- is elevated at depth, and shows the influence of the euphotic zone clearly – where bacteria and phytoplankton are known to reduce IO_3^- to I^- concentrations (Hepach et al., 2020, Chance et al., 2014).

Station	**Latitude**	**Longitude**	**H (MLD) (m)**	**Alpha**	**λ (/day)**	**Rate of vertical diffusion (K_z) (m^2/s)**	**Upwelling rate (w) (m/s)**
1	-20	-152	14	0.0139	0.013	5.7E-04	0
3	-25	-151.25	20	0.00772	0.013	9.31E-04	1.01
6	-32.5	-150	40	0.01861	0.013	4.60E-04	0.043
8	-37.5	-149.28	44	0.02654	0.013	1.73E-04	0.15
10	-42.5	-148.47	10	0.01667	0.013	4.6E-04	0.25
12	-47.5	-147.52	38	0.01797	0.013	1.2E-04	0.84
14	-52.3	-146.4	77	0.02480	0.013	4.59E-05	1.48
18	-56.3	-145.28	34	0.00525	0.013	1.3E-03	3.71
20	-57.6	-144.86	46	-	0.013	-	-
22	-60	-144	58	0.00773	0.013	2.37E-04	1.67
25	-67	-134.99	18	0.17230	0.013	5.02E-05	2.19
35	-54.35	-76.55	26	0.00757	0.013	8.89E-04	0.95

Table 2.3 Values of mixed layer depth (MLD), calculated alpha, vertical diffusion rates (K_z) and upwelling rates (w) for stations with measured ^{7}Be. Station 20 is omitted because of a torn hose that led to compromised data, so calculations for this station could not go further. These values assume zero horizontal flux (F).

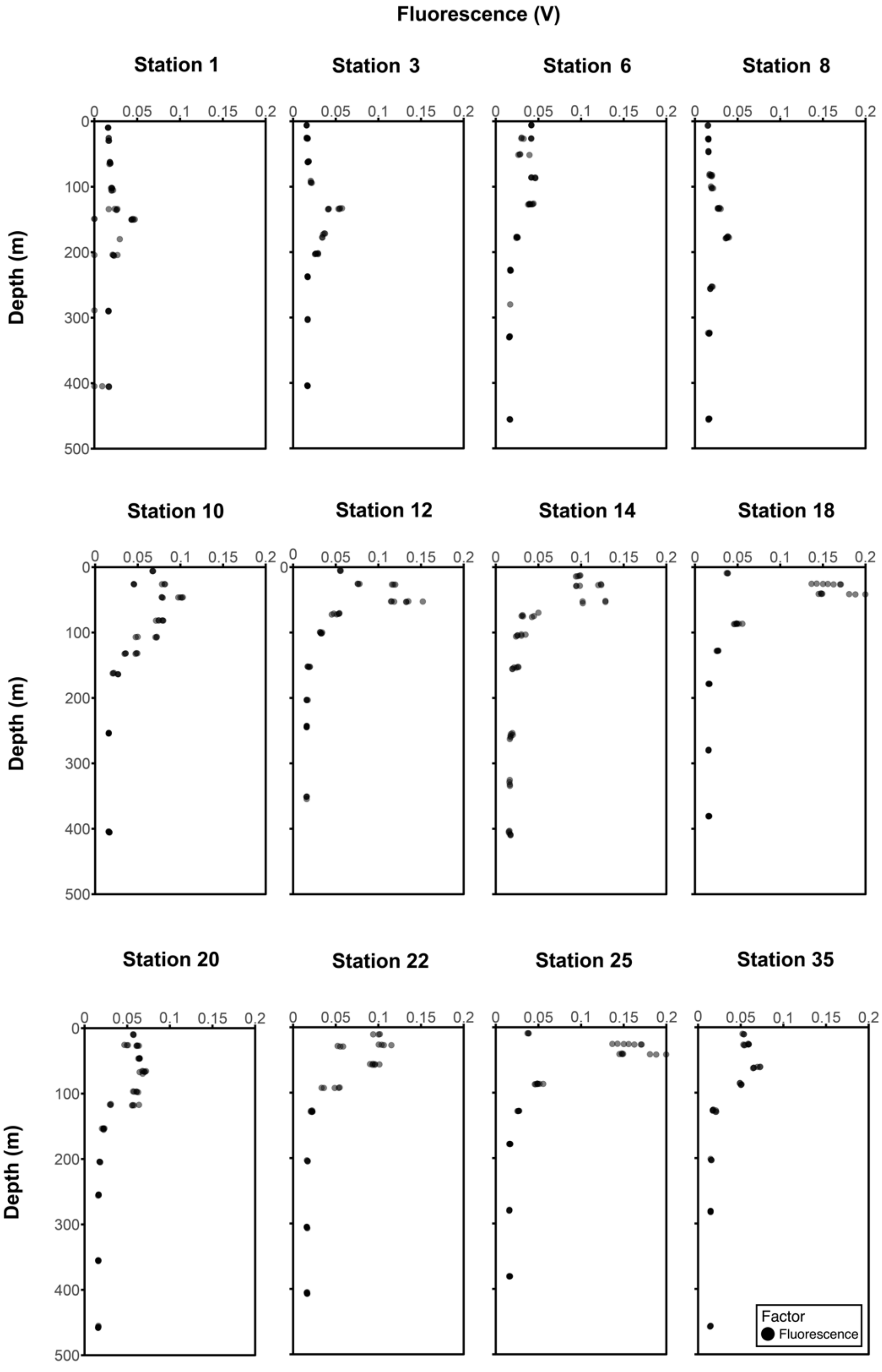

Figure 2.5 Fluorescence over depth at stations with $[^{7}\text{Be}]$ measurements. The bottom of the partial production zone (PPZ) is defined as z (Table 3.3), the depth at which fluorescence returns to background noise; here, about 0.017 V at each station measured for ^{7}Be.

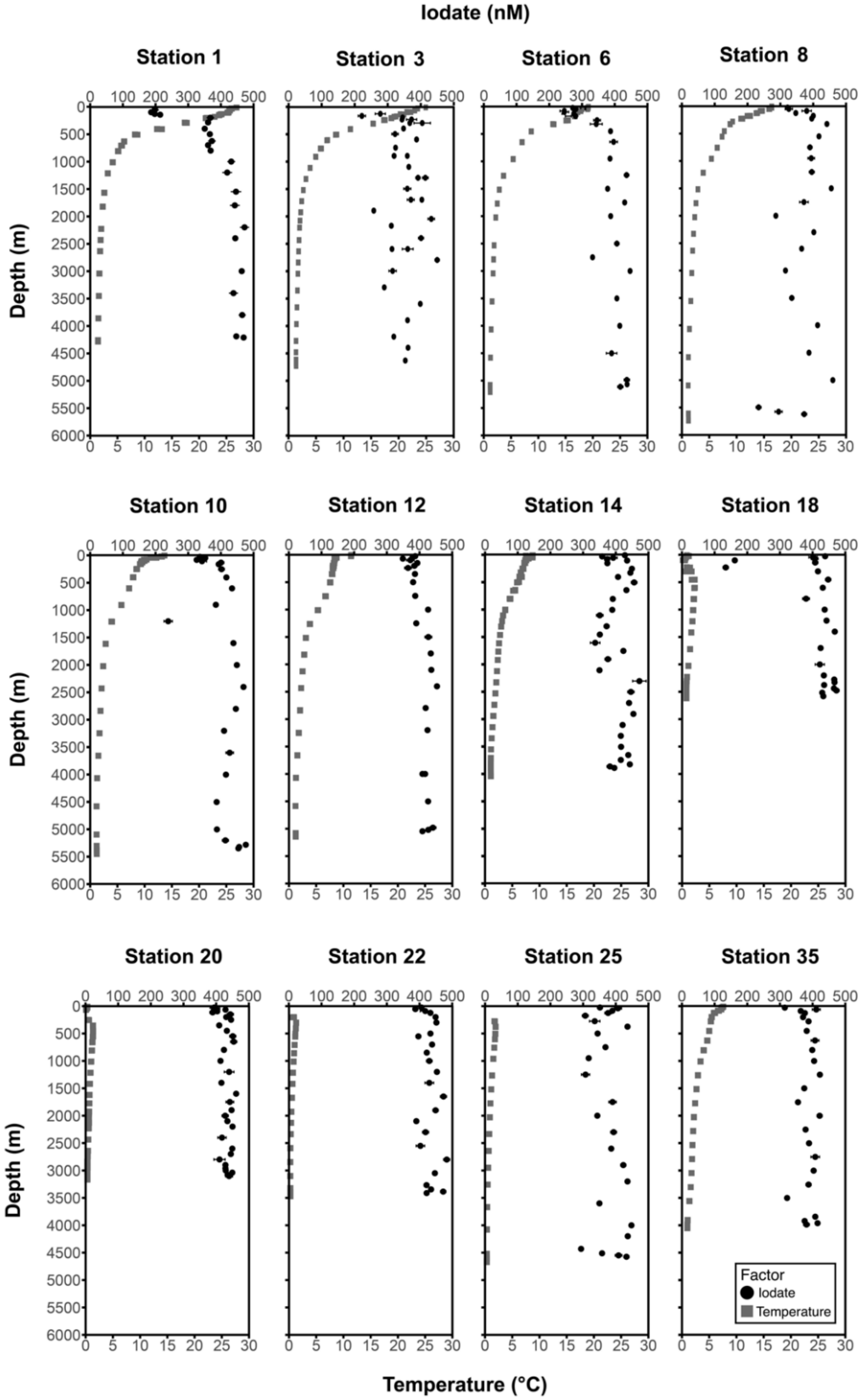

Figure 2.6 Depth profiles of [IO_3^-] (black circles, nM) from selected GP17-OCE stations where [^{7}Be] is also available. Note that Station 1 is in equatorial waters, with an increase in latitude corresponding with increase in station number. Stations in high-latitude waters show great consistency with depth of [IO_3^-] values, at ~400 nM. Temperature values (gray squares, °C) for each depth profile are included for each plot with a secondary x-axis (bottom). Vertical diffusion (K_z) rates are found to be highest at stations 3, 18, and 35, which may explain some of the variability in concentration seen at Station 3 with depth.

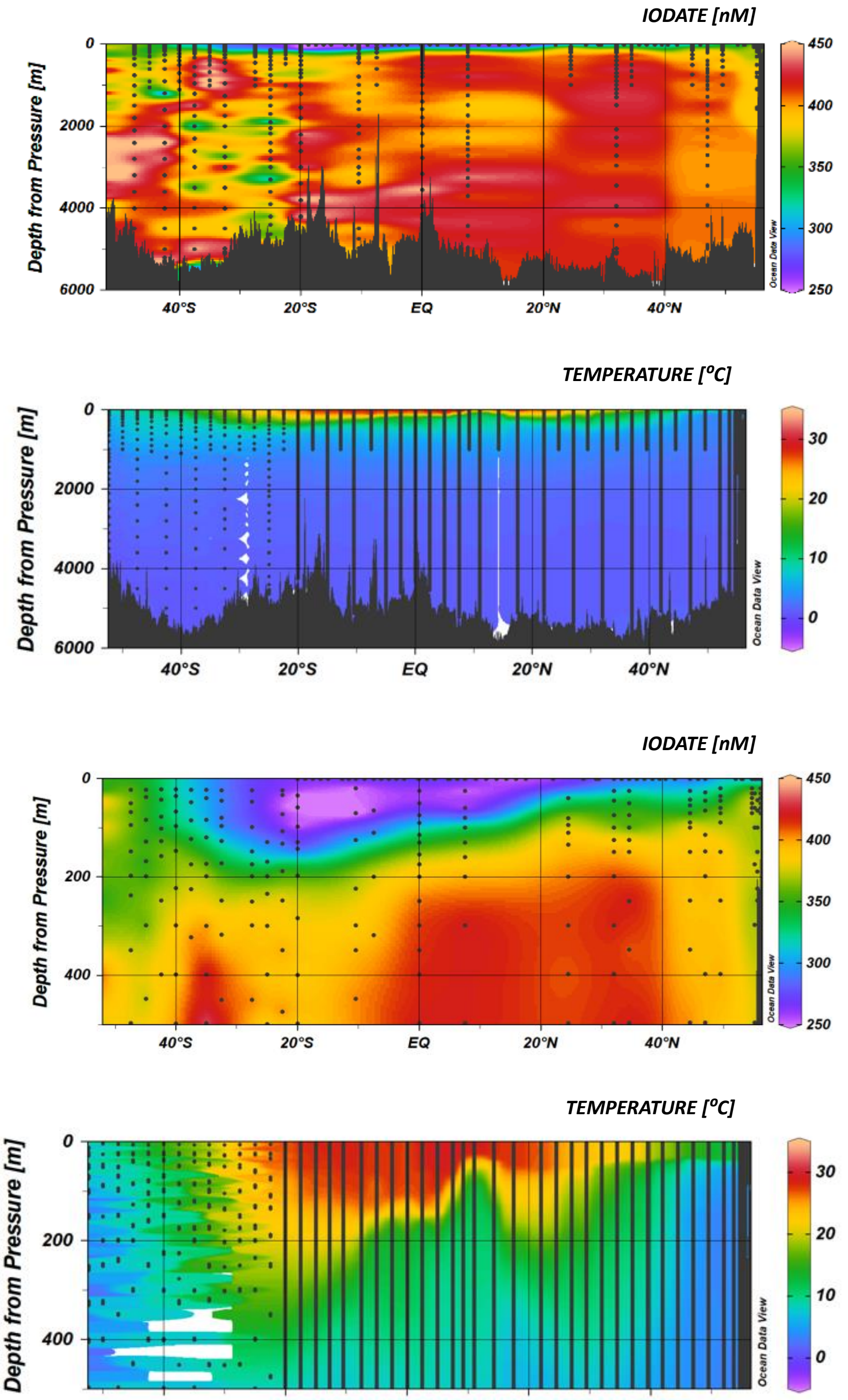

Figure 2.7 Interpolation of IO_3^- and temperature (ºC) with depth (6000 and 500 m) in the water column along the GP15 and GP17-OCE cruise track.

2.4.2 Calculations from mass balance components

Upwelling (w) and rates of vertical diffusion (K_z) were calculated from methods outlined above (section 2.3.3.2) and are used moving forward to aid in calculations of I:C and F_{ox}, along with the [IO_3^-] data found from measurement of these specific depth profiles, for calculation of a mass balance of the Southern Pacific Ocean basin. Results for each station are shown in Table 2.3. A mass balance for calculating I:C ratios during primary production and I^- oxidation flux in euphotic waters was completed for the Southern Pacific Ocean using methods from Kadko (2017, Kadko and Olson 1996) and Hardisty (2020). Rates of w and K_z were calculated using methods from Kadko (2017) and Kadko and Olson (1996), where a value of F, describing the observed ^{7}Be inventory, was randomly chosen based on its measured mean and standard deviation assuming a normal distribution across the water column. Horizontal advection was set at 0 m/s for these upwelling calculations. From the mass balance, F_{ox} was calculated at 0.23 mmol m^{-2} d^{-1}, and the I:C ratio for the South Pacific was calculated at 1.2×10^{-2} (Figure 2.8).

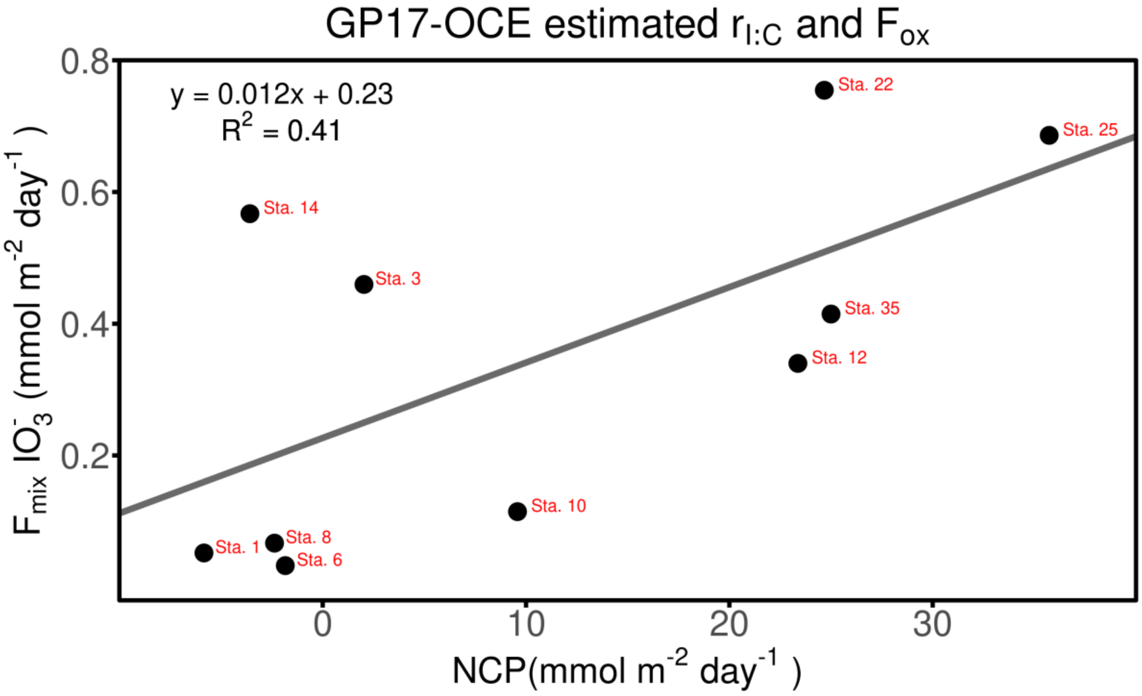

Figure 2.8 Net community production (NCP) of each station plotted against F_{mix}, the multiplicative section of Equation 2.7 that includes values for upwelling (w), vertical diffusion (K_z), [IO_3^-] at the base of the euphotic zone, and [IO_3^-] over depth from the base of the mixed layer to the base of the euphotic zone. Values for $r_{I:C}$ and are calculated from the linear regression found of all stations (excluding station 18) sampled for ^{7}Be and IO_3^-. This calculation assumes a singular value for both I:C ratio and F_{ox} for all stations.

Station	z (m)	IO_3^- depth	$[IO_3^-]_{euph}$ (nmol)	$\left(\frac{\delta IO_3^-}{\delta z}\right)_{euph}$ (nmol/m)	NCP ($mmol/m^2/d$)
1	242.214	200.3	367.78	1.03	-5.84
3	295.5624	236	372.12	0.91	2.03
6	258.2594	249.9	346.01	0.43	-1.84
8	231.7896	225.3	395.52	0.40	-2.37
10	258.8726	250.1	401.97	0.29	9.58
12	207.2616	149.7	393.31	0.15	23.37
14	255.2	149	374.28	0.01	-3.58
18	145.5328	139.7	407.97	0.07	-22.66
20	208.488	150.1	443.30	0.43	12.84
22	208.8968	124.1	433.39	0.65	24.67
25	182.427	175.2	306.62	-0.30	35.73
35	129.3852	124.6	376.31	0.62	25.00

Table 2.4 The base of the euphotic zone is based on the point at which the fluorescence decreases to background levels (~0.017 V) after peak fluorescence shown in Niskin bottle depth profiles from GP17-OCE.

2.5: Discussion

2.5.1 Temporal and methodological iodine comparison

Although some past studies have measured iodine redox species in specific sections of the Pacific Ocean (Figure 2.6), our study, combined with that of Moriyasu et al., 2023, is the most comprehensive study of iodine across the Pacific Ocean to date. Our new redox species concentration data provide a wholistic framework for euphotic iodine speciation across the Pacific Ocean. The observed trends of iodine at 152°W with latitude across the Pacific basin follow the generate pattern observed in this and other ocean basins (Chance et al., 2014, Wadley et al., 2020), but also provide insights into drivers of this distribution. In general, at lower latitudes where higher sea surface temperatures increase stratification, iodine speciation is in disequilibrium, with elevated [I^-] relative to the oxidized [IO_3^-] (Chance et al., 2014) (Figure 2.4). The *in situ* reduction of IO_3^- to I^- by phytoplankton and bacteria in surface waters drives initial I^- accumulation at the sea surface. We hypothesize that a combination of slow oxidation kinetics of I^- and vertical mixing with high -IO_3^- sub-photic waters play an additional important role in euphotic iodine speciation distribution with latitude.

Iodine speciation is assessed here across diverse biogeochemical gradients as defined by Alan Longhurst (2007), as areas of high primary productivity, ODZs and pore waters that may be sources of iodine redox cycling (Figure 2.4). Surface samples measured for iodine redox transect measurements and selected depth profiles (Figures 2.4, 2.6, and 2.9) used for calculation of the iodine mass balance here are not impacted by oxygen deficiency, and therefore we do not expect lower than average [IO_3^-] that might otherwise impact mass balance calculations (Evans et al., 2020, Carpenter et al., 2014, Hardisty et al., 2020). Depth profiles of IO_3^- measured at 12 stations across the GP17-OCE transect show typical distribution concentrations (Chance et al., 2014, Tian et al., 1995, Cheng et al., 2024) and are generally found at about 400-450 nM concentration at depth. Profiles at lower latitudes show some decrease in [IO_3^-] at the surface, giving way for the higher [I^-] that is expected in euphotic waters at these latitudes as a result of reduction by bacteria and phytoplankton (i.e. *Synechococcus, Prochlorococcus*) that are prevalent there (Hepach et al., 2020, Chance et al., 2014).

For a comparison to and validation of our data, we compiled known Pacific sea surface IO_3^- and I^- data. Studies that measure iodine redox concentrations in areas of the Pacific that are known to be areas of large OMZs have been omitted from comparison with this data as iodine redox species show very specific profiles through these areas (low surface IO_3^- and high surface I^- through the most prolific sections of the OMZ) that differ significantly from oxygenated, open ocean environments (Evans et al., 2020). The specific OMZ impacting comparisons of Pacific data here is located in the Eastern Tropical North Pacific (ENTP), which stretches from the coast of Mexico out to the open ocean at about 20°N. At 152°W, waters are fully oxygenated and the OMZ is not affecting our iodine concentration measurements.

The concentrations of IO_3^- and I^- measured here generally overlap with previous studies across the Pacific Ocean (Figure 2.6). Iodine's specific trends in concentration across latitude are well-known, with I^- decreasing at high latitudes and increasing in productive low latitudes, and IO_3^- inversely trending with high concentrations at higher latitudes where upwelling brings IO_3^-–concentrated water to the surface and with low concentrations in low latitudes where bacteria and phytoplankton quickly reduce IO_3^- to I^- (Chance et al., 2014, Hepach et al., 2020, Schnur et al., 2024). Other studies have measured sections of the Pacific (Elderfield and Truesdale, 1980, Mctaggert et al., 1994, Nakayama et al., 1985, Tsunogai and Henmi 1971, among others) (Figure 2.4, blue circles), but none have measured these concentrations across such a full transect of the Pacific. Importantly, the compiled data show comparable results despite variable analytical techniques. Ours and previous studies use a variety of methods to measure concentrations of IO_3^- and I^-, the most common of which is spectrophotometry (Tsunogai and Henmi 1971, Jickells 1988) for IO_3^- and cathodic-strip voltammetry (Campos et al., 1997, Wong and Zhang 1992), ICP-MS (Hardisty et al., 2020, Hardisty et al., 2021, Schnur et al., 2024, Ştreangă et al., 2023), and IC methods (Jones et al., 2023, Hu et al., 2002) for measurement of I^-. With recent advances in ICP-MS methods (Hardisty et al., 2020, Hardisty et al., 2021), ICP-MS is becoming a very precise way to measure concentrations of I^- in seawater, where previously its low concentrations in seawater have sometimes lead it to be estimated by the difference of total iodine (TI) and IO_3^- in samples (Gong and Zhang 2013). The methods used in this study are spectrophotometric methods of measuring IO_3^-, using a modified method from Jickells et al., 1988, and column chromatography and ICP-MS methods (Hardisty et al., 2020, Hardisty et al., 2021) for the separation and measurement of I^- from surface seawater samples (section 2.3.2.1 and 2.3.2.2).

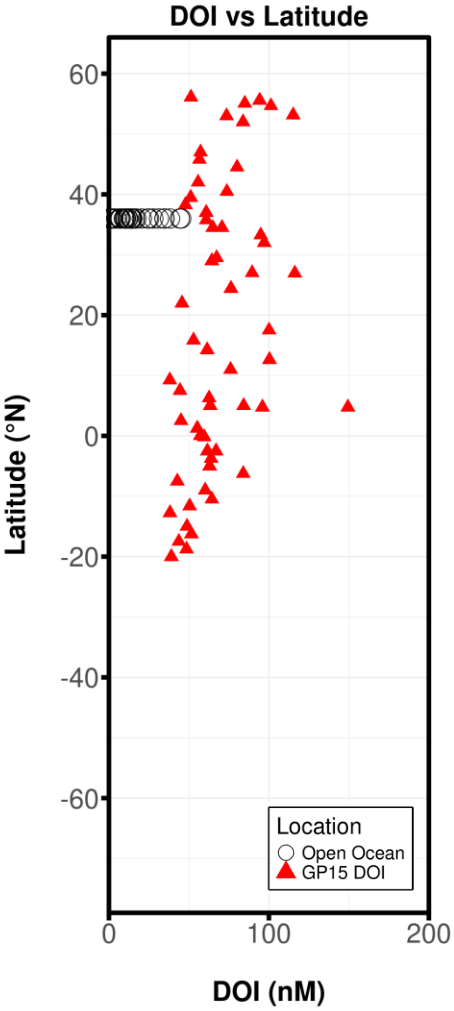

Figure 2.9 Measured GP15 DOI concentrations versus latitude in the Pacific Basin plotted with DOI data from Huang et al., 2005.

Dissolved Organic Iodine (DOI) is an iodine intermediate that is formed when elemental iodine (I_2) or HOI, another iodine intermediate, reacts with dissolved organic carbon (Hardisty et al., 2020, Luther 1995, Shetaya et al., 2012). Our measured DOI values from the North Pacific during GP15 (Figure 2.9) are the first meridional dissolved organic iodine transect measurements for the Pacific Ocean. Our transect DOI measurements show an active DOI cycle with some variation over latitude, and generally elevated values of between 37 and 150 nM through the transect. DOI is not a species of iodine that is typically measured, and previous reports suggest that it constitutes around 5% of iodine in the open ocean, although it can constitute up to 10-20% of the total iodine pool (Chance et al., 2020, Wong and Cheng 1998, Ştreangă et al., 2024). Figure 2.9 shows existing DOI data from the Pacific (black circles). Ştreangă et al., 2023, measured DOI in the North Pacific and showed that up to 8% of the total iodine pool in these locations could be ascribed to present DOI (specific concentration values not reported), and Huang et al., 2005 (Figure 2.9) measured the vertical distribution of dissolved nutrients in the North Pacific at 155°E. These measurements included measurements of DOI, which found little variation with depth.

2.5.2 Biological and External Drivers of iodine variations at the sea surface

The GP15 and GP17-OCE cruises transect waters from across many areas of changing biogeochemical and iodine redox concentration profiles. It is likely that a combination of the effects of biogeochemistry, ocean circulation and mixing, and "hotspots" of iodine redox transformations leads to the distribution of iodine that we see across these sea surface areas (Figure 2.4) and depth profiles of IO_3^- (Figure 2.6, Figure 2.7). For example, samples taken during the GP15 cruise in September 2018 were taken during boreal Autumn, when a phytoplankton bloom is known to occur at high latitudes due to deeper mixing of waters and nutrient upwelling that accompany this season (Martinez et al., 2011). Similarly, samples taken during the GP17-OCE cruise were taken during austral summer, again when large phytoplankton blooms are occurring north of 40°N and South of 40°S as upwelling brings nutrient-rich (i.e. nitrogen-rich) water from deeper depths (Figure 2.4, Deppeler and Davidson 2017). In addition to seasonality, trends in ecological zones, such as those defined by Alan Longhurst (2007), and general ocean currents can help us to understand broad variations in iodine concentrations throughout the Pacific Ocean (Figure 2.4). Together, the GP15 and GP17-OCE cruises cross 10 of the overall 56 defined ecological zones throughout the world ocean that, as they are meant to compare to terrestrial biomes, attempt to define the response of phytoplankton in the surface ocean to external forces

(Reygondau and Dunn 2018). We ultimately suggest that the combination of the following factors control IO_3^-/I^- abundance across latitude, with variable contributions from each at different locations described below: 1) external supply of elevated IO_3^- to the surface from vertical mixing; 2) IO_3^- reduction to I^- via phytoplankton in euphotic waters; and 3) I^- oxidation to IO_3^- in euphotic waters.

Over the latitudes traversed by the GP15 and GP17-OCE cruises (56°N to 67°S, moving from north to south), IO_3^- and I^- show specific trends in concentration over areas of varying temperature (controlling vertical mixing), ocean currents, and biogeochemical regimes (Figure 2.4). Importantly, these trends are relatively mirrored north and south of the equator. Specifically, a similar trend is seen for North and South of the North Pacific Polar Front (NPPF) (40°N) and South Subtropical Convergence (SSTC) (40°S), respectively, with relatively elevated IO_3^- and limited I^-; though I^- is lower north of the NPPF. The North Pacific Tropical Gyre (NPTG) and South Pacific Gyre (SPSG) are both marked by a relative trough in IO_3^- and corresponding I^- peak. Straddling the equator, the Pacific Equatorial Divergence (PEQD) and North Pacific Equatorial Countercurrent (PNEC) are marked by a relative peak in IO_3^- and decline in I^- as compared to the gyre regions (North Pacific Tropical Gyre (NPTG) and South Pacific Gyre (SPSG)) directly north and south of the equatorial biomes.

The relatively high IO_3^- and low I^- at the northern- and southern-most end of the combined GP15 and GP17-OCE latitudinal transect also correspond with high reported chlorophyll-a and temperature changes across the transect (Figure 2.4). Generally, where there is a larger amount of chlorophyll-a reported, a larger amount of IO_3^- is reported overall. This increase in IO_3^- also overlaps with colder surface waters. Together, the overlap of elevated IO_3^- with colder surface waters and higher chlorophyll contents is likely a result of a limited vertical temperature gradient enhancing vertical exchange of deep nutrient-rich waters to surface waters, which fuel phytoplankton growth but also supplies IO_3^--rich waters to the surface. Notably, this does not imply a lack of IO_3^- reduction via phytoplankton, just that this IO_3^- sink is balanced by the supply of IO_3^- from underlying waters. For measurements of $[IO_3^-]$ with depth from GP17-OCE specifically, the intense vertical mixing at high latitudes is apparent in depth profiles (Figure 2.6), where the concentration of IO_3^- is found to be extremely consistent from surface to deep starting around station 10 (~400 nM), where the high level of phytoplankton becomes apparent (Figure 2.1, Figure 2.4).

Importantly, though IO_3^- is elevated, we expect that phytoplankton-driven IO_3^- reduction has the potential to be widespread in these high latitude waters – at least during respective summer months – given the elevated nutrients and diverse phytoplankton communities. However, upwelling of IO_3^- rich deep waters could replace this reduced fraction of IO_3^- in the surface, and lead to the consistent depth profile that we see in these areas even with the influence of large areas of phytoplankton. For example, blooms are documented during the transects via chlorophyll-a and a large concentration of phytoplankton are active in higher latitudes (Figure 2.4). Polar zones are characterized by low biodiversity in general (Ibarbalz et al., 2019), although phytoplankton and small eukaryotes, such as *Micromonas* and *Synecococcus* are known to dominate the dissolved chlorophyll maximum (DCM) here (Giebel et al. 2021, Hollibaugh et al., 2007, Bachy et al., 2022).

While phytoplankton-driven IO_3^- reduction is likely occurring throughout the transect, it is most evident in the North and South Gyres, where I^- peaks in both hemispheres. This is likely explained by relative temperature stratification increasing the residence time of I^- in surface waters in these regions relative to others. This can be seen in Figures 2.6 and 2.7, where these zones mark a stark increase in surface temperature relative to higher latitudes. While IO_3^- is supplied via *in situ* oxidation and vertical mixing, phytoplankton across the transect reduce IO_3^- to increase concentrations of I^-. Lower $[IO_3^-]$ and elevated $[I^-]$ are thus expected to occur in stratified areas where phytoplankton-driven reduction of IO_3^- outpaces *in situ* and *ex situ* supplies of IO_3^-. The distribution of phytoplankton communities likely plays an additional role, as experiments demonstrate variable capacity for IO_3^- reduction between species (Hepach et al., 2020, Bluhm et al., 2010). A large, diverse array of bacteria, phytoplankton (diatoms), and cyanobacteria are active at mid latitudes, including *Synecococcus*, *Prochlorococcus*, *Alteromonadaceae* and *Rhodobacteraceae* (Wang et al., 2023, Flombaum et al., 2013, Balmonte et al., 2024, Hepach et al., 2020, Raes et al., 2018). *Synechococcus* is shown to produce I^- at low rates compared to diatoms, although both types of microorganisms were seen to remove IO_3^- and produce I^- in culture, with *Synechococcus* (a cyanobacteria) directly shown in unialgal culture to reduce IO_3^- (Hepach et al., 2020, Chance et al., 2007). Additionally, marine aerobic bacteria such as *Alteromonadaceae* and *Rhodobacteraceae* have been shown to reduce IO_3^- in oxygen-limited environments (Kine et al., 2024).

While gyres are relatively oligotrophic and low in chlorophyll compared to higher latitudes, the nutrient regime of the NPTG and SPSG zones still facilitate phytoplankton growth. The mixed layer depths (MLDs) found here vary seasonally, and deepen in winter, forming surface mode waters. These nutrient-rich waters are enriched in NO_3 and encourage large biomass production that is taxonomically diverse (Longhurst 2007). In subtropical areas, the taxa of the Dissolved Chlorophyll Maximum (DCM) resembles that of the mixed layer above it during times of high mixing, such as in spring, until the pylon line fully develops and the taxa separate across the DCM (Longhurst 2007). This large biomass production facilitates increased reduction of IO_3^- to I^-, leading to observed low concentrations of IO_3^- and a relative spike in I^- concentrations in the NPTG and SPSG (Figure 2.4).

Observed increases in IO_3^- and a countering slight decrease in I^- is seen in the equatorial PNEC and PEQD zones (Figure 2.4). This could be explained by increased upwelling of IO_3^--rich deep waters, facilitated by displacement as the trade winds push surface water north and south of the equator. Another possibility for IO_3^- increase oxidation of I^- to IO_3^- in areas of increased biological concentration and richness facilitated by these upwelled nutrients, even through productivity is generally lower (Pennington et al., 2006). Although oxidation of I^- to IO_3^- is known to be slow (Hardisty et al., 2021, Schnur et al., 2024), it has been shown that some amount of oxidation of I^- to IO_3^- is facilitated by nitrifying bacteria (i.e. *Nitrosomonas*) (Hughes et al., 2021), likely below the mixed layer (Moriyasu et al., 2023). It is unsurprising then that NO_3-rich Pacific equatorial waters with a high amount of biological richness including many species of nitrogen-fixing bacteria would show prevalent production of IO_3^- in these areas, leading to an overall measured increase in IO_3^- here.

2.5.3 Mass balance constraints on upwelling and vertical diffusion

To quantify the impacts of vertical mixing, cellular iodine incorporation, and oxidation-reduction reactions on iodine speciation, we performed an iodine mass balance for the southern Pacific Ocean using depth profile measurements of $[IO_3^-]$ and $[^7Be]$ from stations across the GP17-OCE transect. ^7Be is an ideal tracer for comparison to IO_3^-, since the vertical profile of ^7Be is a function of vertical mixing (Kadko and Olson 1996, Grenier et al., 2023, Schulz et a., 2023) and has an inverse depth distribution to $[IO_3^-]$ (Figure 2.2). ^7Be can be used to trace rates of vertical mixing because rainfall deposits ^7Be on the surface ocean, and a short half-life of ~53 days leads to an important deficit of ^7Be concentrations through the water column, allowing for calculation of upwelling of ^7Be-free waters at depth (Kadko and Johns, 2011, Moriyasu et al., 2023, Figure 2.3). As ^7Be is deposited on the sea surface, its short half-life means that as ^7Be starts to diffuse into the water column and deeper depths and it is simultaneously decaying without an additional supply. Therefore, ^{7}Be abundance decreases rapidly and is essentially absent at deeper depths. The stark gradient seen between ^{7}Be-rich surface waters and ^{7}Be-free deep waters can be used to track rates of upwelling as deeper ^{7}Be-free waters are brought to the surface and dilute the ^{7}Be-rich surface. This dilution is an important factor in understanding how waters mix via calculations of upwelling and vertical diffusion.

Oppositely, IO_3^- accumulates with depth in the water column, until iodine is almost completely found as IO_3^-, at around 450 nM in concentration (Elderfield and Truesdale 1980, Luther 2023). The increase in IO_3^- can be seen in Figure 2.6 for IO_3^- profiles measured from this transect. Upwelling rates calculated from dilution of ^{7}Be surface waters by ^{7}Be-free waters tells us the amount of IO_3^- that is being brought to the surface from these depths, and more heavily concentrates IO_3^- at the surface with the movement of these waters.

Our reported iodine oxidation rate for the area covered by the mass balance was calculated using Equation 2.1 from the y-intercept of the linear regression of values at all stations (Figure 2.8). The calculated average of 0.23 mmol m^{-2} day^{-1} for the South Pacific presented here fits well within the range published for studies at the Hawaii Ocean Time Series (HOT) off the coast of Oahu at Station Aloha (22°N, 158°W) in the North Pacific and Bermuda Atlantic Time Series (BATS) in the Sargasso Sea (31°N, 64°W) , both published by Campos et al. in 1996 (Table 2.5). This flux of IO_3^- into the system from oxidation is important for understanding formation of the oxidized species throughout the South Pacific. Although rates of oxidation of I^- are slow (previously reported between $5.3x10^{-4}$ – 18 nM/day) (Schnur et al., 2024, Hardisty et al., 2020, Campos et al., 1996, Newell et al., 2013, Hughes et al., 2021, Moriyasu et al., 2023), this calculated flux shows that at least some oxidation to IO_3^- is occurring throughout the basin. This formation rate, along with the rate of movement of IO_3^- throughout the basin by *ex situ* methods of water mass movement, is important for understanding the distribution of iodine redox species that we see across latitude in open ocean basins. Campos et al., 1996 calculated an IO_3^- production rate of 1.53 nM/day based on a seasonal mass balance in the Pacific Gyre, an important comparison for the mass balance described here.

Estimates of biological iodine assimilation via an iodine:carbon (I:C) ratio were calculated at a value of $1.2x10^{-2}$ based on the sum of vertical mixing fluxes versus calculated values of NCP. Previously reported values of I:C ratios show this to be high, as ratios of this kind are generally reported between 10^{-3} to10^{-5} in open ocean regions (Wadley et al., 2020, Chance et al., 2010, Elderfield & Truesdale, 1980, Jickells et al., 1988). Importantly, the wide scatter observed between stations for calculated values of F_{mix} and NCP and resulting high calculated slope at a low R^2 value could be due to difference in environmental factors across a large ocean basin for NCP, where values of production are based on factors such as amount of biological activity, concentration of nutrients and depth of the mixed layer, as well as environmental factors such as amount of light (Cottrell et al., 2006). Across a large transect such as GP17-OCE, these factors can change significantly, leading to a large difference in NCP reported between stations that are many kilometers apart. Similarly, the F_{mix} factor incorporates several measurements of IO_3^- and ^{7}Be over depth and across latitude at these different stations, which are incorporated in to calculations of w and K_z used to determine F_{mix}. Environmental factors also cause many changes in these measured concentrations over the wide scope of the GP17-OCE transect, and likely contribute to the scatter seen in the results shown in Figure 8. Improvements to the model could be made through grouping of stations across the transect in terms of more complimentary environmental factors, specific factors informing values of IO_3^- specifically based on known latitudinal trends (Chance et al., 2014), or, at a more robust level, as a station-level determination.

Previously calculated values are also calculated based on a "Redfield like" molar ratio to calculate IO_3^- reduction to I^- during NCP, which is measured directly from cells and not field observations (Lu et al., 2018, Wadley et al., 2020). The calculation done here is completed via field observations. It is possible that these values calculated here considering only IO_3^- concentrations over depth to calculate vertical mixing fluxes (F_{mix}) may be exaggerating the I:C ratio, as is suggested by Elderfield and Truesdale (1980). It would be beneficial to measure iodine redox concentrations at these stations near sediments or from phytoplankton from the water column in order to have a better understanding of the results of the calculations of the ratio presented here, in deoxygenated regions where IO_3^- production would be prohibited.

Importantly, the mass balance equation used here for calculation of these iodine oxidation rate and I:C ratios assumes three things that may lead to uncertainty in the results. The first assumption of the equation is that the system, i.e., the South Pacific Ocean, is at steady state, meaning that there is no net accumulation or loss of iodine. This assumption is overarching for a system of this size, as all inputs and influences of nutrients for the entire ocean, including terrestrial, aeolian, and deposition inputs and export from the system from ocean currents and remineralization are difficult to account for, and most likely do not lead to a system that is fully at steady state. Secondly, this steady state approach calculates a single oxidation rate and a single I:C ratio for the entire basin as a whole and does not calculate these individually for each station with measured [^{7}Be]. This is a limitation of the equation itself, and it must be understood that this generalization exists or a tolerance of the results discussed here. Lastly, the components of this equation lead to the assumption that the only three factors driving euphotic iodine distribution are: 1) vertical mixing, 2) NCP, and 3) I^- oxidation. As in any nutrient system, this process is likely more complicated and contains more factors than the three described, thus we limit ourselves with the understanding that only three factors are involved in the distribution of iodine through an entire ocean system.

Campos et al. (1996 and 1996) also calculated I^- formation values of 0.17 mmol m^{-2} day^{-1} for the Atlantic and 0.3 mmol m^{-2} day^{-1} for the South Pacific, something not calculated here, but worth mentioning as it relates to the amount of iodine found in oxygenated waters and could have an effect on the interpretation of values calculated in the mass balance.

Site	Iodate flux mmol m^{-2} day^{-1}	F_{red} (I^- formation) mmol m^{-2} day^{-1}	Ocean Basin	Citation
HOT	0.1-8.4	0.30	North Pacific	Campos et al., 1996; range for all stations
BATS	0.4-31.5	0.17	North Atlantic	Campos et al., 1996; range for all stations
GP17-OCE	0.23	-	South Pacific	This study; average of all stations

Table 2.5 Previous estimations of $r_{I:C}$ and F_{ox} in the Pacific Ocean as compared to findings for this study.

2.5.4 Implications

A mass balance of the Southern Pacific Ocean was completed to elucidate the role of mixing in [IO_3^-] contributions to the surface ocean. As it is known that I^- oxidation to IO_3^- is very slow (Hardisty et al., 2020, Schnur et al., 2024), it is likely that *ex situ* methods of water mass movement and mixing from "hotspots" of *in situ* I^- oxidation, such as areas of high primary productivity, pore water inputs, and OMZs may heavily influence the distribution of iodine redox species throughout ocean basins, and have a larger effect on measured iodine distribution in euphotic waters than has previously been known. Seasonal upwelling of high-latitude waters, like many measured in this study, likely contributes to surface water levels of IO_3^- as IO_3^--rich waters are brought to the surface from depth. Advection of these deeper waters, as is calculated in this study, also contributes to higher [IO_3^-] at the surface, as has been previously reported (Chance et al., 2020, Chance et al., 2010).

Knowledge on sources and distribution of iodine at the sea surface is key for a better understanding of surface ocean iodine's impact on O_3 destruction and to inform global climatological models more accurately (Macdonald et al., 2014, Ganzeveld et al., 2009, Helmig et al., 2012). Iodide in the surface ocean reacts with and destroys tropospheric ozone (O_3), releasing hypoiodous acid (HOI) and I_2 to the atmosphere (Carpenter et al., 2013, Hepach et al., 2020), which quickly photolyze to I atoms that react with O_3 to form IO (Carpenter et al., 2013). Iodine is eventually recycled back to ocean basins through rain and runoff. Deposition of O_3 to the sea surface is a significant O_3 sink and accounts for about one third of the total global O_3 dry deposition flux (600-1000 Tg O_3) per year, with an accompanying flux on the order of 10^{12} per year of iodine from the surface ocean to the atmosphere (Chance et al., 2014).

An understanding of IO_3^- formation and iodine distribution is also vital to understanding iodine to calcium (I/Ca) ratios that are present in carbonates, which have an important role in the paleoredox proxy for tracking ancient ocean oxygenation, notably during oceanic anoxic events (OAEs) (Lu et al., 2010). Our measurements of IO_3^- distribution throughout the Southern Pacific Ocean basin help to better understand the impact of these processes in this part of the world ocean, and inform on the impact that iodine has on paleoredox and atmospheric processes.

The effect of vertical mixing on IO_3^- profiles measured in this study as a result of calculations using concentrations and initial values of ^{7}Be and mixed layer depth is especially pronounced at southern stations at the highest latitudes of the GP17-OCE transect. In more northern stations, these profiles show a consistent lower concentration of IO_3^- up to the first 500 m, where [IO_3^-] then reaches ~400 nM concentration and is steady at this concentration through the remainder of the water column. However, at southern stations where vertical mixing is prominent and temperatures are generally higher, IO_3^--rich waters are brought to the surface with more consistency and concentrations of IO_3^- in the top 500 m of the water column are found to be ~400 nM and are very consistent with depth through the water column.

2.6: Conclusion

We are extending our understanding of IO_3^- flux to photic zones across the Southern Pacific and surface iodine redox species distribution across the Pacific Ocean at 152°W with the transect cruises GEOTRACES GP15 (North Pacific) and GP17-OCE (South Pacific). We have measured concentrations of I^- and IO_3^- across a latitudinal transect of the Pacific, from Alaska (53°N) to southern waters near Antarctica (67°S). The Pacific is under characterized in terms of our understanding of iodine within these waters, and these measurements are an important step for characterizing a large part of the ocean by means of trace element concentration measurements that are used in definitions such as the paleoredox proxy that aids in our understanding of ancient oxygen distribution. Our measurements show good correlation with past measurements of iodine in these waters, and bolster conclusions of rapid IO_3^- to I^- reduction in waters with high levels of primary productivity, and higher concentrations of IO_3^- at high latitudes where upwelling is intense.

Our measured concentration measurements of IO_3^- are used in conjunction with measurements of [^{7}Be], an element with contradictory trends in distribution through the water column with IO_3^-, that aided in calculation of rates of iodine uptake into carbon (I:C) and flux throughout the water column as part of a mass balance calculation for the Southern Pacific Ocean. Our calculated I:C ratio is higher than previously reported, while the calculated rate of flux of IO_3^- fits well with previous studies. It is important to understand that these calculations are generalized for the entire South Pacific basin, and are not site-specific. Site-specific calculations of these rates may give further insight into the importance of iodine into carbonate and ancient oxygen distribution as a more specific trend in ares of differing *ex situ* influences.

Vertical diffusion from subphotic waters may be a larger source of IO_3^- to surface waters than euphotic *in situ* oxidation. Calculation of positive upwelling and vertical diffusion along with known slow rates of I^- oxidation in open ocean waters show that these *ex situ* sources of movement of IO_3^- from deeper water where concentrations are stable and elevated are likely a larger contributor of [IO_3^-] in the surface ocean than *in situ* oxidation. An understanding of the movement of large water masses in the Pacific Ocean could lead to more definition of iodine redox species distribution via *ex situ* sources of water movement throughout the basin.

REFERENCES

Amachi, S., Kawaguchi, N., Muramatsu, Y., Tsuchiya, S., Watanabe, Y., Shinoyama, H., & Fujii, T. (2007). Dissimilatory iodate reduction by marine Pseudomonas sp. strain SCT. *Applied and Environmental Microbiology*, *73*(18). https://doi.org/10.1128/AEM.00241-07

Aoki, S., Takahashi, T., Yamazaki, K., Hirano, D., Ono, K., Kusahara, K., Tamura, T., & Williams, G. D. (2022). Warm surface waters increase Antarctic ice shelf melt and delay dense water formation. *Communications Earth and Environment*, *3*(1). https://doi.org/10.1038/s43247-022-00456-z

Balmonte, J. P., Giebel, H. A., Arnosti, C., Simon, M., & Wietz, M. (2024). Distinct bacterial succession and functional response to alginate in the South, Equatorial, and North Pacific Ocean. *Environmental Microbiology*, *26*(3). https://doi.org/10.1111/1462-2920.16594

Bluhm, K., Croot, P., Wuttig, K., & Lochte, K. (2010). Transformation of iodate to iodide in marine phytoplankton driven by cell senescence. *Aquatic Biology*. https://doi.org/10.3354/ab00284

Bock, N., van Wambeke, F., Dion, M., & Duhamel, S. (2018). Microbial community structure in the western tropical South Pacific. *Biogeosciences*, *15*(12). https://doi.org/10.5194/bg-15-3909-2018

Campbell, L., Liu, H., Nolla, H. A., & Vaulot, D. (1997). Annual variability of phytoplankton and bacteria in the subtropical North Pacific Ocean at Station ALOHA during the 1991-1994 ENSO event. *Deep-Sea Research Part I: Oceanographic Research Papers*, *44*(2). https://doi.org/10.1016/S0967-0637(96)00102-1

Campos, M. L. A. M. (1997). New approach to evaluating dissolved iodine speciation in natural waters using cathodic stripping voltammetry and a storage study for preserving iodine species. *Mar. Chem*. 57, 107–117. doi: 10.1016/S0304-4203(96)00093-X

Campos, M. L. A. M., Farrenkopf, A. M., Jickells, T. D., & Luther, G. W. (1996). A comparison of dissolved iodine cycling at the Bermuda Atlantic Time-series Station and Hawaii Ocean Time-series Station. *Deep Sea Research Part II: Topical Studies in Oceanography*. https://doi.org/10.1016/0967-0645(95)00100-x

Carpenter, L. J., Chance, R. J., Sherwen, T., Adams, T. J., Ball, S. M., Evans, M. J., Hepach, H., Hollis, L. D. J., Hughes, C., Jickells, T. D., Mahajan, A., Stevens, D. P., Tinel, L., & Wadley, M. R. (2021). Marine iodine emissions in a changing world. *Proceedings of the Royal Society A*, *477*(2247). https://doi.org/10.1098/RSPA.2020.0824

Carpenter, L. J., MacDonald, S. M., Shaw, M. D., Kumar, R., Saunders, R. W., Parthipan, R., Wilson, J., & Plane, J. M. C. (2013). Atmospheric iodine levels influenced by sea surface emissions of inorganic iodine. *Nature Geoscience*. https://doi.org/10.1038/ngeo1687

Chance, R., Baker, A. R., Carpenter, L., & Jickells, T. D. (2014). The distribution of iodide at the sea surface. In *Environmental Sciences: Processes and Impacts*. https://doi.org/10.1039/c4em00139g

Chance, R., Malin, G., Jickells, T., & Baker, A. R. (2007). Reduction of iodate to iodide by cold water diatom cultures. *Marine Chemistry*. https://doi.org/10.1016/j.marchem.2006.06.008

Chance, R., Tinel, L., Sarkar, A., Sinha, A. K., Mahajan, A. S., Chacko, R., Sabu, P., Roy, R., Jickells, T. D., Stevens, D. P., Wadley, M., & Carpenter, L. J. (2020). Surface Inorganic Iodine Speciation in the Indian and Southern Oceans From 12°N to 70°S. *Frontiers in Marine Science*, *7*, 621. https://doi.org/10.3389/FMARS.2020.00621/BIBTEX

Cheng, K., Ridgwell, A., and Hardisty, D. S.: Characterizing the marine iodine cycle and its relationship to ocean deoxygenation in an Earth system model, Biogeosciences, 21, 4927–4949, https://doi.org/10.5194/bg-21-4927-2024, 2024.

Cottrell, M. T., Malmstrom, R. R., Hill, V., Parker, A. E., & Kirchman, D. L. (2006). The metabolic balance between autotrophy and heterotrophy in the western Arctic Ocean. *Deep-Sea Research Part I: Oceanographic Research Papers*, *53*(11). https://doi.org/10.1016/j.dsr.2006.08.010

Councell, T. B., Landa, E. R., & Lovley, D. R. (1997). Microbial reduction of iodate. *Water, Air, and Soil Pollution*. https://doi.org/10.1023/A:1018370423790

Dafner, E., Mordasova, N., Arzhanova, N., Maslennikov, V., Mikhailovsky, Y., Naletova, I., Sapozhnikov, V., Selin, P., & Zubarevich, V. (2003). Major nutrients and dissolved oxygen as indicators of the frontal zones in the Atlantic sector of the Southern Ocean. *Journal of Geophysical Research: Oceans*, *108*(7). https://doi.org/10.1029/1999jc000288

Elderfield, H., & Truesdale, V. W. (1980). On the biophilic nature of iodine in seawater. *Earth and Planetary Science Letters*, *50*(1), 105–114. https://doi.org/10.1016/0012-821X(80)90122-3

Farrenkopf, A. M., & Luther, G. W. (2002). Iodine chemistry reflects productivity and denitrification in the Arabian Sea: Evidence for flux of dissolved species from sediments of western India into the OMZ. *Deep-Sea Research Part II: Topical Studies in Oceanography*, *49*(12), 2303–2318. https://doi.org/10.1016/S0967-0645(02)00038-3

Farrenkopf A. M., Dollhopf M. E., Chadhain S. N., Luther G. W., Nealson K. H. (1997). Reduction of iodate in seawater during Arabian Sea shipboard incubations and in laboratory cultures of the marine bacterium Shewanella putrefaciens strain MR-4. *Mar. Chem*. 57, 347–354. doi: 10.1016/S0304-4203(97)00039-X

Fox, P. M., Davis, J. A., & Luther, G. W. (2009). The kinetics of iodide oxidation by the manganese oxide mineral birnessite. *Geochimica et Cosmochimica Acta*, *73*(10), 2850–2861. https://doi.org/10.1016/J.GCA.2009.02.016

Gartman, A., & Findlay, A. J. (2020). Impacts of hydrothermal plume processes on oceanic metal cycles and transport. *Nature Geoscience 2020 13:6*, *13*(6), 396–402. https://doi.org/10.1038/s41561-020-0579-0

Gong, T., & Zhang, X. (2013). Determination of iodide, iodate and organo-iodine in waters with a new total organic iodine measurement approach. *Water Research*, *47*(17). https://doi.org/10.1016/j.watres.2013.08.039

Grenier, M., van Beek, P., Lerner, P., Sanial, V., Souhaut, M., Lagarde, M., Marchal, O., & Reyss, J. L. (2023). New insights on the 7Be cycle in the ocean. *Deep-Sea Research Part I: Oceanographic Research Papers*, *194*. https://doi.org/10.1016/j.dsr.2023.103967

Hardisty, D. S., Horner, T. J., Wankel, S. D., Blusztajn, J., & Nielsen, S. G. (2020). Experimental observations of marine iodide oxidation using a novel sparge-interface MC-ICP-MS technique. *Chemical Geology*. https://doi.org/10.1016/j.chemgeo.2019.119360

Hardisty, D. S., Lu, Z., Planavsky, N. J., Bekker, A., Philippot, P., Zhou, X., & Lyons, T. W. (2014). An iodine record of Paleoproterozoic surface ocean oxygenation. *Geology*, *42*(7), 619–622. https://doi.org/10.1130/G35439.1

Hepach, H., Hughes, C., Hogg, K., Collings, S., & Chance, R. (2020). Senescence as the main driver of iodide release from a diverse range of marine phytoplankton. *Biogeosciences*. https://doi.org/10.5194/bg-17-2453-2020

Hou X., Dahlgaard H., Nielsen S. P. (2001). Chemical speciation analysis of 129I in seawater and a preliminary investigation to use it as a tracer for geochemical cycle study of stable iodine. *Mar. Chem*. 74, 145–155. doi: 10.1016/S0304-4203(01)00010-X

Hu, W., Yang, P. J., Hasebe, K., Haddad, P. R., & Tanaka, K. (2002). Rapid and direct determination of iodide in seawater by electrostatic ion chromatography. *Journal of Chromatography A*, *956*(1–2). https://doi.org/10.1016/S0021-9673(01)01581-3

Huang, Z., Ito, K., Morita, I., Yokota, K., Fukushi, K., Timerbaev, A. R., Watanabe, S., & Hirokawa, T. (2005). Sensitive monitoring of iodine species in sea water using capillary electrophoresis: Vertical profiles of dissolved iodine in the Pacific Ocean. *Journal of Environmental Monitoring*. https://doi.org/10.1039/b501398d

Hughes C., Barton E., Hepach H., Chance R., Pickering M. D., Hogg K., et al. (2021). Oxidation of iodide to iodate by cultures of marine ammonia-oxidising bacteria. *Mar. Chem.* 234, 104000. doi: 10.1016/J.MARCHEM.2021.104000

Hung, C. C., Wong, G. T. F., & Dunstan, W. M. (2005). Iodate reduction activity in nitrate reductase extracts from marine phytoplankton. *Bulletin of Marine Science*, *76*(1).

Ibarbalz, F. M., Henry, N., Brandão, M. C., Martini, S., Busseni, G., Byrne, H., Coelho, L. P., Endo, H., Gasol, J. M., Gregory, A. C., Mahé, F., Rigonato, J., Royo-Llonch, M., Salazar, G., Sanz-Sáez, I., Scalco, E., Soviadan, D., Zayed, A. A., Zingone, A., … Zinger, L. (2019).

Global Trends in Marine Plankton Diversity across Kingdoms of Life. *Cell*, *179*(5). https://doi.org/10.1016/j.cell.2019.10.008

Janssen, D. J., Rickli, J., Quay, P. D., White, A. E., Nasemann, P., & Jaccard, S. L. (2020). Biological Control of Chromium Redox and Stable Isotope Composition in the Surface Ocean. *Global Biogeochemical Cycles*, *34*(1), e2019GB006397. https://doi.org/10.1029/2019GB006397

Jickells, T. D., Boyd, S. S., & Knap, A. H. (1988). Iodine cycling in the Sargasso Sea and the Bermuda inshore waters. *Marine Chemistry*. https://doi.org/10.1016/0304-4203(88)90006-0

Jones, M. R., Chance R., Dadic R., Hannula H. R., May R., Ward M., et al., (2023). Environmental iodine speciation quantification in seawater and snow using ion exchange chromatography and UV spectrophotometric detection. *Anal. Chimica Acta* 1239 (November 2022), 340700. DOI: 10.1016/j.aca.2022.340700

Kadko, D., & Olson, D. (1996). Beryllium-7 as a tracer of surface water subduction and mixed-layer history. Deep-Sea Research Part I: Oceanographic Research Papers. https://doi.org/10.1016/0967-0637(96)00011-8

Kadko, D., & Johns, W. (2011). Inferring upwelling rates in the equatorial Atlantic using 7Be measurements in the upper ocean. Deep-Sea Research Part I: Oceanographic Research Papers, 58(6), 647–657. https://doi.org/10.1016/J.DSR.2011.03.004

Kadko, D. (2017). Upwelling and primary production during the U.S. GEOTRACES East Pacific Zonal Transect. *Global Biogeochemical Cycles*. https://doi.org/10.1002/2016GB005554

Kadko, D., Aguilar-Islas, A., Buck, C. S., Fitzsimmons, J. N., Landing, W. M., Shiller, A., Till, C. P., Bruland, K. W., Boyle, E. A., & Anderson, R. F. (2020). Sources, fluxes and residence times of trace elements measured during the U.S. GEOTRACES East Pacific Zonal Transect. Marine Chemistry, 222, 103781. https://doi.org/10.1016/J.MARCHEM.2020.103781

Kine, Ken & Yamamura, Shigeki & Amachi, Seigo. (2024). Iodate reduction by marine aerobic bacteria. Frontiers in Microbiology. 15. 10.3389/fmicb.2024.1446596.

Kipp, L. E., Sanial, V., Henderson, P. B., van Beek, P., Reyss, J. L., Hammond, D. E., Moore, W. S., & Charette, M. A. (2018). Radium isotopes as tracers of hydrothermal inputs and neutrally buoyant plume dynamics in the deep ocean. *Marine Chemistry*, *201*, 51–65. https://doi.org/10.1016/J.MARCHEM.2017.06.011

Lu W., Ridgwell A., Thomas E., Hardisty D. S., Luo G., Algeo T. J., et al. (2018). Late inception of a resiliently oxygenated upper ocean. *Science*. 361, 174–177. doi: 10.1126/science.aar5372

Lu, Z., Jenkyns, H. C., & Rickaby, R. E. M. (2010). Iodine to calcium ratios in marine carbonate as a paleo-redox proxy during oceanic anoxic events. *Geology*. https://doi.org/10.1130/G31145.1

Luhar, A. K., Galbally, I. E., Woodhouse, M. T., & Thatcher, M. (2017). An improved parameterisation of ozone dry deposition to the ocean and its impact in a global climate-chemistry model. *Atmospheric Chemistry and Physics*. https://doi.org/10.5194/acp-17-3749-2017

Luther, G. W., Wu, J., & Cullen, J. B. (1995). *Redox Chemistry of Iodine in Seawater*. 135–155. https://doi.org/10.1021/BA-1995-0244.CH006

Luther, G. W. I. (2023). Review on the physical chemistry of iodine transformations in the oceans. *Frontiers in Marine Science*, *10*, 20. https://doi.org/10.3389/FMARS.2023.1085618

Martinez, E., Antoine, D., D'Ortenzio, F., & de Boyer Montégut, C. (2011). Phytoplankton spring and fall blooms in the North Atlantic in the 1980s and 2000s. *Journal of Geophysical Research: Oceans*, *116*(11). https://doi.org/10.1029/2010JC006836

Matek, A., Bosak, S., Šupraha, L., Neeley, A., Višić, H., Cetinić, I., & Ljubešić, Z. (2023). Phytoplankton diversity and chemotaxonomy in contrasting North Pacific ecosystems. *PeerJ*, *11*. https://doi.org/10.7717/peerj.14501

Moisan, T. A., Dunstan, W. M., Udomkit, A., & Wong, G. T. F. (1994). THE UPTAKE OF IODATE BY MARINE PHYTOPLANKTON. *Journal of Phycology*. https://doi.org/10.1111/j.0022-3646.1994.00580.x

Moriyasu, R., Bolster, K. M., Hardisty, D. S., Kadko, D. C., Stephens, M. P., & Moffett, J. W. (2023). Meridional Survey of the Central Pacific Reveals Iodide Accumulation in Equatorial Surface Waters and Benthic Sources in the Abyssal Plain. *Global Biogeochemical Cycles*, *37*(3). https://doi.org/10.1029/2021GB007300

Moriyasu, R., Evans, N., Bolster, K. M., Hardisty, D. S., & Moffett, J. W. (2020). The Distribution and Redox Speciation of Iodine in the Eastern Tropical North Pacific Ocean. *Global Biogeochemical Cycles*, *34*(2), e2019GB006302. https://doi.org/10.1029/2019GB006302

Newell S. E., Fawcett S. E., Ward B. B. (2013). Depth distribution of ammonia oxidation rates and ammonia-oxidizer community composition in the Sargasso Sea. *Limnology Oceanography* 58 (4), 1491–1500. doi: 10.4319/LO.2013.58.4.1491

Pennington, J. T., Mahoney, K. L., Kuwahara, V. S., Kolber, D. D., Calienes, R., & Chavez, F. P. (2006). Primary production in the eastern tropical Pacific: A review. *Progress in Oceanography*, *69*(2–4). https://doi.org/10.1016/j.pocean.2006.03.012

Raes, E. J., Bodrossy, L., van de Kamp, J., Bissett, A., Ostrowski, M., Brown, M. v., Sow, S. L. S., Sloyan, B., & Waite, A. M. (2018). Oceanographic boundaries constrain microbial diversity gradients in the south pacific ocean. *Proceedings of the National Academy of Sciences of the United States of America*, *115*(35). https://doi.org/10.1073/pnas.1719335115

Rafter, P. A., Sigman, D. M., Charles, C. D., Kaiser, J., & Haug, G. H. (2012). Subsurface tropical Pacific nitrogen isotopic composition of nitrate: Biogeochemical signals and their transport. *Global Biogeochemical Cycles*, *26*(1). https://doi.org/10.1029/2010GB003979

Reygondeau, G., & Dunn, D. (2019). Pelagic Biogeography. In *Encyclopedia of Ocean Sciences, Third Edition: Volume 1-5* (Vols. 1–5). https://doi.org/10.1016/B978-0-12-409548-9.11633-1

Roch, M., Brandt, P., & Schmidtko, S. (2023). Recent large-scale mixed layer and vertical stratification maxima changes. *Frontiers in Marine Science*, *10*. https://doi.org/10.3389/fmars.2023.1277316

Rudnicki, M. D., & Elderfield, H. (1992). Helium, radon and manganese at the TAG and Snakepit hydrothermal vent fields, 26° and 23°N, Mid-Atlantic Ridge. *Earth and Planetary Science Letters*, *113*(3), 307–321. https://doi.org/10.1016/0012-821X(92)90136-J

Shetaya, W. H., Young, S. D., Watts, M. J., Ander, E. L., & Bailey, E. H. (2012). Iodine dynamics in soils. *Geochimica et Cosmochimica Acta*, *77*. https://doi.org/10.1016/j.gca.2011.10.034

Schnur AA, Sutherland KM, Hansel CM and Hardisty DS (2024) Rates and pathways of iodine speciation transformations at the Bermuda Atlantic Time Series. Front. Mar. Sci. 10:1272870. doi: 10.3389/fmars.2023.1272870

Scholz, F., Hardisty, D. S., & Dale, A. W. (2024). Early Diagenetic Controls on Sedimentary Iodine Release and Iodine-To-Organic Carbon Ratios in the Paleo-Record. *Global Biogeochemical Cycles*, *38*(2). https://doi.org/10.1029/2023GB007919

Schulz, K., Kadko, D., Mohrholz, V., Stephens, M., & Fer, I. (2023). Winter Vertical Diffusion Rates in the Arctic Ocean, Estimated From 7Be Measurements and Dissipation Rate Profiles. *Journal of Geophysical Research: Oceans*, *128*(2). https://doi.org/10.1029/2022JC019197

Sherwen, T., Chance, R. J., Tinel, L., Ellis, D., Evans, M. J., & Carpenter, L. J. (2019). A machine-learning-based global sea-surface iodide distribution. *Earth System Science Data*. https://doi.org/10.5194/essd-11-1239-2019

Ştreangă, I. M., Repeta, D. J., Blusztajn, J. S., & Horner, T. J. (2023). Speciation and cycling of iodine in the subtropical North Pacific Ocean. *Frontiers in Marine Science*, *10*. https://doi.org/10.3389/fmars.2023.1272968

Talley, L. D., Pickard, G. L., Emery, W. J., & Swift, J. H. (2011). Descriptive physical oceanography: An introduction: Sixth edition. In *Descriptive Physical Oceanography: An Introduction: Sixth Edition*. https://doi.org/10.1016/C2009-0-24322-4

Tian, R. C., & Nicolas, E. (1995). Iodine speciation in the northwestern Mediterranean Sea, method and vertical profile. *Marine Chemistry*, *48*(2). https://doi.org/10.1016/0304-4203(94)00048-I

Tsunogai, S. (1971). Iodine in the deep water of the ocean. *Deep-Sea Research and Oceanographic Abstracts*. https://doi.org/10.1016/0011-7471(71)90065-9

Tsunogai, S., & Sase, T. (1969). Formation of iodide-iodine in the ocean. *Deep-Sea Research and Oceanographic Abstracts*. https://doi.org/10.1016/0011-7471(69)90037-0

van Oostende, M., Hieronymi, M., Krasemann, H., & Baschek, B. (2023). Global ocean colour trends in biogeochemical provinces. *Frontiers in Marine Science*, *10*. https://doi.org/10.3389/fmars.2023.1052166

Wadley, M. R., Stevens, D. P., Jickells, T. D., Hughes, C., Chance, R., Hepach, H., Tinel, L., & Carpenter, L. J. (2020). A Global Model for Iodine Speciation in the Upper Ocean. *Global Biogeochemical Cycles*, *34*(9), e2019GB006467. https://doi.org/10.1029/2019GB006467

Wang, Y., Lin, H., Huang, R., & Zhai, W. (2023). Exploring the plankton bacteria diversity and distribution patterns in the surface water of northwest pacific ocean by metagenomic methods. *Frontiers in Marine Science*, *10*. https://doi.org/10.3389/fmars.2023.1177401

Webb, P. (2017). Introduction to Oceanography. In *Roger Williams University*. https://rwu.pressbooks.pub/webboceanography/

Wong, G. T. F., & Cheng, X. H. (1998). Dissolved organic iodine in marine waters: Determination, occurrence and analytical implications. *Marine Chemistry*. https://doi.org/10.1016/S0304-4203(97)00078-9

Wong, G. T. F., & Zhang, L. S. (1992). Determination of total inorganic iodine in seawater by cathodic stripping square wave voltammetry. *Talanta*, *39*(4). https://doi.org/10.1016/0039-9140(92)80148-7

Zhou, X., Jenkyns, H. C., Lu, W., Hardisty, D. S., Owens, J. D., Lyons, T. W., & Lu, Z. (2017). Organically bound iodine as a bottom-water redox proxy: Preliminary validation and application. *Chemical Geology*, *457*. https://doi.org/10.1016/j.chemgeo.2017.03.016

CHAPTER 3: WATER MASS ANALYSIS OF THE 2022 GEOTRACES SOUTHERN PACFIC TRANSECT (GP17-OCE) AND IMPLICATIONS FOR TRACE ELEMENT DISTRIBUTION

3.1: Abstract

A fundamental focus of the GEOTRACES program is understanding the biogeochemical cycles and large-scale distribution of trace elements and their isotopes (TEIs) in the marine environment. TEIs can be impacted by and ultimately become tracers of combinations of physical, biological, and chemical processes. Importantly, deconvolving the influences of *in situ* biogeochemical processes on TEIs and their integrated implications for the cycling of oxygen, carbon, and nutrients, for example, requires a quantitative framework for tracking the formation and movement of major water masses in ocean basins. Here, we have completed an extended water mass analysis (eOMPA) of oxygenated Southern Pacific waters across both meridional (latitude range) and zonal transects (longitude range) using hydrographic ship data from the GEOTRACES GP17-OCE (2022) cruise from Papeete, Tahiti, to Punta Arenas, Chile. We have identified eight major water masses that are present along this transect; three surface water masses, one intermediate water mass, and four deep and bottom waters that constitute a majority of the water column through the study area. Two water masses – AAIW and PDW – are intersected separately twice across the transect, first in the northern section of the "latitudinal" transect, and second in the final portion of the "pseudo-north" transect near the coast of Chile, where the cruise transects the "main" AAIW forming region. We report that the deep water mass AABW is found north of the Pacific-Antarctic ridge, perhaps due to entrainment with LCDW and subduction from mixed surface waters south of the Subantarctic Front (SAF). Our use of a single non-density-dependent OMPA shows the importance of including generally omitted surface water masses for accurate water mass deconvolution of deeper waters. As a demonstration of the implications for water masses on TEI distribution, we have used the OMPA results to construct a predictive conservative mixing framework for iodine distribution across the transect and compared these values to measured iodine speciation from Chapter 2 of this dissertation. Although IO_3^- was not found in this case to be a sufficient tracer for water mass movement in the South Pacific, the results of this comparison can be used to provide a baseline for quantifying the integrated impacts of physical mixing and biogeochemical processes on TEI distribution in the South Pacific.

3.2: Introduction

GEOTRACES is an international cruise program that focuses on biogeochemical cycling and the movement of trace metals throughout the world's oceans. The purpose of the GEOTRACES GP17-OCE cruise is, specifically, to understand the cycling of "key elements" in the Southern Pacific Ocean basin, and, for the purpose of this study, to disseminate the role that physical mixing properties has on the distribution of iodine redox species in the Pacific Ocean as a result of water mass movement, and their contributions to areas of the Southern Pacific Ocean basin. Several previous South Pacific transect studies have included iodine as part of their parameters, including those done for the GEOTRACES GP15 cruise (North Pacific) (Moriyasu et al., 2023, Chapter 2 of this dissertation) and along the Eastern Tropical North Pacific (Moriyasu et al., 2020, Hardisty et al., 2021). These studies have shown that iodine is ubiquitous in the South Pacific and follows well-known trends of distribution (Chance et al., 2014). The GEOTRACES GP17-OCE cruise provided a unique opportunity to sample open ocean waters across the South Pacific basin over large biogeochemical gradients, through many areas of changing ocean currents, and across physical features such as the Pacific Antarctic ridge that form major boundaries for water mass movement (Figure 3.2). This cruise also crossed waters above known areas of hydrothermal plume influence, allowing for study of nutrients and trace elements and isotopes (TEIs) in variable waters. A unique feature of GP17-OCE is the inclusion of both a "latitudinal" (152^{o}W) and "longitudinal" (67^{o}S) section as part of one cruise, granting the opportunity to sample both open ocean waters and waters moving towards a coastal environment in one single cruise. Previous cruises have not had a similar range of this extent.

In order to fully understand the incorporation of nutrients and TEIs into the South Pacific basin, it is first imperative to understand the environment in which they are incorporated: the distinct water masses of the basin itself. By understanding the baseline properties of these water masses, we are able to denote changes from the baseline state of each mass and interpret from this the likely drivers of nutrient variability. Each identifiable body of water, or singular water mass, has a common formation history which has physical properties that are distinct from surrounding waters (Talley 2011). Physical qualities of these water masses, such as temperature and salinity that combine to determine the density of an individual water mass, are conservative flow tracers. Each water mass is assigned a water type "core", or endmember, composition that is considered the source or center of measured properties. As nutrients are semi-conservative, an extended

Optimum Multi-parameter Analysis (OMPA) using known remineralization ratios (Supplementary Table 3.3) is used here to account for nutrient deviation from source water mass properties (Evans et al., 2023, Lawrence et al., 2022).

OMPA relies on a set of linear mixing equations to solve for fractions of the defined endmember water types in a given sample (section 3.3.2) (Evans et al., 2020, Evans et al., 2023, Lawrence et al., 2022, Tomczak and Large 1989). These hydrographic properties must be conservative, and although the number of endmember water types that can be analyzed for a given sample in the OMPA is generally limited by the number of conservative properties available, the eOMPA tool used here allows for an overextension of this water mass to property ratio, allowing for elucidation for all water masses in the area without impediment. Because of the semi-conservative nature of nutrients in ocean water, the use of eOMPA is crucial for a good fit for South Pacific water masses (Lawrence et al., 2022, Evans et al., 2023). Known major influential water masses in the South Pacific include: Subtropical and Subantarctic Mode Waters (STMW/SAMW), Antarctic Intermediate Water (AAIW), Pacific Deep Water (PDW), Upper and Lower Circumpolar Deep Water (UCDW/LCDW), North Atlantic Deep Water (NADW), Antarctic Bottom Water (AABW), and Antarctic Surface Water (AASW), with smaller influences of other water masses such as Southern Equatorial Pacific Intermediate Water (SEqPIW) and 13C Water.

The Southern Pacific Ocean is known to be dominated by deep and bottom waters that are sourced from circumpolar and deep waters moving toward and around Antarctica (Figure 3.1) (Talley 2011, Orsi a et al., 1999). These water masses, including the Lower Circumpolar Deep Water (LCDW), Upper Circumpolar Deep Water (UCDW), and Antarctic Bottom Water (AABW) are formed after circumpolar water at high latitudes are upwelled to the surface during overturning circulation (UCDW and LCDW) and dense brine-rejected surface water sinks to the depths off the coast of Antarctica (AABW) (Yamazaki et a., 2024, Iudicone et al., 2008). These circumpolar water masses, once upwelled, mix with surface waters in the Antarctic, evolve, and subduct northward to lower latitudes where they influence the formation of intermediate and mode waters like Antarctic Intermediate Water (AAIW) and Subantarctic Mode Water (SAMW). The UCDW and LCDW have strong upwelling signals that can be seen through study of nutrients like silica and oxygen (Grasse et al., 2013, Grasse et al., 2020, Reyes-Malaya et al., 2021). Although defined separately here, UCDW, LCDW, and AABW have very similar properties that allow for a large amount of mixing between them, and make up most of the water column in the Southern Ocean (Talley 2011, Waltemathe et al., 2024).

Pacific Deep Water (PDW) is incorporated at a similar depth to LCDW in the water column but moves in from the north above the North Atlantic Deep Waters (NADW) that eventually form LCDW (Talley 2013). This cruise catches only a slight influence in the north from PDW, as its influence is waning by the time this water mass reaches the latitudes transected by GP17-OCE (Bostock et al., 2010).

The Antarctic Intermediate Water (AAIW) is the only intermediate water present along this transect, with a large zone of influence in the latitudinal transect and strong influence near the coast in the "main" AAIW forming region – the only true water mass forming region waters that the cruise transects (Bostock et al., 2013, Xia et al., 2022, Talley 2011). AAIW is found throughout the Pacific south of 15°N and is prolific in its influence across these waters (Bostock et al., 2013, Zeno et al., 2005).

The single true surface water mass that is encountered, the Antarctic Surface Water (AASW), is formed from very cold, very dense water off the ice shelves of Antarctica, and is subducted northward slightly to add influence to SAMW and AAIW after mixing with upwelled UCDW and LCDW (Xia et al., 2022, Bostock et al., 2013, Li et al., 2022). Two mode waters are present along the GP17-OCE cruise track – the Subantarctic Mode Water (SAMW) and the Southern Tropical Mode Water (STMW). These mode waters sit just above AAIW in the water column and are formed as a result of heavy winter mixing in lower latitudes (Bushinsky and Cerovecki 2023, Hartin et al., 2011, Roemmich and Corneille 1991). These waters are only found in the most northern part of the latitudinal transect of GP17-OCE, and do not have influence with other water masses or subduct farther into the water column.

Using hydrographic ODF data from GEOTRACES GP17-OCE, we completed an extended python Optimum Multiparameter Analysis (eOMPA) (Evans et al., 2023, Lawrence et al., et al., 2022) of Southern Pacific water masses to diagnose the relative contribution of these defined water masses along the transect. Eight water masses that contribute to waters in these areas are defined here (Table 3.1). In this study, the influence of these eight water masses across the transect of GP17-OCE will be explored and elucidated, and the contributions to conservative and non-conservative factors of conservative temperature, absolute salinity, oxygen, nitrate, nitrite, silica, and phosphate will be determined.

Water Mass	Abbreviation
Antarctic Intermediate Water	AAIW
Subantarctic Mode Water	SAMW
Antarctic Surface Water	AASW
Antarctic Bottom Water	AABW
Pacific Deep Water	PDW
Lower Circumpolar Deep Water	LCDW
Upper Circumpolar Deep Water	UCDW
Southern Tropical Mode Water	STMW

Table 3.1 Water masses encountered by the GP17-OCE transect at 152°W.

3.3: Methods

3.3.1 Sample collection

Hydrographic data was collected shipboard during the entirety of the GEOTRACES GP17-OCE transect from December 2022 – January 2023, encompassing 59 stations within the Southern Pacific basin. 32 stations of the total 59 were sampled over a depth profile, at depths reaching between 3 and 5738.1 m, with bottom depth varying for each station (Supplementary Table 3.1). Water types are characterized by a unique set of hydrographic properties (Jenkins et al., 2015). The variables used from these measurements for the water mass analysis include conservative temperature (°C), absolute salinity (g/kg), and concentrations of phosphate (µmol/kg), nitrate (µmol/kg), silica (µmol/kg), and oxygen (µmol/kg). Bottle ODF (Ocean Data Facility) hydrographic data used for this study from the GP17-OCE cruise is available at https://www.bco-dmo.org/dataset/933861.

The conventional ODF rosette for collection of non-contamination-prone TEI's were used with *in-situ* McLane pumps for collection of large volumes of water, including particulate TEI's (Twining et al., 2023a). Samples were filtered through nested 0.8 and 0.45 um Akropak filter capsules from a SIO STS 36-place yellow rosette holding Bullister style Niskin bottles (absolute volume 10.6 L). Filters were reused for similar casts and refrigerated between uses. Tubing was rinsed with

18 MΩ-cm water and reused for each cast. 36 filters were split into three sections – surface, intermedia, and deep – for use with similar waters between casts. Nutrients were sampled from every sample bottle by drawing samples into 30 ml polypropylene screw-caped centrifuge tubes that were cleaned with 10% HCl and analyzing within 2-16 hours after sample collection, after samples reached room temperature. Nutrient analysis for phosphate, silicate, nitrate used here for

OMPA analysis were performed on a Seal Analytical continuous-flow Auto Analyzer 3 (AA3) as described in the GP17-OCE ODF report. Analyses of dissolved oxygen was performed with an SIO/ODF designed automated oxygen titration using photometric end-point detection based on the absorption of 365 nm UV light (Twining et al., 2023b). The temperature, conductivity, dissolved oxygen, pumps, and exhaust tubing were mounted to the bottom of the CTD cage. CTD data was examined at the completion of each deployment for calibration shifts (Twining et al., 2023b).

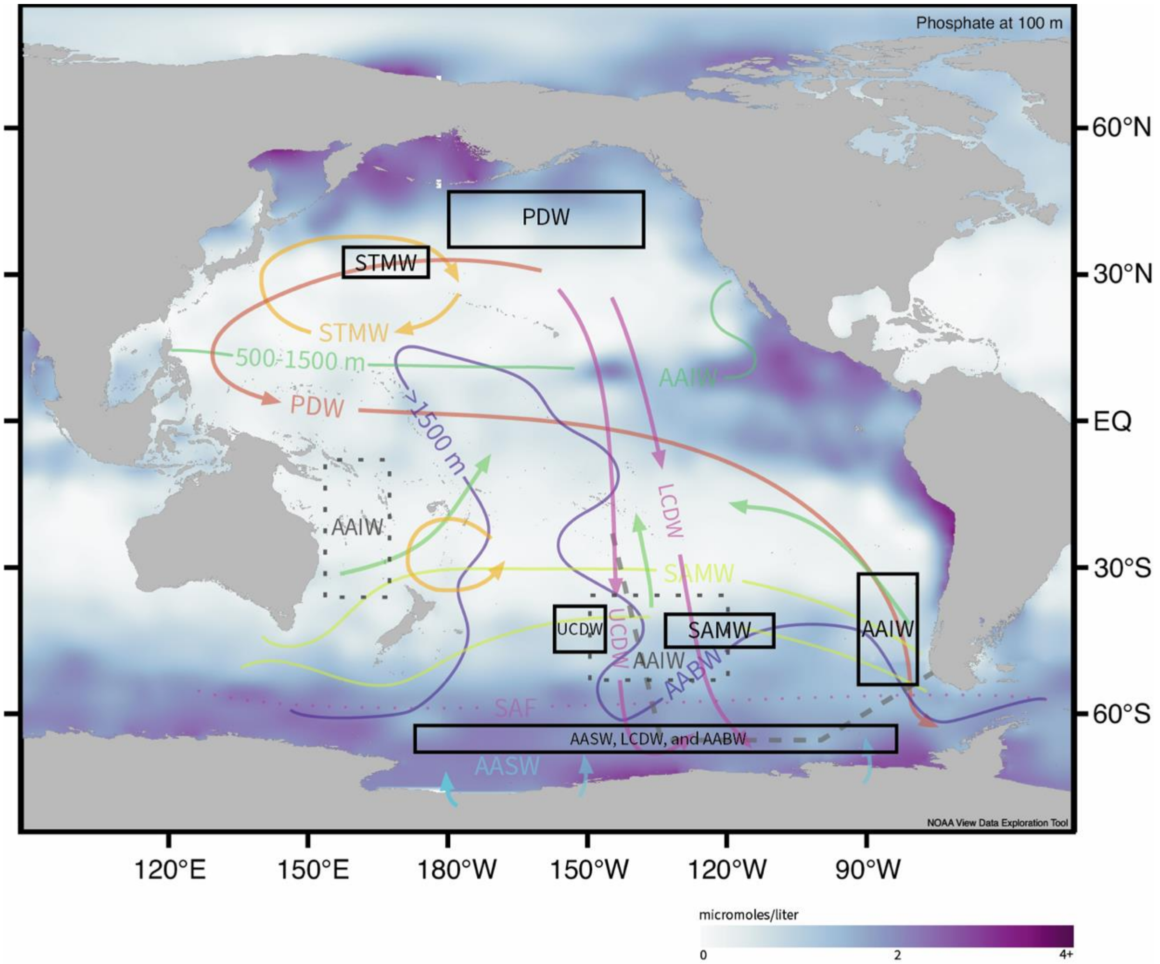

Figure 3.1 Interpretation of ranges and directional influences of eight water masses of the South Pacific (labeled colored lines) that intersect hydrographic data taken by GEOTRACES GP17-OCE transect (dark gray dashed line). Lines overlayed on phosphate concentration of the Paciifc at 100 m depth. Arrows depict movement of indivual water masses as influenced by major oceanic currents. Forming regions indicated by black squares for each water mass. Additional Pacific AAIW forming regions not used in this study outlined in gray dashed squares. (Oka et al., 2003, Peters et al., 2018, Lawrence et al., 2022, Meijer et al., 2019, Bostock et al., 2013).

Compiled CTD and ODF nutrient bottle data was used as a basis for water mass data in pyOMPA as the representation of water masses and water properties throughout the Southern Pacific Ocean along 152°W and 67°S. Individual water mass core properties were discerned as described above, and nutrients across the transect were plotted for visualization (Figure 3.3), as changes with density can somewhat visualize water mass contributions through semi-conservative nutrients. This phenomenon is especially apparent in definitions of oxygen and silica across the transect (Figure 3.3).

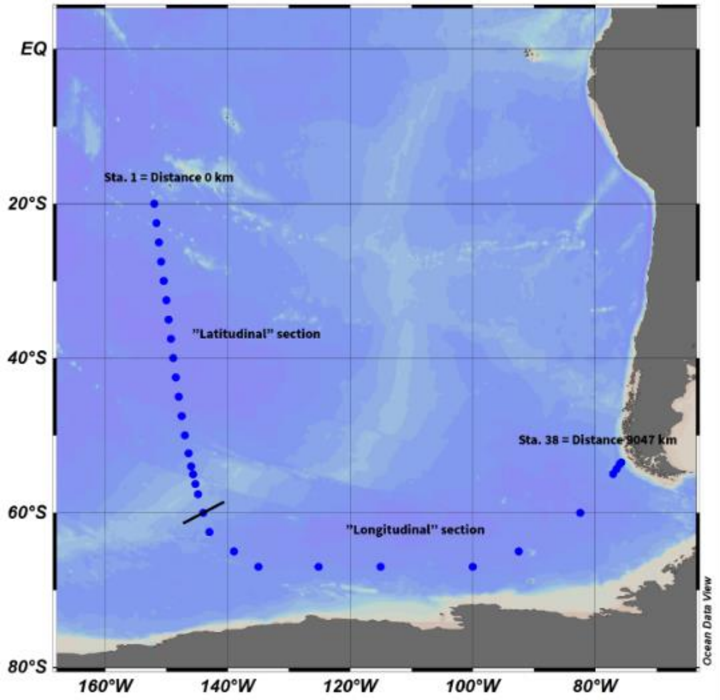

Figure 3.2 Transect map of GP17-OCE showing individual stations (blue dots). Data from all stations along the transect were used for differentiation of water masses. Line through Station 26 indicates "cut" between latitudinal and longitudinal sections for visualization.

Spiciness (θ) (used in characterization of oxygen-poor waters), potential density (σ), and potential vorticity (water rotation) are optional parameters of OMPA that were not used in this study (Evans et al., 2020. Other elemental parameters not used here have also been examined in past studies to aid in water mass deconvolution. Gallium has been explored for the potential of Arctic source water deconvolution by Whitmore et al., 2020, who found that their 1-D advection-diffusion model using Ga showed greater mixing between Pacific and Atlantic waters than previously expected in Arctic waters from past use of mixed nutrients at Redfield ratio. Zhang et al., 2018 has used four heavy Rare Earth Elements (HREEs), along with temperature and salinity for a water mass analysis of the East China Sea, showing that HREEs are conservative tracers that can be used in water mass deconvolution. Zheng et al., 2016 used a similar technique, using the dissolved Rare Earth Elements (REEs) Nd and Yb to investigate deeper waters (UCDW, UNADW, LNADW, and AABW) across an East-West section of the tropical South Atlantic, and yielding both non-conservative concentrations of the REEs and PO_4 and the water mass fractions of the deep waters studied.

The hydrographic data from GP17-OCE was filtered for depth values of <250 m, defined here as the "surface", as characterization of surface waters in OMPA is notoriously difficult. Generally, if characterized, surface water is split into a separate water mass analysis so that consistent deep waters may be analyzed separately (Llanillo, et al., 2013, Peters et a., 2018, Silva et al., 2009). Mixing from air-sea interactions at the surface and active nutrients cycling does not allow for the precise deconvolution of surface water mass contributions. It was found, however, that although inclusion of their full endmember spaces (up to 0 m) was counteractive to a well-founded analysis, inclusion of the surface and near-surface water masses themselves (STMW and AASW) and their endmember definitions was extremely important for correct characterization of intermediate and upwelling water masses both at low and high latitudes in this analysis.

3.3.2 Overview on water mass definitions

Each of the water masses studied here have been defined in previous work (Table 3.2, Figure 3.8), which we use as a starting place before refining to minimize residuals and best fit with our data from the GP17 transect. Below we overview this previous work informing our initial endmember definitions.

Southern Tropical Mode Water (STMW) is the surface most water mass measured in the northern section of the GP17-OCE transect. Like SAMW, it is formed from the subduction of winter mixed layers (Talley 2011, Rainville et al., 2007) and is centered at a potential density of 25.2 kg/m^3. The SMTW present in the South Pacific (SPSTMW) is the weakest of the global STMW's (Talley 2011, Roemmich and Corneille 1992). We define STMW in the north of the GP17-OCE transect at a slightly higher density of 25.12 kg/m^3 where it reaches a depth of about 500 m. STMW's influence wanes quickly across the latitudinal transect towards the influence of deeper waters at high latitudes.

Subantarctic Mode Water (SAMW) occurs north of the Subantarctic Front (SAF) and is formed from thick winter mixed layers with low vorticity, or rate of fluid rotation (Hanawa and Talley 2001). In the South Pacific, these waters can reach over 300 m in depth and either move eastward or are subducted northward during summer (Talley 2011, Sanders et al., 2023). SAMW is known to have a high oxygen content and supplies surface water to the subtropical pycnocline when subducted (Talley 2011). SAMW is defined here between ~300 and 800 m and a density of 26.63 kg/m^3 and is depleted quickly by the influence of AAIW.

Surface waters south of the SAF are defined as the Antarctic Surface Water (AASW), the coldest (-1.9-1^{o}C), freshest, and most dense of all the water masses defined by this analysis. Ice melt in summer contributes to freshwater input to these waters off the coast of Antarctica (Talley 2011, Jia et al., 2022). These water masses are only about 100-250 m thick. Because of the large input of fresh water and low change in temperature, the AASW is heavily influenced by salinity changes (Talley 2011). Recent accelerated ice melt from global ocean heating has had an effect on the ventilation of deeper waters (i.e. AABW) and increased the size of intermediate and mode waters (SAMW and AAIW). Eckman transport carries AASW northward across the SAF, where it is subducted and aids information of SAMW and AAIW (Talley 2011, Hartin et al., 2011, Lie et al., 2023, Akon et al., 2022).

One formation region for the only intermediate water sampled, the Antarctic Intermediate Water (AAIW), is crossed near the coast of Chile, measured in stations 35-37. AAIW formed here near the Drake Passage, termed “main” AAIW (Talley 2011, Bostock et al., 2013) is subducted beneath the Sub-Antarctic Front (SAF) near the coast of Chile and flows north and west out to the open Pacific Ocean, then being present throughout almost all latitudes and north to about 15^{o}N (Peters et al., 2018, Talley 2011, Hartin et al., 2011). The only water mass defined in this study with a lower salinity than AAIW is the AASW. AAIW across the GP17-OCE transect is defined as being completely composed of main AAIW water, with a density of 26.98 kg/m^3.

Circumpolar deep water (CDW) extends from northern latitudes below the AASW south of the SAF and below the AAIW north of the SAF (Talley 2011). CDW is divided here for definition of two separate water masses, the Upper Circumpolar Deep Water (UCDW) and the Lower Circumpolar Deep Water (LCDW). UCDW is formed from evolved PDW moving in from the north above North Atlantic Deep Water (NADW), and upsells to the surface ocean at high latitudes. There, UCDW mixes with surface waters (AASW) before subducting northward to aid in the formation for SAMW and AAIW. LCDW is formed from the deeper NADW as it evolves through the deep waters of the Pacific, also upwelling at high latitudes but subducting quickly once there as part of AABW formation. Talley (2011) defined UCDW as an oxygen minimum layer, while LCDW is known as a salinity maximum layer (Yamazaki et al., 2024). UCDW also includes a temperature maximum layer just below the AASW, and a high nutrient content (Talley 2011).

LCDW is defined as the bottom water for most of the world ocean outside of the Southern Ocean, where Antarctic Bottom Water (AABW) is found and defined separately. UCDW and LCDW's upwelling southward to high latitudes creates deep circulation in the South Pacific (Waltemathe et al., 2024). These water masses are defined from their upwelling regions in the South Pacific, far from less evolved waters that may still contain PDW and NADW remnants. They are defined with low oxygen values and densities of 27.52 kg/m^3 (UCDW) and 27.84 kg/m^3 (LCDW).

Pacific Deep Water (PDW) is also known for relatively low oxygen stemming from consumption of oxygen by microorganisms and decreased mixing in deeper waters (Webb 2023). PDW moves into the GP17-OCE transect area from the north above NADW (Talley 2011, Fuhr et al., 2021). This deep water mass is found in the northern section of GP17-OCE's latitudinal transect, and it appears to visually bifurcate the LCDW as they come together at similar depths in the waters around 40ºS (Figure 3.5). PDW is defined by low oxygen values close to those found in UCDW and a middling density of 27.68 kg/m^3 that leaves it similar in property to what is defined as CDW, defined above.

Antarctic Bottom Water (AABW) that is present in the South Pacific is formed in the Weddell Sea from sea ice formation and cooling of surface waters creating very dense water that sinks to deep depths (Talley 2011). AABW sits below the CDW in the Southern Ocean below the SAF and is generally restricted in range to high latitude waters by the Pacific-Antarctic ridge (Talley 2011, Zhou et al., 2023). Some mixing with LCDW may allow these very dense waters to be entrained northward into the South Pacific north of this ridge (Baker et al., 2023), and in fact, we document this in some capacity with the results of this analysis. AABW is the densest water mass defined in this study, at a density of 27.92 kg/m^3. This water is defined as it is formed in the Antarctic from subduction of very dense AASW that has been transformed from sea ice formation and rapid cooling of surface waters, as well as mixing with dense, upwelled LCDW.

Water Mass	**CT (◦C)**	**SA (g/kg)**	**Phosphate (μmol/kg)**	**Nitrate (μmol/kg)**	**Silica (μmol/kg)**	**Oxygen (μmol/kg)**	**Potential Density (kg/m^3)**	**Study**
AAIW	5.53	34.25	1.75	25.3	13	250	27.01	Peters et al., 2018
AAIW	6.03	34.7	3.48			4.8		Evans et al., 2020
AAIW	4-8	34.2-34.35		14-30	1-32	200-300	27.1	Bostock et al., 2013
AAIW	3.2-7	34.5-34.36					27.2-27.35	Vol. 181 Initial Reports ODP Proceedings
AAIW	3.5-10	34.3-34.5	1.25-2.25	20-35	5-80	200-250	27.1	Bostock et al., 2010
AAIW	4-6	34.1-34.5					27.05-27.15	Talley Chapter 10
AAIW	3	34	1.98	28.5	24.6	238.2		Reyes-Macaya et al., 2021
AAIW	5.04	34.39	1.67	23.99	11.51	272.31		Lawrence et al., 2022
AAIW	4.47	34.40	1.99	28.54	20.43	231.45		Lawrence et al., 2022
SAMW	7.4-9	34.53-34.61		28.6-32.4			26.8-27.1	Granger et al., 2018
SAMW	6-10	34-34.2					26.8-27.2	Vol. 181 Initial Reports ODP Proceedings
SAMW	8-9							Talley Chapter 13
SAMW	11	34	1.07	13.7	2.17	268.2		Reyes-Macaya et al., 2021
SAMW	4-15	34.2-35.2					26.6-27.1	Li et al., 2021
SAMW			1,7	25.0	10.7	255		Holte et al., 2013
SAMW			2.0	29.1	21.7	226		Holte et al., 2013
AABW	-0.9-0	34.53-34.67					>28.27	Talley Chapter 13
AABW	0.01	34.7	2.29	33.1	144	216	27.88	Peters et al., 2018
AABW	0.07	34.87	2.26	32.46	128.23	216.23		Lawrence et al., 2022
PDW	1.1-1.2	34.68-34.69						Talley Chapter 10
PDW	1.82	34.67	2.76	38.42	157.3	105.2	45.87	Reyes-Macaya et al., 2021
PDW	1.44	34.67	2.57	38.6	166	116	27.77	Peters et al., 2018
PDW	3.74	34.43	3.16	43.87	117.45	11.38		Lawrence et al., 2022
PDW	2.16	34.71	3.15	44.57	167.51	23.94		Lawrence et al., 2022
PDW	1.20	34.87	2.59	37.10	171.60	136.80		Lawrence et al., 2022
LCDW	0.55-0.9	<34.71					45.93-46	Vol. 181 Initial Reports ODP Proceedings
LCDW	1.3-1.8	34.8-34.9					27.8	Talley Chapter 13

Table 3.2 Comparisons of water mass endmembers from previous water mass literature and OMPA studies.

Table 3.2 (cont'd)

Water Mass	CT (◦C)	SA (g/kg)	Phosphate (µmol/kg)	Nitrate (µmol/kg)	Silica (µmol/kg)	Oxygen (µmol/kg)	Potential Density (kg/m^3)	Study
LCDW	1.67	34.73	2.2	31.9	92	190	27.79	Peters et al., 2018
LCDW	1.55	34.90	2.18	31.50	93.37	190.11		Lawrence et al., 2022
LCDW	0.77	34.86	2.26	32.43	119.83	199.11		Lawrence et al., 2022
UCDW	1.6-1.8	34.67-34.71					36.5-37	Vol. 181 Initial Reports ODP Proceedings
UCDW	1.5-2.5					<180	27.6	Talley Chapter 13
UCDW	2.44	34.57	2.4	34.5	77	168	27.59	Peters et al., 2018
UCDW	1.42	34.87	2.67			118		Evans et al., 2020
UCDW	2.50	34.73	2.39	34.11	83.32	168.79		Lawrence et al., 2022
AASW	-1-4	33-34.5						Talley Chapter 13
AASW	-1.235-1.219	34.375-34.631		24.7-33.1	32.2-77.2	212.9-300.3	27.748-27.842	Foppert et al., 2024
AASW			<2.4					Broecker et al., 1998
STMW	16-19						25.2	Talley Chapter 10
STMW	16-18						25.5	Talley Chapter 5
STMW	13-20							Vol. 181 Initial Reports ODP Proceedings
STMW	20.8	35.52	0.46	0.74	2.23	240.65		Reyes-Macaya et al., 2021

3.3.2 pyOMPA

We use here an extended pyOMPA package updated by Shrikumar and Casciotti (2022) from the Tomczak and Large (1989) original MATLAB OMPA, and used by Evans et al., 2023 for their investigation of nitrite re-oxidation across the Eastern Tropical North Pacific (ETNP) (https://pypi.org/project/pyompa/). This package includes hydrographic data from TEOS-10 (https://pypi.org/project/gsw/), updating oceanographic standards from those used previously. Extended OMPA (eOMPA) has the strict convenience of allowing for a larger number of water mass definitions to be defined than parameters given in one analysis, a disadvantage found in past OMPA analyses.

"Classic" OMPA views the measured properties of a water sample as a mixture of several end-members and assumes that these values are conserved by mixing (Shrikumar et al., 2022).

Where endmembers are perfectly explained, the sum of the value of a property endmember in any given sample multiplied by the fraction of the endmember in the sample should equal the value of the property in the sample. Where endmembers are not perfectly defined, a residual may be needed to apply the definition correctly (Equation 3.1), resulting in the following equation for each individual water mass, where e is the property p for any endmember, x is the estimated fraction of that end-member in a sample j, s the value of the property p in the sample j, and e is the residual needed to perfectly explain sample properties (Shrikumar et al., 2022):

$$\sum_i e_p^i x_j^i = s_p^j + e_p^j \quad \textit{Equation 3.1}$$

A least-squares optimization method is used to solve for x above, with an equation for each parameter. Water types must be a non-negative value and should sum to one.

Residuals provide an estimate of the prevision of the water mass budget and help to explain non-perfect endmember definitions of the water masses delineated in this study. Residuals are calculated based on uncertainty in endmember properties and uncertainty in the properties of the water samples themselves (Shrikumar et al., 2022) and scaled by the specified weights for each parameter as measured. In previous MATLAB OMPA studies, residuals were calculated in terms of mean-normalized parameter values, which meant that the OMPA solution was affected by mean normalization and it could be unclear which specific parameter might be forcing the mean (Shrikumar et al., 2022). pyOMPA does not have this constraint and allows for visualization of residuals of individual parameters so that each can be considered separately.

In the eOMPA analysis used here, semi-conservative properties such as nitrate, phosphate, silicate, and oxygen are more organically recognized as not fully conserved by mixing, unlike in the "classic" OMPA method described above, and it is assumed that remineralization, or an exchange of nutrients with oxygen in a fixed ratio (Shrikumar et al., 2022) is occurring (Figure 3.4). This adds a term to the equation shown above, where r is the exchange ratio of a parameter and Δ represents the amount of that property that is remineralized in the sample:

$$\left(\sum_i e_p^i x_j^i\right) + r_{NO3}^p delta_j^{NO3} = s_p^j + e_p^j \qquad \textit{Equation 3.2}$$

Parameters that are unaffected by remineralization (i.e. temperature, salinity), will have r simply equal 0 in Equation 3.2 above. Each parameter is used in the OMPA in an equation like Equation 3.2, with a final mass conservation variable forcing the system to sum to one (Karstensen and Tomczak 1998). More water masses can be considered in an extended OMPA than in the "classic" model by adding these semi-conservative parameters and solving the equations without assumptions (Liu and Tanhua 2021).

pyOMPA itself differs from the original MATLAB OMPA in four ways (Shrikumar et al., 2022). 1) mass conservation residuals are forced to zero, 2) the model can support both remineralization and assimilation of semi-conservative factors, 3) remineralization ratios are flexible and not fixed to the Redfield ratio, and 4) ambiguity is allowed in the solution to allow for the definition of more water masses than the number of parameters in a single OMPA. These improvements allow a powerful yet flexible definition of water masses in the research area where there are known to be more water masses present than variables used. Previous studies, even those using pyOMPA, have previously used two to three depth-divided analyses (i.e a surface, thermocline, and deep section with few water masses to accommodate restrictions based on number of factors) (Peters et al., 2018, Evans et al., 2020, Lawrence et al., 2023). Here, we present a single OMPA for all depths across the entire South Pacific that allows for definition of the system as a whole with a single endmember defined for each water mass and its variable.

3.3.3 pyOMPA weighting

Weighting is used to understand how variables change together through a variance-covariant matrix (ω) through two components, 1) measurement uncertainty, and 2) possible error. Differences in the measurement of the tracer variables makes weighting necessary to provide an approximately correct weighting of the tracers relative to each other. The weightings used in this study (Table 3.3) are the same as those used in Evans et al., 2023, for their study of nitrite re-oxidation across the Eastern Tropical North Pacific (ETNP), using the same pyOMPA package in a similar section of the same Ocean Basin. Comparison of these weightings with previous analyses (Supplementary Table 3.2) shows consistently higher values – indicating higher importance – placed on C_T and S_A, with weightings between 1 and 7 typical for other nutrients used for water mass definitions. Values for ranges of aerobic remineralization were chosen based on the Redfield ratio and previous studies (Supplementary Table 3.3) for each nutrient as it compares to phosphate (value of 1), the most conservative of the nutrients used for the definitions. Anaerobic

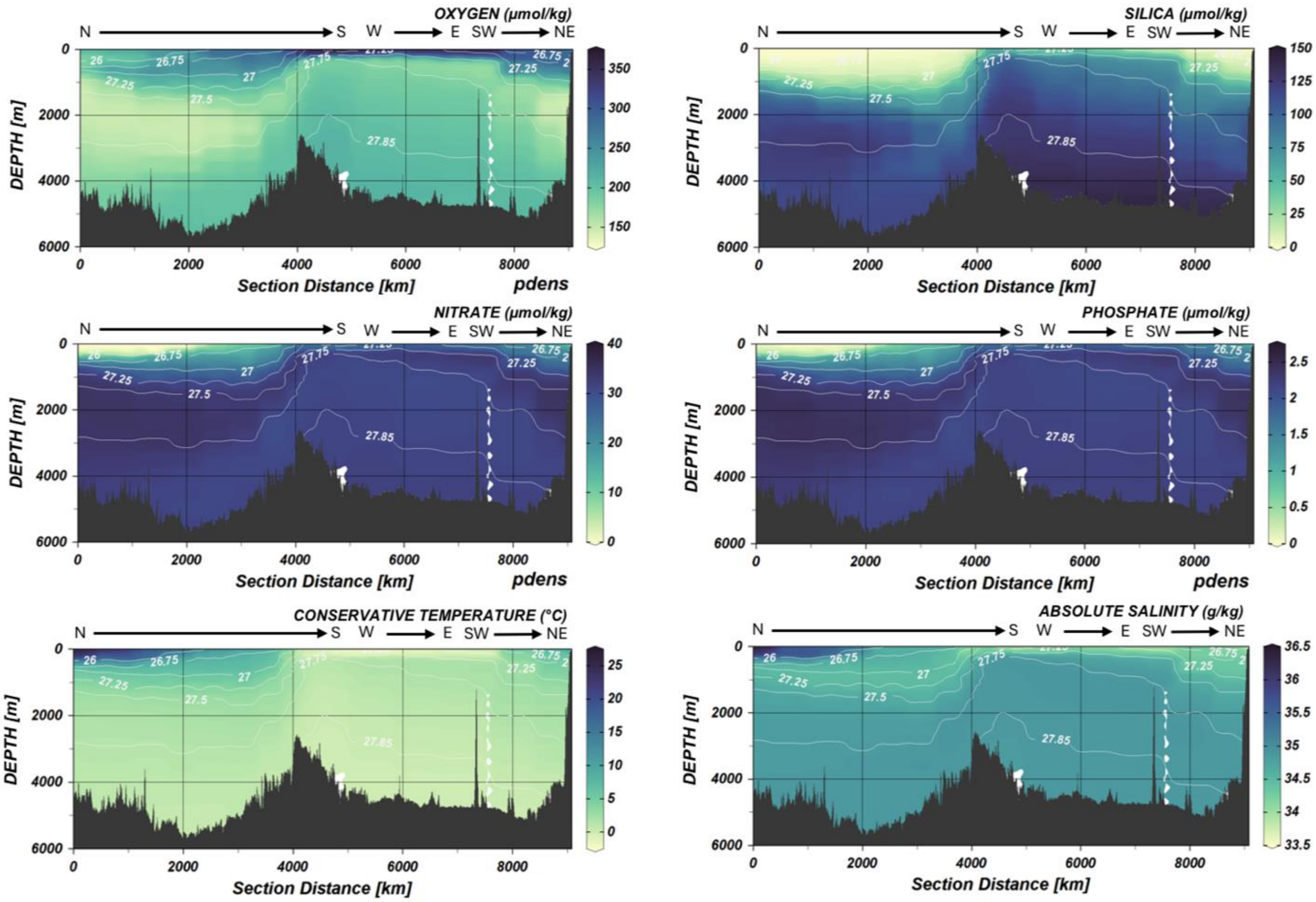

Figure 3.3 Mapped concentrations of temperature, salinity, and nutrients used in the OMPA across the entire GP17-OCE transect with bathymetry, using distance from station 1 (0 m, left) (Figure 2). It is important to note that this transect has both a latitudinal and longitudinal component, with the longitudinal component starting when the transect reached 67°S, or 4516 km here, and moving northeast starting at ~100°W, or 6957 km here.

remineralization was not explored here, as the entire transect is expected to be fully oxygenated and did not pass through any areas of known Oxygen Minimum Zones (OMZs).

	CT	SA	Phosphate	Nitrate	Oxygen	Silica
Aerobic Remineralization			1	15	138	10
Aerobic Remineralization			1	17	170	30
Weighting	12	8	6	4	2	2

Table 3.3 Weightings used in this pyOMPA. Weightings are based off of Evans et al., 2023, which uses the same pyOMPA code base for their analysis of ETNP data in the Pacific Basin. Remineralization values based on Redfield Ratio values for nutrients, as compared to Phosphate (value of 1).

3.4: Results

3.4.1 Water mass contributions

Contributions of water masses are plotted on a scale of 0 – 100% (0 – 1) (Figure 3.5) relative contribution with depth across the entire transect as determined by distance from Station 1 (Figure 3.3 caption). Eight water masses were transected by GP17-OCE and analyzed for this study: two mode waters (Southern Tropical Mode Water (STMW) and Subantarctic Mode Water (SAMW)), one surface water mass (Antarctic Surface Water (AASW)), one intermediate water mass (Antarctic Intermediate Water (AAIW)), three deep water masses (Upper Circumpolar Deep Water (UCDW), Lower Circumpolar Deep Water (LCDW), and Pacific Deep Water (PDW)), and one bottom water (Antarctic Bottom Water (AABW)). South Pacific Equatorial Pacific Water (SEqPIW), Tasman Sea formed AAIW, and Southern Ocean formed AAIW (Figure 3.1) were considered for inclusion in this analyses but were not found to influence the water masses in this region. Specifically, the endmembers for AAIW were found to be consistent with previously reported main AAIW formation region endmembers, and were not variable across the transect.

AASW and STMW are found in the shallowest waters (>500 m) and show very little influence on the output of the water mass analysis, however, the inclusion of these water masses that are found in heavily variable waters is imperative for good definition of all water masses below them. The ocean surface is notoriously difficult to characterize using these methods because of the large amount of variability temperature, salinity, oxygen, and nutrients that is seen in surface waters, and a uniform cut (here, at 250 m) of the most turbulent waters is necessary for proper definition of more conservative, deeper water masses. SAMW, the most surface water mass with a large contribution below the cutoff, is only present in low latitudes between 250 and 500 m in the water column.

AAIW is present between about 250 m (in some locations) to about 1200 m in the water column, in the first 4000 m of the transect and at stations 35-38, near the coast of Chile. One of the largest contributions of AAIW to the transect is found near Chile, in the main AAIW formation zone of the Southeastern Pacific (Hartin et al., 2011) that, after formation, moves westward where it intersects the GP17-OCE transect a second time in the "latitudinal" section. Although there are several instances of AAIW forming regions throughout the Pacific, most notably in the region of the Tasman Sea, (Hamilton 2006, Bostock et al., 2013) the AAIW formation that GP17-OCE transected is well mixed, leading to a density zone congruent across the entire transect. Therefore, one endmember set is sufficient to correctly define the AAIW contributions found here.

Circumpolar Deep Water (CDW) in the Southern Ocean is found at about 500 m depth in the water column and is a mixture of UCDW and LCDW. Here, the Upper Circumpolar Deep Water (UCDW, originating from evolved Pacific Deep Water (PDW) (Talley 2011)) and Lower Circumpolar Deep Water (LCDW, with origins in North Atlantic Deep Water (NADW) (Talley 2011)) show large southward movement and strong upwelling signals (Figure 3.5) past the Subantarctic Front (SAF), at 56°S. AABW is found to be a large and important component of the bottom water throughout the transect. As the densest deep water in the basin, most of the contribution of AABW to the measurements of this transect can be found south of the Pacific-Antarctic Ridge where it is formed, however, strong northward advection of upwelled and mixed circumpolar deep waters shows entrainment of some AABW northward. This means that a strong influence of AABW is seen past the ridge in the deep waters of the transect, mixing with LCDW from ~3000 m (Figure 3.5). PDW is formed in the North Atlantic Ocean and travels south, intersecting and mixing with LCDW/AABW between 1500 m and 4000 m before 56°S and near the coast of Chile at the very end of the transect. Contributions of PDW to this analysis are not extreme but do intersect a fairly large portion of the deep waters south of the equator.

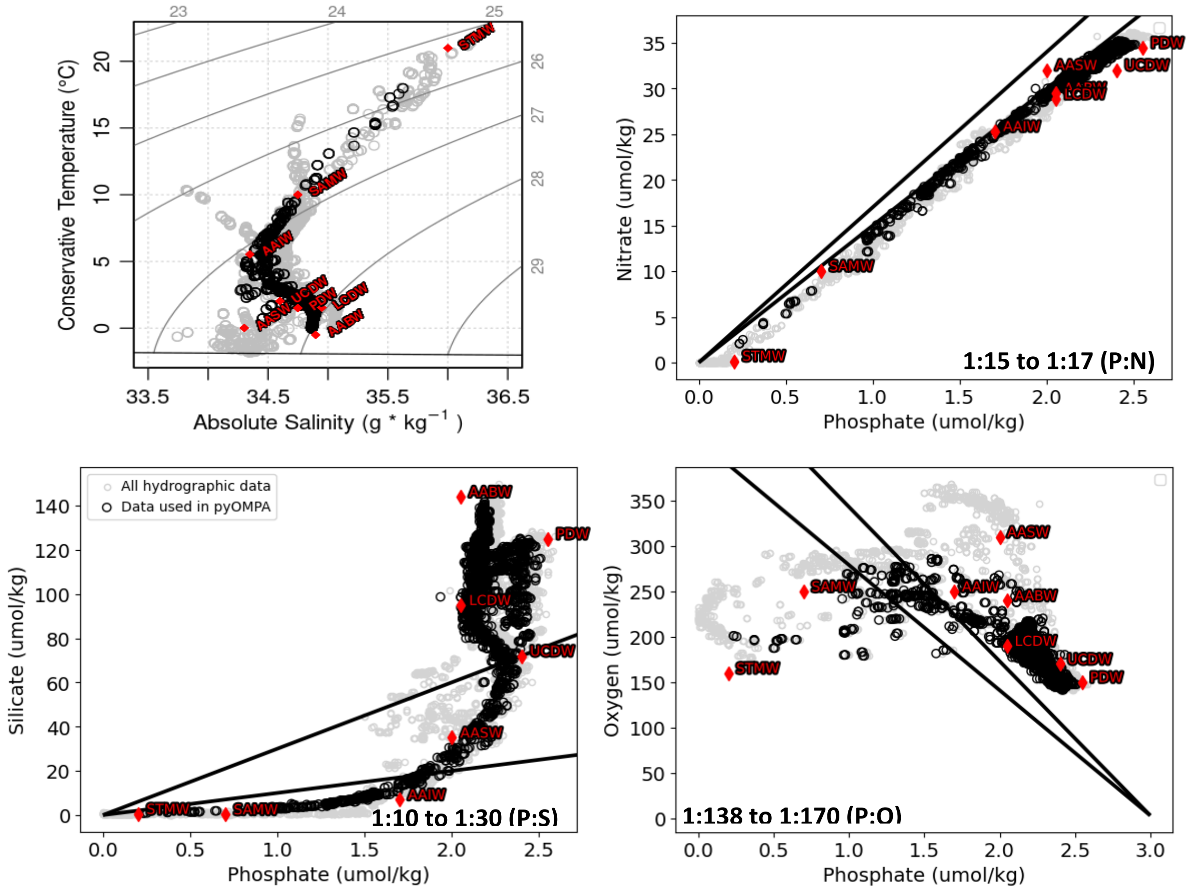

Figure 3.4 A) Temperature-Salinity (T/S) and B, C, D) nutrient plots of all hydrographic ODF data from GP17-OCE (gray dots) overlaid with data used for pyOMPA after 250 m surface and residual outlier value cuts (black dots). Endmember values for each of the eight water masses defined in this study are placed on top of all data and labelled (red diamonds) to show continuity in describing data. For nutrient plots, remineralization ratios are included as wedges and also written for clarity within each plot.

Aerobic remineralization across the transect was examined and is plotted versus depth in Figure 3.6. Aerobic remineralization is found to be occurring (positive) in most of the water column, only becoming negative near the bottom of the thermocline and the top of analyzed values for the water masses. Negative remineralization can indicate the chance for elevated carbon storage as the rate of organic matter breakdown decreases, leading potentially to decreased atmospheric CO_2 levels as carbon is stored in the deep ocean (Segschneider and Bendtsen 2013). Positive remineralization releases this carbon into the ocean, leading to increased ocean acidification (Piñango et al., 2022). The specific remineralization ratio of oxygen, nitrate, and silicate was compared to conservative phosphate across the transect (Figure 3.6). These ratios show a consistent positive ratio across nutrients in the LCDW, and oxygen specifically shows a positive ratio within the AAIW and SAMW water masses near the surface, below the surface.

The vectors placed over the nutrient plots show defined remineralization ratio ranges for nitrate (1:15 – 1:17), silicate (1:10 – 1:30), and oxygen (1:138 – 1:170) (Figure 3.4). These values are supported by previous studies for nutrient remineralization ratios within the Southern Pacific Ocean (Supplementary Table 3.3) that used a series of one- to three-endmember mixing models and measured observations to report updated ratios from the traditional Redfield values.

Water Mass	**Abbreviation**	**CT (◦C)**	**SA (g/kg)**	**Phosphate (µmol/kg)**	**Nitrate (µmol/kg)**	**Silica (µmol/kg)**	**Oxygen (µmol/kg)**	**Potential Density (kg/m^3)**
Antarctic Intermediate Water	AAIW	5.45	34.35	1.7	25.3	7	250	26.98
Subantarctic Mode Water	SAMW	10	34.75	0.7	10	0.3	250	26.63
Antarctic Bottom Water	AABW	-0.5	34.9	2.05	29.5	144	240	27.92
Pacific Deep Water	PDW	1.5	34.75	2.55	34.45	125	150	27.68
Lower Circumpolar Deep Water	LCDW	1.55	34.95	2.05	28.85	95	190	27.84
Upper Circumpolar Deep Water	UCDW	2	34.60	2.4	32	72	170	27.52
Antarctic Surface Water	AASW	0	34.3	2	32	35	310	27.41
Southern Tropical Mode Water	STMW	21	36	0.2	0.15	0.5	160	25.12

Table 3.4 Defined water mass endmembers for the eight water masses defined in this study. Both Southern Tropical Mode Water (STMW) and Antarctic Surface Water (AASW) endmembers lie above the thermocline cutoff used in this study, however, the inclusion of these water masses is imperative for precise definition of all deeper water masses in the study area.

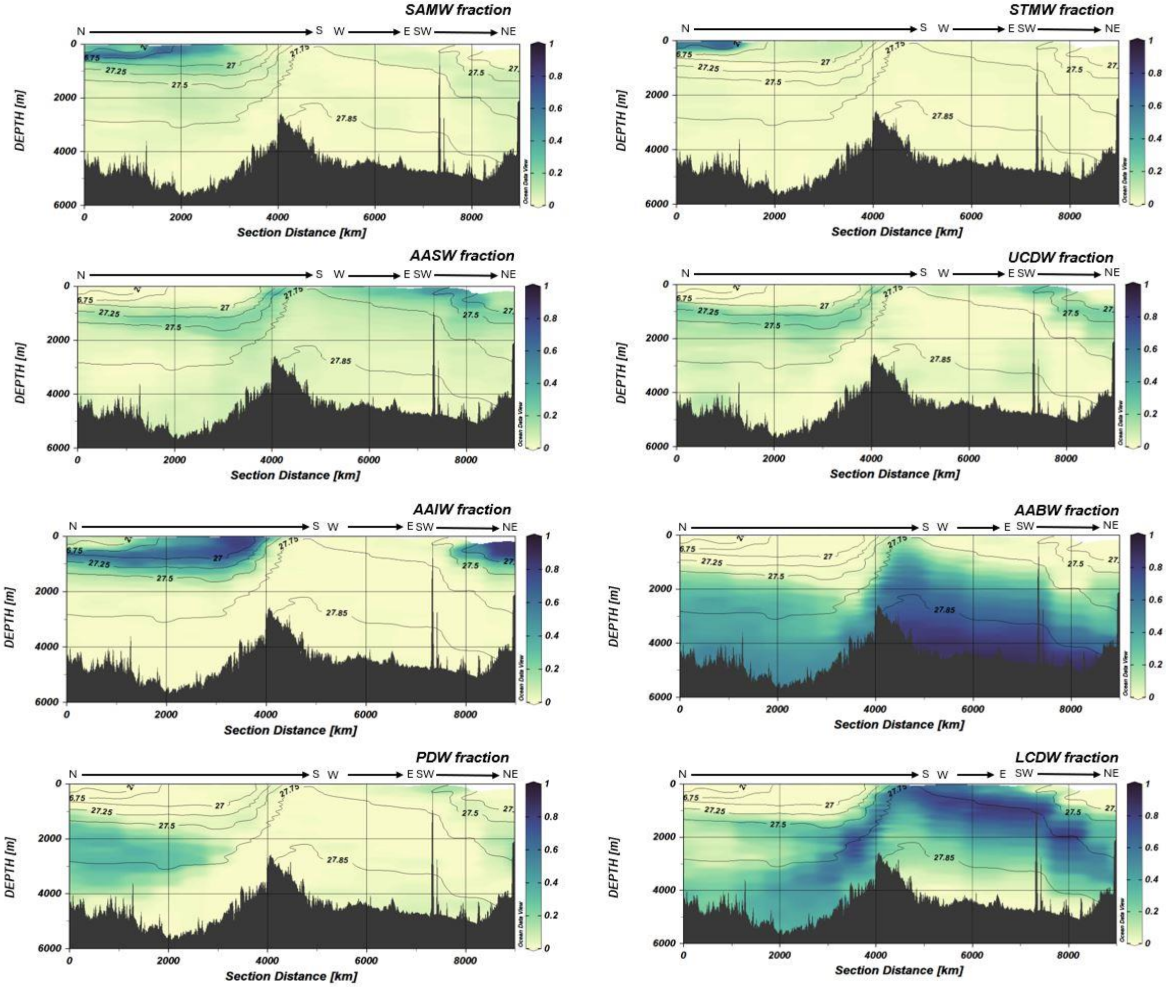

Figure 3.5 Contributions of each of the eight defined water masses to waters across the GP17-OCE transect, on a scale of zero to 1, where 1 indicates the core of each water mass. Core endmembers were not captured for surface water masses STMW and AASW, as well as deep water mass PDW. Water mass movement through the water column, through upwelling (UCDW, LCDW) and downwelling (AASW) can be seen in two areas of the transect, as the pseudo-northeast section of the longitudinal transect ventured back into northern waters. This is also seen by inclusion of AAIW and PDW in both the latitudinal and longitudinal sections of the transect.

3.4.2 Residuals

Residual error for given properties is plotted as a result of the extended pyOMPA for each variable used in water mass percentage analysis (Figure 3.6). These values, placed on a real scale – unlike the scale used for water mass contribution, shown as percentage – quantify the error for endmembers of each water mass based on their location within the water column at defined latitudes, which is expressed through percentage contributions of each water mass in the basin, explained in section 3.4.1 (Figure 3.4). A value of zero in residuals is obtained when the combination of linear mixing equations and endmember definitions of variables used in the analysis (predicted water mass properties) perfectly predicts the observed properties of the sampled waters. A near-zero value was targeted for each variable's residuals, with a maximum range of 0 ± 0.2 used here to define the final set of endmembers in this analysis (Table 3.4). This range has been used in previous studies (Evans et al., 2020, Evans et al., 2021, Peters et al., 2018) that completed water mass analyses of the Pacific Ocean Basin, and shows a good understanding of the core water mass values for the eight water masses defined in this transect.

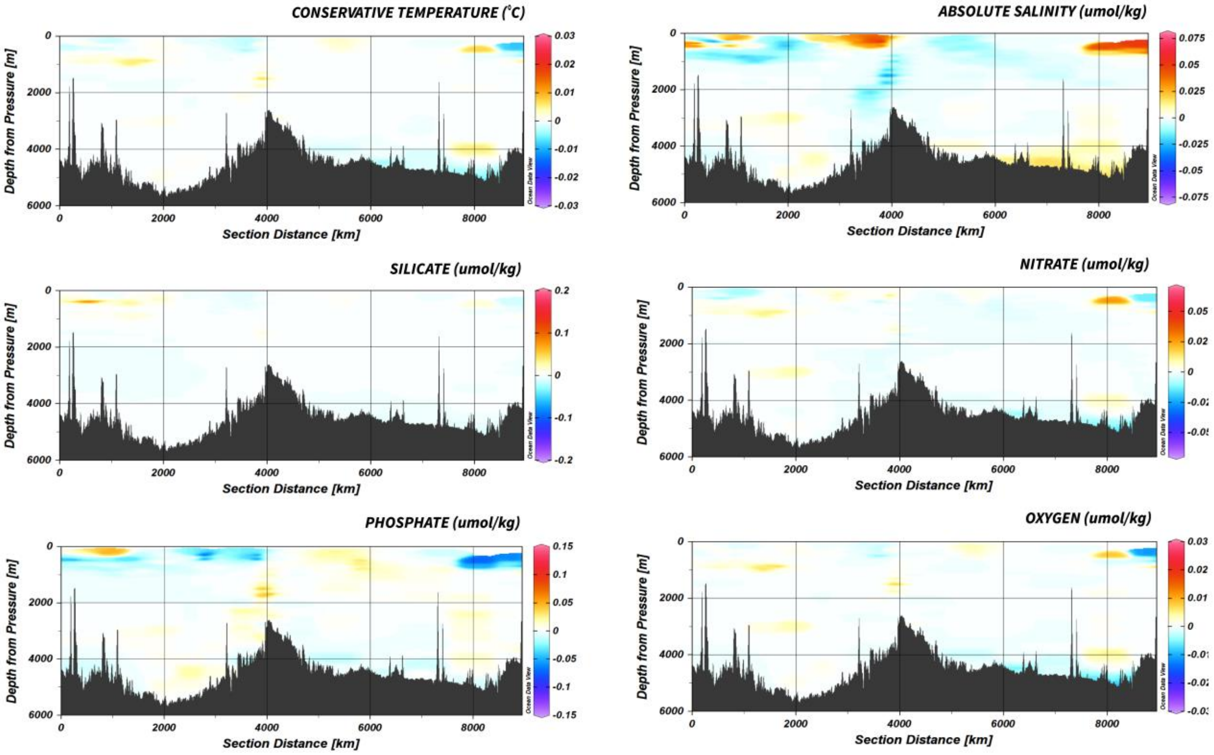

Figure 3.6 Residuals of all factors used in the water mass analysis of the Southern Pacific Ocean. Residuals are listed on a real scale and provide the error of each factor in the positive and negative direction across the entire transect. A residual of zero means a perfect match for each factor as defined by endmembers in the analysis.

Study	CT	SA	Phosphate	Nitrate	Oxygen	Silica
This study	± 0.04	± 0.1	± 0.1	± 0.075	± 0.04	± 0.2

Table 3.5 Final residual value ranges for each factor within the study area for GP17-OCE.

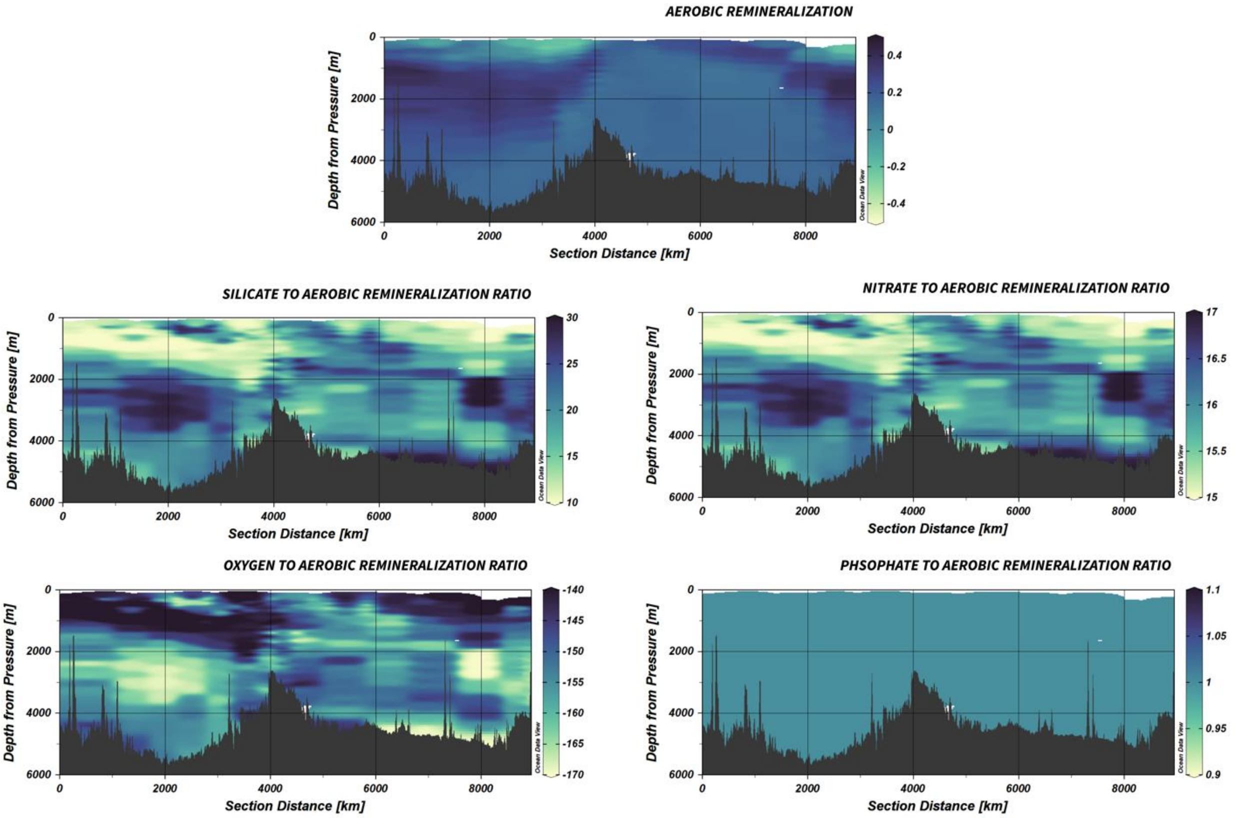

Figure 3.7 Calculated remineralization rates and aerobic remineralization ratios for silica, nitrate, oxygen, and phosphate (Table 3.3). Surface waters low in oxygen show most negative remineralization rates in the water column.

3.5: Discussion

Eight water masses were identified within the GP17-OCE cruise transect on its passage through the Southern Pacific Ocean basin (Table 3.1). Of these water masses, AAIW, LCDW, and AABW were determined to have endmember or near endmember compositions captured along the transect (>89% composition in any sample) after the omission of conflating surface data for the analysis. The other water masses defined here – SMTW, SAMW, AASW, PDW, and UCDW – did not have large full-endmember representative areas captured, but were found to have major contributions along the transect. Importantly, we also note that in some cases, two water masses were transected twice in the study (AAIW and PDW), which is due to their broad presence in the region and the three pseudo-transect orientations (S-N, W-E, SW-NE) of the GP17-OCE cruise across the South Pacific broadly.

In the following discussion, we outline: 1) water mass endmembers determined in this study and their formation regions; 2) the general distribution of water masses; 3) implications for nutrient and TEI distributions, including iodine, across the South Pacific.

3.5.1 South Pacific water masses

3.5.1.1 Defining the surface

An important step in defining endmembers is determining the regions in which the OMPA properties are most conservative. Surface waters are notoriously difficult to define by pyOMPA (Llanillo, et al., 2013, Peters et a., 2018, Silva et al., 2009), as the nutrients that are used in the calculation of water mass endmembers are generally non-conservative at the surface (Figure 3.3). Therefore, for accurate representation of deeper water masses that are generally more conservative, and that are more consistent in their definitions, it is helpful to define an area of data that represents the surface, or, more specifically, the area of changing or known non-conservative factor values that hinder strong definitions of water mass endmembers. In previous studies, these surface waters have been defined based on density and are generally cut for everything that is not intermediate waters and below, or around 27.1 kg/m^3 (Peters et al. 2018, Evans et al., 2020) in northern and near-equatorial South Pacific waters. These previous studies defined areas of the Pacific that were more consistent in surface density across their entire transect, and, therefore, a single density cutoff defined the surface waters in their transect areas. GP17-OCE, while not necessarily longer than these other transects, passed through temperate waters just south of the equator and moved to very variable high latitude waters near Antarctica, then moved East to end along the coast of Chile (Figure 3.2). The movement of this transect through these large chemical gradients is a strength and the intent of the selected cruise transect, especially in the hydrographic data used for pyOMPA; however, these variations and highly differing surface waters and water masses meant that a standard density cutoff like those used before was not possible for this data.

The differences in C_T and S_A, and the resulting density, of the three surface and near-surface water masses defined in this study – the STMW and SAMW in the north and the AASW in the south –is the most important factor preventing a clear density boundary used to define the surface for the purpose of the OMPA (Figure 3.4). Specifically, STMW is found here to be light in density compared to previous definitions (Figure 3.8) at 25.12 kg/m^3, while AASW is reported to be much denser, at 27.4 kg/m^3. Just below these water masses, SAMW is found to be at 26.63 kg/m^3 and the AAIW at 26.98 kg/m^3. Because STMW, SAMW and AAIW are all less dense than the AASW in the south, it is challenging to define these surface waters based solely on density, as previous studies have done in North Pacific and near-equatorial waters. Here, applying a density cutoff would mean deep unnecessary cuts in the transect north of 56°S, especially in AAIW.

By instead recognizing the importance of defining the near surface water masses (STMW and AASW) and cutting the surface based on depth alone at 250 m, we are able to include all water masses present in the water column and create a more accurate definition of the Southern Pacific Ocean water masses (Figure 3.5). Over the entire transect, a uniform depth cutoff of 250 m was placed, effectively removing turbulent surface waters from the calculations of water masses across the transect. STMW and AASW are still included in the calculation of the OMPA itself, but most of their instance across the transect and their 100% endmember values are cut from the calculations as they are in majority found at or above 250 m in the water column. Fringe values for these water masses are still seen in waters just below 250 m, as shown in Figure 3.5. Values for all factors used in the OMPA taken at depths deeper than 250 m are used in the OMPA calculations and are not considered part of the surface waters. The use of a single OMPA for all water masses in the transect with depth is a rigorous approach and used to define all waters together, where some previous water mass analyses have split the water column into two or three separate OMPAs for better fit of error between defined water masses (Peters et al., 2018, Lawrence et al., 2022).

3.5.1.2 Water mass endmembers definitions

We compared our water mass endmember definitions to that of ranges of previous reported values from studies of water masses and OMPA-based water mass analyses (Figure 3.8). Our determined water mass endmembers are generally comparable with previously defined values (Table 3.4, Table 3.2), but some variations are observed. Below we discuss our endmember values in the context of the observed data ranges, justifications for our reported ranges relative to those observed in previous studies, and the resulting distribution and values of residuals quantifying error in our endmember analysis (Figure 3.6, Figure 3.8).

The most important first step in determining the legitimacy of endmember values is ensuring the combination of water masses captures the data ranges for input parameter into the OMPA. Figure 3.4 shows comparisons of the transect data and calculated endmembers for each C_T-S_A. This is an important check on endmember placement once the transected water masses for inclusion to the analysis are determined. Predicted endmembers that land outside of known data should be treated with some suspicion and possibly iterated for better placement. Understanding factor minimums and maximums (i.e. salinity, oxygen, nutrients) for each water mass can help in understanding of the correct placement of these endmembers on real data (i.e. AAIW as a salinity minimum). In Figure 3.4, we show both the entirety of the dataset for GP17-OCE (gray circles) and the data used after 250 m surface cutoff and outlier cuts (black circles), with endmember definitions placed on top of this data (red diamonds). It is easy to see in this way, for example, that the STMW and AASW endmembers are not captured in the OMPA—as their 100% contribution falls far outside of the included data—but are necessary for characterizing the full data range. This is true for each of the four diagrams, including those for nitrate, silicate, and oxygen, all compared to the most conservative nutrient used in this calculation: phosphate (PO_4)

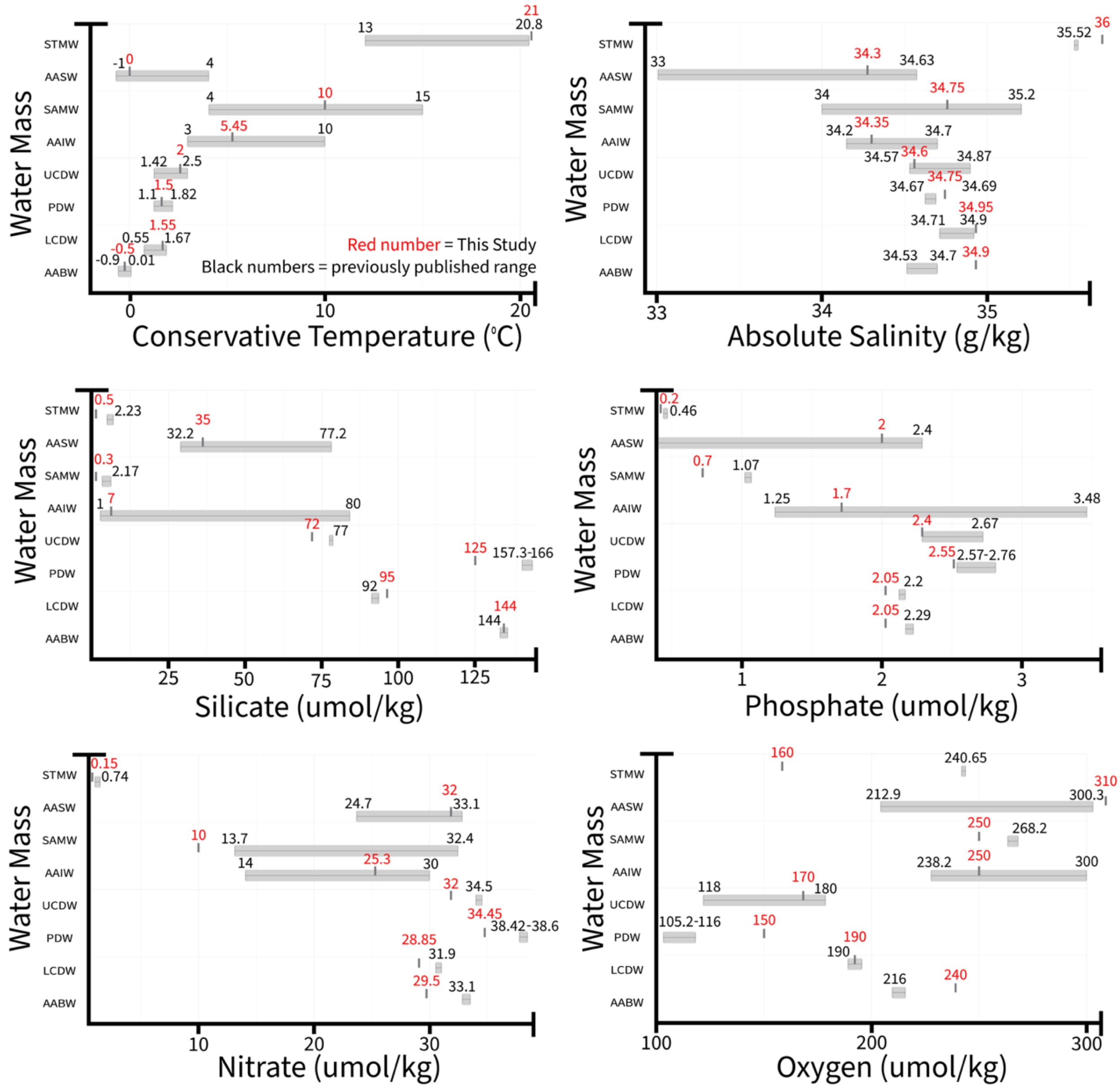

Figure 3.8 Ranges of factors used for OMPA reported in previous studies (gray boxes and black values) overlaid with end member definitions used in this study (gray vertical lines and red values).

Importantly, while our OMPA across the GP17-OCE transect offers an opportunity to better constrain regional water mass formation and distribution, previous studies in the South Pacific offer an important ground-truthing opportunity. Values that are not in range of previous reports are those of the included nutrients (phosphate, nitrate, silicate, and oxygen), and are, even then, close in value to the expected range. The northern surface waters (STMW and SAMW) see the most variation and largest differences from expected values (Figure 3.6). This is not surprising, as surface waters are known to be more difficult than deeper waters to define, and their interaction with the air and high amount of mixing will cause highly variable values for non-conservative factors. Nearly all temperature and salinity values were found to be very closely in range or, at most, have a <1.33% offset from previously reported values. Because of this, all calculated values of potential density, included in the endmember table for reference checks on temperature and salinity endmembers, were found to be aligned with previous values, as well (Table 3.4).

A few endmembers of note defined in our water mass analysis differ from previously reported values for nutrients in the Pacific, although most by less than 30%. First, the PDW defined here has a lower silicate value than previously reported, being defined here at 125 µmol/kg, while previously reported at about 160-170 µmol/kg (Reyes-Macaya et al., 2021 and Peters et al., 2018, Lawrence et al., 2022). PDW also has a slightly higher oxygen level than previously reported, reported here at 150 µmol/kg while previously reported around 105-140 µmol/kg (Reyes-Macaya et al., 2021 and Peters et al., 2018, Lawrence et al., 2022). In AABW, our oxygen value is reported at 240 µmol/kg while previously reported at a slightly lower value of 216 µmol/kg (Peters et al., 2018, Lawrence et al., 2022). Finally, all nutrients for the STMW are found here to be slightly lower than previously reported by Reyes-Macaya et al., 2021, with nitrate at 0.2 µmol/kg vs 0.46 µmol/kg, phosphate at 0.15 µmol/kg vs 0.74 µmol/kg, and silicate at 0.5 µmol/kg vs 2.23 µmol/kg (Table 3.2, Table 3.4). The concentration of these components in the open ocean can be varied by many factors, including specific conditions at time of sampling.

It is important to note that the specific values for these nutrient comparisons listed above refer specifically to three previous water mass analyses of the Pacific Ocean that took place in separate areas from this study – one between the Equator and 60ºS at 90ºW (Reyes-Macaya et al., 2021), one through the Eastern Tropical North Pacific (ETNP) from the coast of Peru west to Tahiti (152ºW) across an area of known oxygen minimum (OMZ) (Peters et al., 2018), and one through the Northern Pacific from Alaska to Tahiti (Lawrence et al., 2022). Endmembers from these cruises were defined based on data from several World Ocean Circulation Experiment (WOCE) cruise transects (Reyes-Macaya et al., 2021), the CLIVAR (Climate Variability and Predictability) repeat hydrography cruise at P18 (Peters et al., 2018), and the Global Ocean Data Analysis Project version 2 (GLODAPv2) (Lawrence et al., 2022) to define forming regions of each water mass selected for the analysis, and define them based on forming region so as to calculate their influence on sampled waters. Reyes-Malaya et a., 2021 focused on coastal waters near the Peruvian margin, and used $\delta^{18}O$, δD, and $\delta^{13}C_{DIC}$ along with temperature, salinity, oxygen, and nutrients to defined water masses in the area. Peters et al., 2018 used MATLAB OMPA with temperature, salinity, nitrate, nitrite, silicate, phosphate, and oxygen to define water masses across the GEOTRACES GP16 cruise transect, where there is a secondary nitrite maximum in the Peruvian OMZ. Lawrence et al., 2022 used pyOMPA, as is used here, to determine the water masses present along the GEOTRACES GP15 cruise transect, using the same parameters as this study: temperature, salinity, nitrate, silicate, phosphate, and oxygen. Although these three studies used different methods of determination for the water masses, all three came to similar conclusions about their distribution and occurrence across the Pacific basin. Therefore, it is important to note that our water mass definitions fit well with these previous definitions (Figure 3.8), and we are not attempting to define here novel water mass endmembers that have not been discussed in other studies focusing on this region, but our constraints on their South Pacific Distribution are novel.

Residuals found as a result of these calculations are low and within range of previous pyOMPA studies (Evans et al., 2023, Lawrence et al., 2022). Clear outliers were excluded from the data as determined from very high residuals and cross-checking with the metadata to confirm that the point was outside normal data bounds for the area. Exclusion of these outliers and many rounds of iteration of endmember values allowed for very precise endmember values, extremely low residual error values, and high confidence in the values used to describe all water masses included in this study (Figure 3.6). The highest residuals are found for silicate (± 0.2), phosphate (± 0.1), and absolute salinity (± 0.1). With the importance of the weighting of the variables in mind – in this case, absolute salinity and conservative temperature with the highest weightings and therefore being assigned the highest importance in their definitions – these residuals tell us that there is the most uncertainty in silicate, phosphate, and absolute salinity within our chosen endmember definitions for these water masses. Importantly, these residual values are not large in accordance with previous studies (Evans et al., 2020, Evans et al., 2023, Peters et al., 2018), however, it is important to resolve possible sources of error within the initial water mass definitions for a clear understanding of results. The largest sources of uncertainty are located at the surface and generally within areas of water masses located above 1000 m. This is unsurprising, as surface waters are notoriously difficult to constrain and the semi-conservative nature of nutrients used in the OMPA is less true in surface waters where biogeochemical activity is prevalent and vertical mixing plays a larger role in definitions. Lower residuals are found in deeper waters where water changes are slower, and the values of all factors are more conservative.

3.5.1.3 Water mass formation regions

Although there are eight identified individual water masses along the GP17-OCE transect (Table 3.1), this cruise passes through the known forming region of only one of these waters – the "main" AAIW forming region off the coast of Chile (Figure 3.1). AAIW has three individual forming regions in the Pacific (Figure 3.1), and in the southeast specifically, it is partially formed from a mixture of Ekman transport and subduction of AASW north of the subantarctic front (SAF) in the Drake Passage (Bostock et al., 2013). Although this forming region is well-known (Bostock et al., 2010, Bostock et al., 2013), evidence for the cruise transect crossing through this forming region is immediately apparent in the results of the OMPA (Figure 3.5), as the fraction of AAIW as defined by endmembers (Table 3.4) in this region (station 35 through 37) reaches over 80%, surpassed only by a small region between stations 12 and 14 where this fraction reaches up to 91.5% (Figure 3.5). The remainder of the transect shows areas that reach between 0 and 80 percent, especially in the northern part of the latitudinal transect, but the majority stays below 10%. Because this large fraction contribution to AAIW is found near the end of the longitudinal transect, we can reasonably say that the endmember of AAIW from the Southeast Pacific forming region was captured, and the influence of AAIW spreading from this forming region out to the open ocean basin allows for the capture of this same water in the latitudinal section of the transect, as described in following sections.

The longitudinal section of the GP17-OCE cruise does not intersect but follows in parallel the region of greatest AASW influence, along with regions used for definition of UCDW, LCDW, and AABW (Figure 3.1). Dense AABW is formed from a mixture of dense brine-rejected AASW and upwelled LCDW and sinks deep into the Southern Ocean below the ACC which will carry it eastward around the Antarctic (Talley 2013). UCDW that is upwelled to Southern Ocean waters through the Pacific is warmed and mixes with surface waters, returning north to contribute to AAIW formation (Talley 2013). Upwelling of UCDW and LCDW brings high concentrations of nutrients to the surface ocean in the South Pacific, which contributes to high biogeochemical activity in these areas. The GP17-OCE cruise track crosses areas with a significant portion of the endmembers of these waters – with AABW captured up to 92%, LCDW up to 89%, and UCDW up to 52% below the 250 m surface cutoff. UCDW is concentrated significantly at the very surface of these waters after upwelling, so the endmember waters are further removed by this parameterization.

The mode waters – STMW and SAMW – are formed from deep winter mixing that allows for their distribution down to 500 m in the water column (Talley 2011, Hanawa and Talley 2001) and across large surface areas of the Pacific basin. Specifically, the South Pacific STMW (SPSTMW) is generally located between New Zealand and Fiji, north of the Tasman Front, and is relatively thin compared to other mode waters in the Pacific (Hanawa and Talley 2001). These waters are formed north of the SAF in the Pacific, and as the GP17-OCE cruise transect moved through the northernmost part of its transect south of Tahiti, we capture up to 78% (SAMW) and 79% (STMW) of the endmember waters for these water masses (Figure 3.5). AASW, the only true surface water that is sampled in this cruise, is formed behind the SAF and is a typical surface water with local origin (Talley 2011). AASW was encountered along the GP17-OCE cruise transect at its southernmost points along the longitudinal portion of the cruise transect (Figure 3.5). We capture 56% of the endmember waters of AASW in the calculations for the OMPA at depths deeper than 250 m beyond 60°S. Because most of this surface water is trimmed with the 250 m surface cutoff for analysis, much of the surface STMW and AASW were removed from the analysis.

The final water mass sampled, PDW, enters the South Pacific basin from the north above the NADW. The GP17-OCE cruise sampled waters at the end of the PDW's influence in the South Pacific at the beginning of the latitudinal transect and the end after the cruise's pseudo-northward transect at the end of the cruise. Fractions of up to 50% for PDW were measured by the water mass analysis for these samples.

3.5.1.4 AAIW and PDW: two zones, one "flavor"

While water masses may evolve due to non-conservative or semi-conservative parameters (e.g., nitrate, phosphate, silicate, and oxygen) or even have multiple formation regions (e.g., AAIW). We found the two water masses transected in multiple locations during GP17-OCE (AAIW and PDW) to each have a single endmember definition (Figure 3.1). This is particularly relevant to AAIW and PDW, which are found to be present in two distinct areas of the transect, along the latitudinal transect and the final stations of the longitudinal transect. The longitudinal portion of GP17-OCE passes through a major area of AAIW influence in the latitudinal transect and ends through the main AAIW forming region off the coast of Chile (Bostock et al., 2013, Bostock et al, 2010). It is interesting to observe that the endmember value is almost completely captured at these stations, as the AAIW trends to 80% only at these final stations, and as it moves out from this region and is bisected by the latitudinal stations, its inclusion is generally only around 60% except for one region between stations 12 and 14. We note that other TEIs not used in this water mass analysis may better distinguish AAIW source regions and improve on our understanding in future studies.

AAIW has varying core depth across the Pacific Ocean, as it is found across the basin from about 15ºN to about 60ºS. Differing core densities based primarily on latitude can be found in the main southeast AAIW forming region near the coast of Chile ahead of the Subantarctic Front (SAF), a second, more westerly southern ocean (SO) forming region between 120ºW and 150ºE, and a final third forming region in the Tasman Sea (Bostock et al., 2013) (Zenk et al., 2005) (Figure 3.1). At 152ºW and from 20ºS to 67ºS along the latitudinal portion of the GP17-OCE transect, Zenk et al., 2005 shows that the core density of the AAIW encountered in this area is around 700 m depth. This is consistent with the results of our analysis (Figure 3.5), as our core AAIW sits near 700 m in the northern regions where the water mass is not actively subducting, and at stations 35 through 37, where the longitudinal transect heads north through the forming region and intersects AAIW for a second time.

Pacific Deep Water is also found at these two distinct areas of the transect, however the reason is different than for AAIW. PDW flows in from the north, (Figure 3.1, Figure 3.9) above the North Atlantic Deep Waters (NADW) into the South Pacific (Talley 2011). As it is flowing in from the north, our transect crosses areas of PDW twice where samples were taken north of 56ºS (Figure 3.5). These instances, like AAIW, are also described with one final set of endmembers. The endmembers of PDW are also found on the very edges of included hydrographic data for the pyOMPA, and the true endmember is not captured in the analysis, as with the two most surface waters (section 3.5.2.1). Although PDW is not directly involved with waters that are upwelled along the South American margin, it is possible that PDW waters here may be affected by regional upwelling and movement of nutrients and other semi-conservative tracers from deeper waters. It is important to keep these factors in mind when considering endmembers for PDW in this area as it moves south.

3.5.2 Water mass distributions

3.5.2.1 Surface water masses and their contributions to deeper water masses

Upwelling and subduction of deep and bottom waters can be visually interpreted by semi-conservative nutrients that are used in pyOMPA to define regions of specific water mass contribution through the GP17-OCE transect (Figure 3.3). Importantly, the subduction and even age of these water masses can be tracked by stable $\delta^{18}O$, SF6, chlorofluorocarbons (CFCs) (Reyes-Malaya et al., 2021, Hartin et al., 2011, Rodehacke et al., 2007), and other atmospheric derived tracers reset while the water mass is at the surface. These alternative tracers can be used to differentiate surface and deeper water masses and track the rate of subduction of deeper water masses in open ocean basins. Although these factors are not measured here, it is important to understand the evolution of surface water masses into intermediate, deep, and bottom waters and the effect that this subduction has on the movement of other nutrients used in water mass analyses. Below we discuss the formation and important aspects of water masses constrained in this analysis that help to determine their influence on the GP17-OCE transect.

Of the three surface water masses determined by the pyOMPA, the AASW and STMW endmembers are least captured in the transect but play an integral part in the definition of the other six water masses that make up the bulk of the sampled area with depth and latitude (Figure 3.5). The AASW and STMW endmembers that indicate “core” instances of these waters are found to be on the very edges of the data used in the pyOMPA (Figure 3.5), but these waters mix and nutrients are likely to diffuse to the next most surface water masses and they themselves are present in small amounts below 250 m. These water masses are therefore important even below the surface water threshold determined for the water mass analysis here. Although it is still very difficult to constrain the very surface ocean in general, the inclusion of these two edge surface waters allows for a better constraint on intermediate and deep waters along the GP17-OCE transect specifically. Without their inclusion, the small amount of surface water mass values that are included in the surface-cut data appear as outliers and significantly increase residuals for every factor included in the pyOMPA. These two surface water masses are individually important members of the “latitudinal” and “longitudinal” sections of the transect, respectively. The AASW, in part because of its very high density (Table 3.4), is also a major player in intermediate water mass definitions. As AASW subducts after mixing with surface UCDW from higher latitudes, it forms SAMW and AAIW in the water column, therefore becoming a more permanent part of the Southern Pacific basin after forming itself from ice shelves near Antarctica (Zhou et al., 2014). Importantly, it is possible to see the difficulty in defining these surface waters in the residuals for these water masses at the surface and just below the 250 m surface threshold in Figure 3.6. Higher residuals in these surface areas highlight the difficulty in constraining surface water masses and their presence below the surface cutoff defined here is visible.

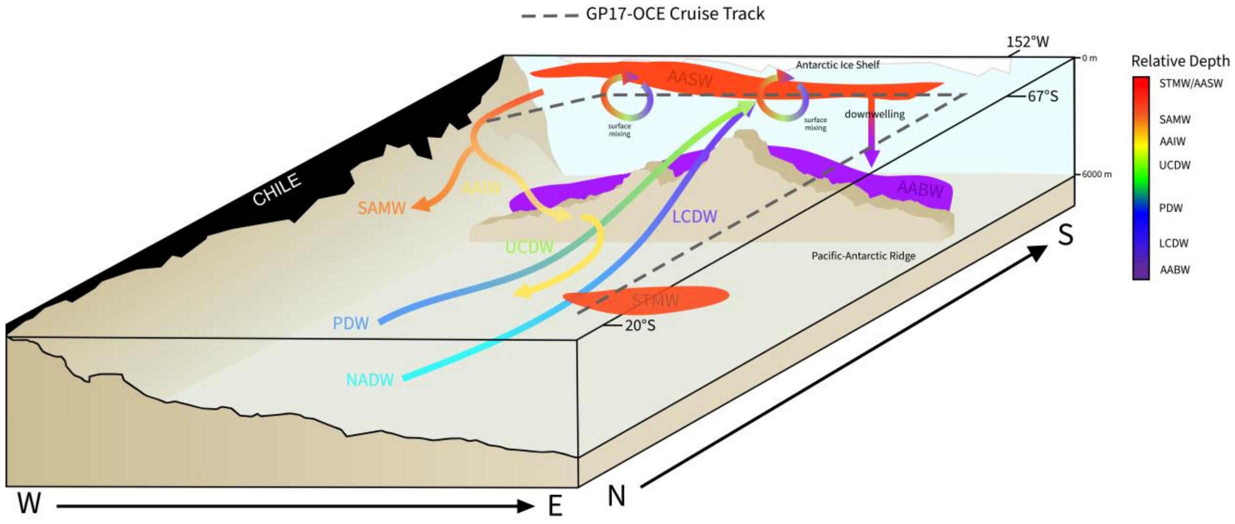

Figure 3.9 Visual interpretation of water mass inclusions into the Southeast Pacific. Arrows indicate direction of upwelling or movement into transect area. GP17-OCE transect indicated by gray dashed line on surface of ocean.

3.5.2.2 AABW North of the Pacific Antarctic Ridge

The deep water masses present in this transect move in from the North as PDW or mixed UCDW and LCDW, the latter of which upwell to the surface at high latitudes around Antarctica. These deep waters make up much of the water column, and the UCDW and LCDW are very prominent as they upwell from mixed deep waters where they are formed in low latitudes into higher latitudes at near-surface depths, bringing high concentrations of nutrients with them from nutrient rich, old waters. Particularly for this transect, the endmember for the UCDW is only barely captured after the cut data for the pyOMPA is determined (section 3.5.2.1) – the area of "core" UCDW is found very close to the surface in this transect near Antarctica and decreases in influence quickly through the water column. The most major player in these waters for GP17-OCE is LCDW, shown very prominently throughout the transect as is upwells through from northern waters to the south in both the latitudinal and longitudinal sections of the transect as it moves from lower latitudes towards higher latitudes (Figure 3.5). The PDW can be seen somewhat bisecting the LCDW as it moves in from the north, as it sits at a similar density range to the LCDW and is known to be part of UCDW's formation history.

The only bottom water transected by the GP17-OCE cruise is the AABW, which is formed from Antarctic Circumpolar Current (ACC) waters (Talley 2011) and is the densest of the deep water masses in this study, as it has the lowest temperature of all the water masses considered here and a relatively high salinity as intense cooling and sea ice formation create very dense waters that sink to the bottom of the ocean near Antarctica (Solodoch et al., 2022) (Table 3.4). Core AABW sits just behind the Pacific-Antarctic ridge, however, it is important to note that it does have some influence north of this ridge, either from upwelling or mixing with LCDW which brings it northward as it subducts after mixing with surface waters (Figure 3.5) (Baker et al., 2023).

AABW is formed at high latitudes south of the Pacific-Antarctic Ridge and, because of its high density, the majority of this water mass stays at high latitudes at the bottom of the water column behind this ridge (Figure 3.9). However, this water mass analysis indicates that a portion of AABW moves to lower latitudes, likely as a result of upwelling and mixing with LCDW. The similarities between the two water masses become important because of AABW's influence north of the Pacific-Antarctic Ridge. For example, the Deep Western Boundary Current (DWBC) pulls AABW that is formed in the Weddell Sea northward through the Drake Passage into the South Atlantic (Talley 2011) and carries these dense waters northward. This is likely possible because of mixing with the less dense LCDW directly above it, which will then continue to mix with ever lighter waters as it is pulled northward (Baker et al., 2013) (Figure 3.5). It is likely that a similar process occurs in the deep southern Pacific Waters, and the AABW formed here mixes with lighter upwelled LCDW and is pulled northward to a mild extent as a result of mixed LCDW downwelling with surface waters across the Pacific Antarctic Ridge to form AAIW. The majority of AABW is still found in the deepest waters behind this ridge, as movement on its own is inhibited by topography.

3.5.3 Implications for nutrient and TEI distributions

3.5.3.1 Sources of nutrient variations

Aerobic remineralization ratios are provided as part of the pyOMPA definitions for calculation, and remineralization ratios are included as part of the OMPA output for visual understanding of nutrient distribution and use across the area defined in the water mass analysis (Figure 3.7). Remineralization rates are found here to be negative in surface waters slightly below 250 m, increasing to their highest positive values around 1000 m, and then steadily decreasing with depth through the remainder of the water column. Oxygen is consumed in the process of aerobic remineralization, and this must be considered when measuring the concentration and distribution of oxygen as a nutrient in the water mass analysis in waters with high amounts of anticipated remineralization.

The process of remineralization releases pre-formed nutrients (i.e. phosphate, silicate, and nitrate) back into the ocean by organic matter breakdown in surface waters (Figure 3.3, Figure 3.7). These nutrients were previously locked in primary producers, and their release adds to the concentration of some semi-conservative nutrients that are included in the calculations for this extended OMPA. Cabbeling of these released nutrients increases the density of deeper water masses (Carter et al., 2014) and has a substantial role in the formation of AAIW and AABW. The amount of nutrients that are available in the water column is heavily influenced by the amount of remineralization that occurs in deeper waters, but the nutrients' main form of distribution is mediated by mixing of surface waters and processes like upwelling and vertical diffusion that change the concentration of nutrients in the water column. As bacteria and phytoplankton in the surface waters die and slowly sink to deeper depths, these pre-formed nutrients are accumulated to a high degree in deeper water masses. Mixing processes then move these nutrients within the water column can be quite slow, and it can also take a significant amount of time to reintroduce accumulated nutrients to the surface from deeper, more dense waters (Sigman and Hain 2012). These variations and drivers of distribution are important to consider when visualizing patterns of aerobic remineralization across the entire GP17-OCE transect.

3.5.3.2 Contribution of iodine to water masses along the GP17-OCE transect

Iodate was measured as described in Chapter 2 of this dissertation (Figure 3.10) along the entire transect of GP17-OCE at 24 of 38, including stations 1 and 38. Iodine follows well known trends of distribution across the South Pacific (Chance et al., 2014, Moriyasu et al., 2023, He et al., 2013, Chance et al., 2010, Moriyasu et al., 2020, Tsunogai and Henmi 1971), with a distinct increase in value from surface to depth in lower latitude regions where IO_3^- is rapidly reduced by bacteria and phytoplankton in the surface ocean (Hepach et al., 2020, Moisan et al., 1994, Bluhm et al., 2010, Chance et al., 2007, Councell et al., 1997). Concentrations of IO_3^- increase as bacterial influence decreases with depth in the water column. In higher latitudes, which encompasses much of the GP17-OCE stations, upwelling from IO_3^--rich deep waters to the surface (i.e. UCDW/LCDW) results in uniform concentrations of IO_3^- throughout the water column, settling around 400 nM for the entire depth profile at these stations. These consistent profiles (Chapter 2,

Figure 2.8) mean that it is difficult to use "excess" concentrations of IO_3^- across the transect as a TEI tracer of water mass movement.

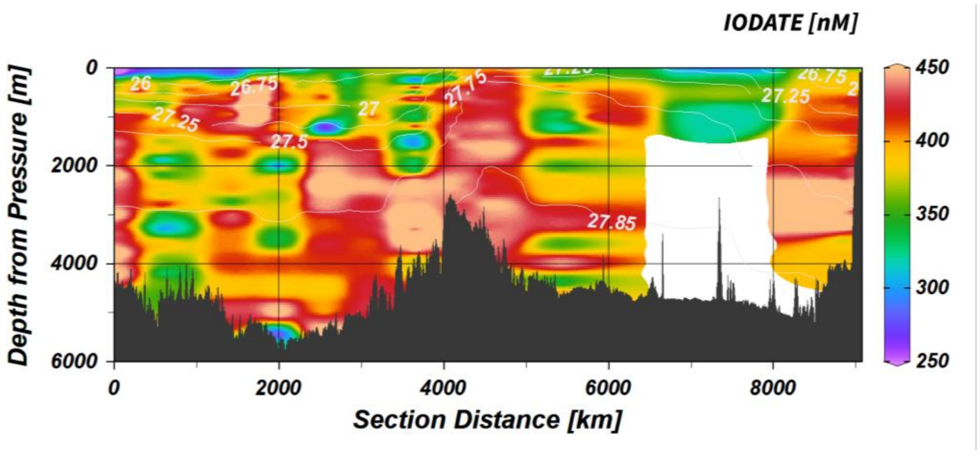

Figure 3.10 Measured Iodate across the GP17-OCE transect.

Contributions of semi-conservative TEIs such as IO_3^- to water masses can be important tracers of water mass movement and mixing. In low oxygen waters, low concentrations of IO_3^- have been used to measure the extent of OMZs and associated water masses (13CW) (Evans et al., 2020). Evans et al., 2020 indicates that increasing concentrations of IO_3^- indicate mixing with higher-oxygen waters (NEPIW), and signal the end of the area of influence of the OMZ. Concentrations of IO_3^- were measured in 24 depth profiles and across the well-oxygenated surface of the GP17-OCE transect. Decreases in surface IO_3^- concentrations are prevalent at low-latitude stations near 20ºS and show a "typical" IO_3^- profile (Bluhm et al., 2010). At higher latitudes, this decrease in surface IO_3^- concentrations likely caused by prevalent biogeochemical cycling by diatoms and bacteria such as *Syneccococus* and *Prochlorococcus* (Hepach et al., 2020) is overridden by intense upwelling of IO_3^- rich deep waters, and the profile becomes uniform at about 400 nM from surface to depth.

Unfortunately, the inherent nature of uniformly high measured IO_3^- concentrations throughout the water column at high latitudes in GP17-OCE means that a change in concentration of IO_3^- in surface waters as they move north to form AAIW could not be determined. It is likely that I^-, as it is even more conservative than IO_3^- because of known slow rate of oxidation to IO_3^- (Schnur et al., 2024, Hardisty et al., 2021), may be an even better tracker of water mass formation and movement in oxygenated South Pacific waters. Future measurements of these values from the GP17-OCE stations will aid in this determination.

Predicted IO_3^- for the South Pacific was calculated using a linear mixed-effects model that includes consideration of IO_3^- removed by aerobic respiration and the contributions of IO_3^- to each water mass as determined by the actual amount of IO_3^- measured and contained in those water masses, a value that differs with depth and station across the entire transect (Figure 3.11). Predicted IO_3^- is plotted against our observed IO_3^- values in Figure 3.11, and demonstrates the invariable nature of measured concentrations across the sample region. Measured IO_3^- shows to be, on average, about ±63 nM from predicted IO_3^- (Figure 3.11).

In a linear mixing model (LMM), predicted values, if predicted correctly, should exhibit a 1:1 ratio with measured values across the entire dataset. Deviations from this 1:1 ratio could indicate high residual error in the model. The distribution of predicted vs measured IO_3^- plotted here (Figure 3.11) violates the 1:1 ratio and is likely due to missing random effects (unmodeled sources of variance) from the model, for which distributional assumptions cannot be easily checked and which have more serious consequences for LMM than for linear models (Schielzeth et al., 2020), thus creating a bad fit. The fixed effects used in the LMM for prediction of IO_3^- are: 1) the water mass fractions of the eight defined water masses of GP17-OCE, 2) values of aerobic respiration as defined by the OMPA, and 3) the measured IO_3^- concentrations across the transect. Effects that vary randomly across a population that may be affecting the fit of the models include varying temperature, salinity, and nutrient concentrations across the transect. The effects of changing concentrations of semi-conservative nutrients such as phosphate, nitrate, and silicate, and larger effects of changing temperature and salinity across the expansive transect are not currently factored into this model, and, if included, may account for some observed scatter and violation of the 1:1 ratio, as any one of these might be a "higher level" random effect that causes cascading down to residuals (Schielzeth et al., 2020).

We can use the plotted results of the LMM to make qualitative predictions about the factors controlling IO_3^- distribution in the South Pacific. The variance of the fixed effects here (i.e. measured IO_3^- concentrations) is larger than random effects predicted. Inflated standard errors are reported for most of the more surface water masses (Table 3.6), including AASW, SAMW, STMW, UCDW, and, interestingly, the deeper PDW. This might predict that there is strong mixing or other factors, such as unaccounted for *in situ* oxidation or reduction of iodine found in measured samples that is skewing the model. Inclusion of more effects may serve to better inform the model and create a better fit.

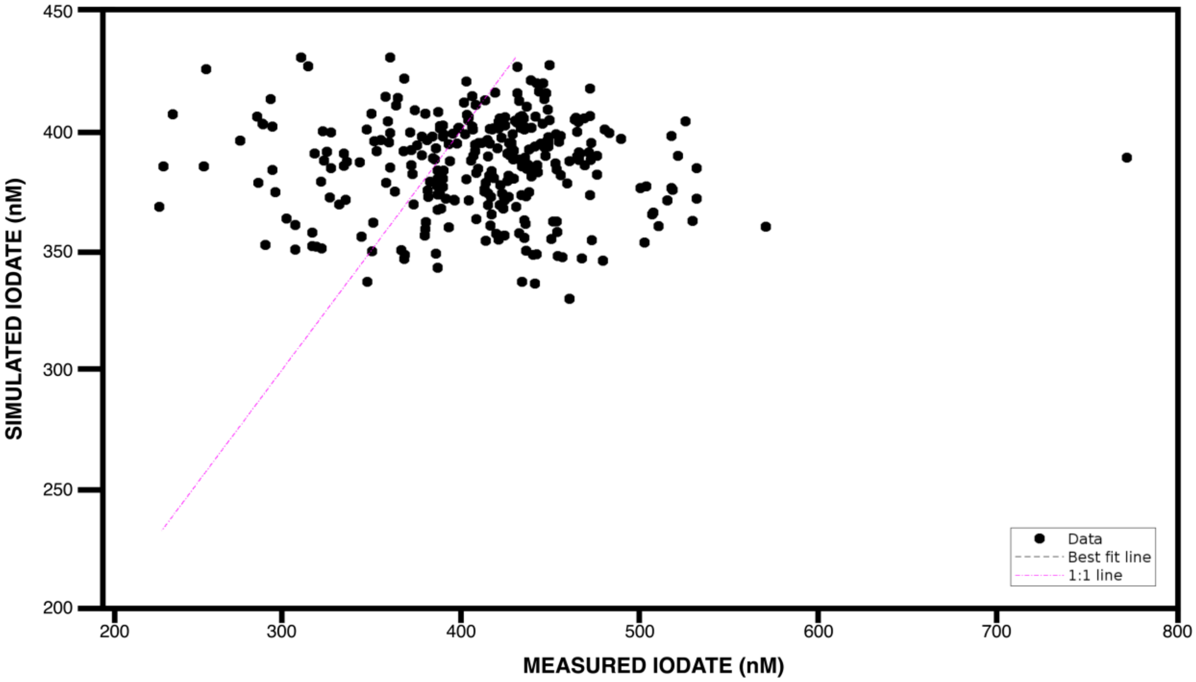

Figure 3.11 Measured IO_3^- values (nM) plotted against predicted IO_3^- values calculated using a linear mixed effect model (LMM) from the water mass fractions calculated in pyOMPA and the results of aerobic respiration.

Water Mass	**Standard Error**
Antarctic Intermediate Water	17.58
Subantarctic Mode Water	38.66
Antarctic Surface Water	64.99
Antarctic Bottom Water	12.82
Pacific Deep Water	41.46
Lower Circumpolar Deep Water	17.34
Upper Circumpolar Deep Water	68.47
Southern Tropical Mode Water	44.32

Table 3.6 Standard error for predicted IO_3^- in each water mass in GP17-OCE OMPA. Higher values may indicate missing random effects that could lead to a bad fit for the LMM.

3.5.3.3 Other non-conservative processes impacting distribution

The largest source of other non-conservative processes impacting distribution of nutrients, including IO_3^-, throughout the cruise transect is hydrothermal vent influence. There are two known areas of hydrothermal vent influence in the GP17-OCE transect: the first is at stations 18 and 20 (-56.30°S, -145.28°W and -57.60°S, -144.85°W), and the second is near the coat of Chile, at stations 35 and 37 (-54.35°S, -76.55°W and -53.50°S, -75.75°W). Hydrothermal vents are thought to influence iodine values through reactions with manganese, and IO_3^- values at stations 18 and 25 are reported slightly higher than their surrounding counterparts (~450 nM average). The difference, however, is not extremely significant and does not allow for further calculations of water mass movement. No clear trend in [IO_3^-] at all hydrothermal vent stations is observed.

Measurements of other nutrients at these hydrothermal vent sites also show uncharacteristic variability that leads to outliers in the hydrographic data, cut for pyOMPA (Figure 3.3). Specifically, hydrothermal vent influence may correlate with several areas of outlying points that were cut separately from surface values for calculation of the OPMA and consideration of low residuals. These values accounted for less than 5% of all data points used in the water mass analysis.

Benthic sources of iodide (I^-) may impact values of total iodine as the transect moves towards the coast of Chile. Measurement of these values and the values of total iodine (iodate plus iodide), including what could be defined as “excess iodine” (Moriyasu et al., 2020) could be useful for discerning trends of iodine off the coast, near the sea floor with depth profiles, and possible rates of water mass movement if these profiles show variability with depth. These measurements would be a further step in understanding if iodine can be used as a conservative tracer for water mass subduction throughout the open ocean.

3.6: Conclusion

With this calculation of a single extended pyOMPA of the Southern Pacific Ocean, we aimed to quantify water mass contributions along the entire GP17-OCE transect. We identified eight major water masses along the GP17-OCE transect throughout the water column below a depth of 250 m which was used to define the difficult-to-delineate surface waters of the transect. Three of these water masses were surface water masses, with two edgemember surface water masses contributing little to the overall waters that were described using this water mass analysis, but whose endmembers provided crucial definition of the surrounding waters and deeper water masses within the transect. The other five water masses were intermediate and deep waters of the Pacific, each delimited to specific areas of the basin by their unique densities and nutrient makeup. Where water masses were intersected twice, it was found that a single forming region was established for each, so that a single set of endmembers correctly and distinctly defined each water mass without need for a second set for any of the water masses transected here. Calculated aerobic respiration rates showed positive remineralization throughout the water column with the exception of the surface where oxygen utilization is high and available nutrients are low as microbial activity is prevalent.

The contribution of iodine in these water masses and tracking its movement through subduction northward by Pacific Ocean basin waters is difficult to establish, mainly because of uniform concentrations of IO_3^- throughout the water column at high latitudes, which, when subducted to intermediate waters, show a very similar concentration in low latitude surface waters that is expected in higher latitude deep waters. Physical mixing may play a major role in observed iodine speciation, however, these values must be tracked in another way in order to better understand the movement of TEIs through water mass movement in the South Pacific basin.

REFERENCES

Aoki, S., Takahashi, T., Yamazaki, K., Hirano, D., Ono, K., Kusahara, K., Tamura, T., & Williams, G. D. (2022). Warm surface waters increase Antarctic ice shelf melt and delay dense water formation. *Communications Earth and Environment*, *3*(1). https://doi.org/10.1038/s43247-022-00456-z

Avanti Shrikumar, Rian Lawrence, Karen L Casciotti. PYOMPA version 0.3: Technical Note. ESS Open Archive .May 13, 2021.

Baker, L. E., Mashayek, A., & Naveira Garabato, A. C. (2023). Boundary Upwelling of Antarctic Bottom Water by Topographic Turbulence. *AGU Advances*, *4*(5). https://doi.org/10.1029/2022AV000858

Bluhm, K., Croot, P., Wuttig, K., & Lochte, K. (2010). Transformation of iodate to iodide in marine phytoplankton driven by cell senescence. *Aquatic Biology*. https://doi.org/10.3354/ab00284

Bluhm, K., Croot, P. L., Huhn, O., Rohardt, G., & Lochte, K. (2011). Distribution of iodide and iodate in the Atlantic sector of the southern ocean during austral summer. *Deep-Sea Research Part II: Topical Studies in Oceanography*. https://doi.org/10.1016/j.dsr2.2011.02.002

Bostock, H. C., Opdyke, B. N., & Williams, M. J. M. (2010). Characterising the intermediate depth waters of the Pacific Ocean using δ13C and other geochemical tracers. *Deep-Sea Research Part I: Oceanographic Research Papers*, *57*(7). https://doi.org/10.1016/j.dsr.2010.04.005

Bostock, H. C., Sutton, P. J., Williams, M. J. M., & Opdyke, B. N. (2013). Reviewing the circulation and mixing of Antarctic Intermediate Water in the South Pacific using evidence from geochemical tracers and Argo float trajectories. *Deep-Sea Research Part I: Oceanographic Research Papers*, *73*. https://doi.org/10.1016/j.dsr.2012.11.007

Boulahdid, M., & Minster, J. F. (1989). Oxygen consumption and nutrient regeneration ratios along isopycnal horizons in the Pacific Ocean. *Marine Chemistry*, *26*(2). https://doi.org/10.1016/0304-4203(89)90057-1

Brand, S. V. S., Prend, C. J., & Talley, L. D. (2023). Modification of North Atlantic Deep Water by Pacific/Upper Circumpolar Deep Water in the Argentine Basin. *Geophysical Research Letters*, *50*(2). https://doi.org/10.1029/2022GL099419

Broecker, W. S., Peacock, S. L., Walker, S., Weiss, R., Fahrbach, E., Schroeder, M., Mikolajewicz, U., Heinze, C., Key, R., Peng, T. H., & Rubin, S. (1998). How much deep water is formed in the Southern Ocean? *Journal of Geophysical Research: Solid Earth*, *103*(C8). https://doi.org/10.1029/98jc00248

Bushinsky, S. M., & Cerovečki, I. (2023). Subantarctic Mode Water Biogeochemical Formation Properties and Interannual Variability. *AGU Advances*, *4*(2). https://doi.org/10.1029/2022AV000722

Carter, B. R., Talley, L. D., & Dickson, A. G. (2014). Mixing and remineralization in waters detrained from the surface into Subantarctic Mode Water and Antarctic Intermediate Water in the southeastern Pacific. *Journal of Geophysical Research: Oceans*, *119*(6). https://doi.org/10.1002/2013JC009355

Chance, R., Baker, A. R., Carpenter, L., & Jickells, T. D. (2014). The distribution of iodide at the sea surface. In *Environmental Sciences: Processes and Impacts*. https://doi.org/10.1039/c4em00139g

Chance, R., Weston, K., Baker, A. R., Hughes, C., Malin, G., Carpenter, L., Meredith, M. P., Clarke, A., Jickells, T. D., Mann, P., & Rossetti, H. (2010). Seasonal and interannual variation of dissolved iodine speciation at a coastal Antarctic site. *Marine Chemistry*. https://doi.org/10.1016/j.marchem.2009.11.009

Chance, R., Malin, G., Jickells, T., & Baker, A. R. (2007). Reduction of iodate to iodide by cold water diatom cultures. *Marine Chemistry*. https://doi.org/10.1016/j.marchem.2006.06.008

Councell, T. B., Landa, E. R., & Lovley, D. R. (1997). Microbial reduction of iodate. *Water, Air, and Soil Pollution*. https://doi.org/10.1023/A:1018370423790

Demuynck, P., Tyrrell, T., Naveira Garabato, A., Christopher Moore, M., & Peter Martin, A. (2020). Spatial variations in silicate-to-nitrate ratios in Southern Ocean surface waters are controlled in the short term by physics rather than biology. *Biogeosciences*, *17*(8). https://doi.org/10.5194/bg-17-2289-2020

Evans, D. G., Zika, J. D., Naveira Garabato, A. C., & Nurser, A. J. G. (2018). The Cold Transit of Southern Ocean Upwelling. *Geophysical Research Letters*, *45*(24). https://doi.org/10.1029/2018GL079986

Evans, N., Boles, E., Kwiecinski, J. V., Mullen, S., Wolf, M., Devol, A. H., Moriyasu, R., Nam, S. H., Babbin, A. R., & Moffett, J. W. (2020). The role of water masses in shaping the distribution of redox active compounds in the Eastern Tropical North Pacific oxygen deficient zone and influencing low oxygen concentrations in the eastern Pacific Ocean. *Limnology and Oceanography*, *65*(8), 1688–1705. https://doi.org/10.1002/LNO.11412

Freeman, N. M., Lovenduski, N. S., Munro, D. R., Krumhardt, K. M., Lindsay, K., Long, M. C., & Maclennan, M. (2018). The Variable and Changing Southern Ocean Silicate Front: Insights From the CESM Large Ensemble. *Global Biogeochemical Cycles*, *32*(5). https://doi.org/10.1029/2017GB005816

Foppert A, Bestley S, Shadwick EH, Klocker A, Vives CR, Liniger G and Westwood KJ (2024) Observed water-mass characteristics and circulation off Prydz Bay, East Antarctica. Front. Mar. Sci. 11:1456207. doi: 10.3389/fmars.2024.1456207

Granger, J., Sigman, D. M., Gagnon, J., Tremblay, J. E., & Mucci, A. (2018). On the Properties of the Arctic Halocline and Deep Water Masses of the Canada Basin from Nitrate Isotope Ratios. *Journal of Geophysical Research: Oceans*, *123*(8). https://doi.org/10.1029/2018JC014110

Hamilton, L. J. (2006). Structure of the Subtropical Front in the Tasman Sea. *Deep-Sea Research Part I: Oceanographic Research Papers*, *53*(12). https://doi.org/10.1016/j.dsr.2006.08.013

Hardisty, D. S., Horner, T. J., Wankel, S. D., Blusztajn, J., & Nielsen, S. G. (2020). Experimental observations of marine iodide oxidation using a novel sparge-interface MC-ICP-MS technique. *Chemical Geology*. https://doi.org/10.1016/j.chemgeo.2019.119360

Hardisty, D. S., Horner, T. J., Evans, N., Moriyasu, R., Babbin, A. R., Wankel, S. D., Moffett, J. W., & Nielsen, S. G. (2021). Limited iodate reduction in shipboard seawater incubations from the Eastern Tropical North Pacific oxygen deficient zone. *Earth and Planetary Science Letters*, *554*, 116676. https://doi.org/10.1016/j.epsl.2020.116676

Hanawa, K., & D.Talley, L. (2001). Chapter 5.4 Mode waters. *International Geophysics*, *77*(C). https://doi.org/10.1016/S0074-6142(01)80129-7

Hartin, C. A., Fine, R. A., Sloyan, B. M., Talley, L. D., Chereskin, T. K., & Happell, J. (2011). Formation rates of Subantarctic mode water and Antarctic intermediate water within the South Pacific. *Deep-Sea Research Part I: Oceanographic Research Papers*, *58*(5). https://doi.org/10.1016/j.dsr.2011.02.010

He, P., Hou, X., Aldahan, A., Possnert, G., & Yi, P. (2013). Iodine isotopes species fingerprinting environmental conditions in surface water along the northeastern Atlantic Ocean. *Scientific Reports 2013 3:1*, *3*(1), 1–8. https://doi.org/10.1038/srep02685

Hepach, H., Hughes, C., Hogg, K., Collings, S., & Chance, R. (2020). Senescence as the main driver of iodide release from a diverse range of marine phytoplankton. *Biogeosciences*. https://doi.org/10.5194/bg-17-2453-2020

Hung, C. C., Wong, G. T. F., & Dunstan, W. M. (2005). Iodate reduction activity in nitrate reductase extracts from marine phytoplankton. *Bulletin of Marine Science*, *76*(1)

Karstensen, J., & Quadfasel, D. (2002). Formation of Southern Hemisphere thermocline waters: Water mass conversion and subduction. *Journal of Physical Oceanography*, *32*(11). https://doi.org/10.1175/1520-0485(2002)032<3020:FOSHTW>2.0.CO;2

Karstensen, J., & Tomczak, M. (1998). Age determination of mixed water masses using CFC and oxygen data. *Journal of Geophysical Research: Oceans*, *103*(C9). https://doi.org/10.1029/98JC00889

Jenkins, W. J., Smethie, W. M., Boyle, E. A., & Cutter, G. A. (2015). Water mass analysis for the U.S. GEOTRACES (GA03) North Atlantic sections. *Deep Sea Research Part II: Topical Studies in Oceanography*, *116*, 6–20. https://doi.org/10.1016/J.DSR2.2014.11.018

Jia, R., Chen, M., Pan, H., Zeng, J., Zhu, J., Liu, X., Zheng, M., & Qiu, Y. (2022). Freshwater components track the export of dense shelf water from Prydz Bay, Antarctica. *Deep-Sea Research Part II: Topical Studies in Oceanography*, *196*. https://doi.org/10.1016/j.dsr2.2022.105023

Li, Y. H., & Peng, T. H. (2002). Latitudinal change of remineralization ratios in the oceans and its implication for nutrient cycles. *Global Biogeochemical Cycles*, *16*(4). https://doi.org/10.1029/2001gb001828.

Li, Z., Groeskamp, S., Cerovečki, I., & England, M. H. (2022). The Origin and Fate of Antarctic Intermediate Water in the Southern Ocean. *Journal of Physical Oceanography*, *52*(11). https://doi.org/10.1175/jpo-d-21-0221.1

Li, Z., England, M. H., & Groeskamp, S. (2023). Recent acceleration in global ocean heat accumulation by mode and intermediate waters. *Nature Communications*, *14*(1). https://doi.org/10.1038/s41467-023-42468-z

Liu, M., & Tanhua, T. (2021). Water masses in the Atlantic Ocean: Characteristics and distributions. *Ocean Science*, *17*(2). https://doi.org/10.5194/os-17-463-2021

Llanillo, P. J., Karstensen, J., Pelegrí, J. L., & Stramma, L. (2013). Physical and biogeochemical forcing of oxygen and nitrate changes during el niño/el viejo and la niña/la vieja upper-ocean phases in the tropical eastern south pacific along 86 w. *Biogeosciences*, *10*(10). https://doi.org/10.5194/bg-10-6339-2013

Luther, G. W., Wu, J., & Cullen, J. B. (1995). *Redox Chemistry of Iodine in Seawater*. 135–155. https://doi.org/10.1021/BA-1995-0244.CH006

Luther, G. W. I. (2023). Review on the physical chemistry of iodine transformations in the oceans. *Frontiers in Marine Science*, *10*, 20. https://doi.org/10.3389/FMARS.2023.1085618

Maamaatuaiahutapu, K., Garçon, V. C., Provost, C., Boulahdid, M., & Osiroff, A. P. (1992). Brazil-Malvinas Confluence: Water mass composition. Journal of Geophysical Research: Oceans, 97(C6), 9493–9505. https://doi.org/10.1029/92JC00484

Meijers, A. J. S., Cerovečki, I., King, B. A., & Tamsitt, V. (2019). A See-Saw in Pacific Subantarctic Mode Water Formation Driven by Atmospheric Modes. *Geophysical Research Letters*, *46*(22). https://doi.org/10.1029/2019GL085280

Moisan, T. A., Dunstan, W. M., Udomkit, A., & Wong, G. T. F. (1994). THE UPTAKE OF IODATE BY MARINE PHYTOPLANKTON. *Journal of Phycology*. https://doi.org/10.1111/j.0022-3646.1994.00580.x

Moriyasu, R., Evans, N., Bolster, K. M., Hardisty, D. S., & Moffett, J. W. (2020). The Distribution and Redox Speciation of Iodine in the Eastern Tropical North Pacific Ocean. *Global Biogeochemical Cycles*, *34*(2), e2019GB006302. https://doi.org/10.1029/2019GB006302

Moriyasu, R., Bolster, K. M., Hardisty, D. S., Kadko, D. C., Stephens, M. P., & Moffett, J. W. (2023). Meridional Survey of the Central Pacific Reveals Iodide Accumulation in Equatorial Surface Waters and Benthic Sources in the Abyssal Plain. *Global Biogeochemical Cycles*, *37*(3). https://doi.org/10.1029/2021GB007300

Oka, E., & Suga, T. (2003). Formation region of North Pacific subtropical mode water in the late winter of 2003. *Geophysical Research Letters*, *30*(23). https://doi.org/10.1029/2003GL018581

Peters, B. D., Jenkins, W. J., Swift, J. H., German, C. R., Moffett, J. W., Cutter, G. A., Brzezinski, M. A., & Casciotti, K. L. (2018). Water mass analysis of the 2013 US GEOTRACES eastern Pacific zonal transect (GP16). *Marine Chemistry*, *201*, 6–19. https://doi.org/10.1016/J.MARCHEM.2017.09.007

Piñango, A., Kerr, R., Orselli, I. B. M., Carvalho, A. da C. O., Azar, E., Karstensen, J., & Garcia, C. A. E. (2022). Ocean Acidification and Long-Term Changes in the Carbonate System Properties of the South Atlantic Ocean. *Global Biogeochemical Cycles*, *36*(9). https://doi.org/10.1029/2021GB007196

Proceedings of the Ocean Drilling Program, 181 Scientific Results. (2004). In *Proceedings of the Ocean Drilling Program, 181 Scientific Results*. https://doi.org/10.2973/odp.proc.sr.181.2004.

Qu, T., Gao, S., Fukumori, I., Fine, R. A., & Lindstrom, E. J. (2008). Subduction of South Pacific waters. *Geophysical Research Letters*, *35*(2). https://doi.org/10.1029/2007GL032605

Rainville, L., Jayne, S. R., McClean, J. L., & Maltrud, M. E. (2007). Formation of Subtropical Mode Water in a high-resolution ocean simulation of the Kuroshio Extension region. *Ocean Modelling*, *17*(4). https://doi.org/10.1016/j.ocemod.2007.03.002

Ramadhan, A., Marshall, J., Meneghello, G., Illari, L., & Speer, K. (2022). Observations of Upwelling and Downwelling Around Antarctica Mediated by Sea Ice. Frontiers in Marine Science, 9. https://doi.org/10.3389/fmars.2022.864808

Reyes-Macaya, D., Hoogakker, B., Martínez-Méndez, G., Llanillo, P. J., Grasse, P., Mohtadi, M., Mix, A., Leng, M. J., Struck, U., McCorkle, D. C., Troncoso, M., Gayo, E. M., Lange, C. B., Farias, L., Carhuapoma, W., Graco, M., Cornejo-D'Ottone, M., de Pol Holz, R., Fernandez, C., … Hebbeln, D. (2022). Isotopic Characterization of Water Masses in the Southeast Pacific Region: Paleoceanographic Implications. *Journal of Geophysical Research: Oceans*, *127*(1). https://doi.org/10.1029/2021JC017525

Rodehacke, C. B., Hellmer, H. H., Beckmann, A., & Roether, W. (2007). Formation and spreading of Antarctic deep and bottom waters inferred from a chlorofluorocarbon (CFC) simulation. *Journal of Geophysical Research: Oceans*, *112*(9). https://doi.org/10.1029/2006JC003884

Roemmich, D., & Cornuelle, B. (1992). The subtropical mode waters of the South Pacific Ocean. *Journal of Physical Oceanography*, *22*(10). https://doi.org/10.1175/1520-0485(1992)022<1178:TSMWOT>2.0.CO;2

Rubin, S. I., Takahashi, T., Chipman, D. W., & Goddard, J. G. (1998). Primary productivity and nutrient utilization ratios in the pacific sector of the Southern Ocean based on seasonal changes in seawater chemistry. *Deep-Sea Research Part I: Oceanographic Research Papers*, *45*(8). https://doi.org/10.1016/S0967-0637(98)00021-1

Sanders, R. N. C., Meijers, A. J. S., Holland, P. R., & Naveira Garabato, A. C. (2023). Sea Ice-Driven Variability in the Pacific Subantarctic Mode Water Formation Regions. *Journal of Geophysical Research: Oceans*, *128*(12). https://doi.org/10.1029/2023JC020006

Schnur AA, Sutherland KM, Hansel CM and Hardisty DS (2024) Rates and pathways of iodine speciation transformations at the Bermuda Atlantic Time Series. Front. Mar. Sci. 10:1272870. doi: 10.3389/fmars.2023.1272870

Schielzeth, H., Dingemanse, N. J., Nakagawa, S., Westneat, D. F., Allegue, H., Teplitsky, C., Réale, D., Dochtermann, N. A., Garamszegi, L. Z., & Araya-Ajoy, Y. G. (2020). The Robustness of linear mixed effects models to violations of distributional assumptions. *Methods in Ecology and Evolution*, *11*(9). https://doi.org/10.1111/2041-210X.13434

Segschneider, J., & Bendtsen, J. (2013). Temperature-dependent remineralization in a warming ocean increases surface pCO2 through changes in marine ecosystem composition. *Global Biogeochemical Cycles*, *27*(4). https://doi.org/10.1002/2013GB004684

Sigman, D. M., & Hain, M. P. (2012). The Biological Productivity of the Ocean | Learn Science at Scitable. *Nature Education Knowledge*, *3*(6).

Silva, N., Rojas, N., & Fedele, A. (2009). Water masses in the Humboldt Current System: Properties, distribution, and the nitrate deficit as a chemical water mass tracer for Equatorial Subsurface Water off Chile. *Deep Sea Research Part II: Topical Studies in Oceanography*, *56*(16), 1004–1020. https://doi.org/10.1016/J.DSR2.2008.12.013

Solodoch, A., Stewart, A. L., Hogg, A. M. C., Morrison, A. K., Kiss, A. E., Thompson, A. F., Purkey, S. G., & Cimoli, L. (2022). How Does Antarctic Bottom Water Cross the Southern Ocean? *Geophysical Research Letters*, *49*(7). https://doi.org/10.1029/2021GL097211

Talley, L. D., Pickard, G. L., Emery, W. J., & Swift, J. H. (2011). Descriptive physical oceanography: An introduction: Sixth edition. In *Descriptive Physical Oceanography: An Introduction: Sixth Edition*. https://doi.org/10.1016/C2009-0-24322-4

Talley, L.D. 2013. Closure of the global overturning circulation through the Indian, Pacific, and Southern Oceans: Schematics and transports. Oceanography 26(1):80–97, http://dx.doi.org/10.5670/oceanog.2013.07.

Tsunogai, S., & Henmi, T. (1971). Iodine in the surface water of the ocean. *Journal of the Oceanographical Society of Japan*. https://doi.org/10.1007/BF02109332

Twining, B. S., Fitzsimmons, J. L., & Cutter, G. A. (2023). *U.S. GEOTRACES GP17-OCE Cruise Report*.

Wadley, M. R., Stevens, D. P., Jickells, T. D., Hughes, C., Chance, R., Hepach, H., Tinel, L., & Carpenter, L. J. (2020). A Global Model for Iodine Speciation in the Upper Ocean. *Global Biogeochemical Cycles*, *34*(9), e2019GB006467. https://doi.org/10.1029/2019GB006467

Waltemathe, H., Struve., T., Rehbein, M., Pahnke, K. (2024). Influence of water mass mixing and hydrothermal processes on the distribution of dissolved Nd isotopes and concentrations in the South Pacific. *Earth and Planetary Science Letters*, 642. https://doi.org/10.1016/j.epsl.2024.118846

Webb, P. (2017). Introduction to Oceanography: Dissolved Gasses: Oxygen. *Roger Williams University*.

Webb, P. (2017). Introduction to Oceanography. In Roger Williams University. https://rwu.pressbooks.pub/webboceanography/.

Whitmore, L. M., Pasqualini, A., Newton, R., & Shiller, A. M. (2020). Gallium: A New Tracer of Pacific Water in the Arctic Ocean. *Journal of Geophysical Research: Oceans*, *125*(7). https://doi.org/10.1029/2019JC015842

Wong, G. T. F., & Hung, C. C. (2001). Speciation of dissolved iodine: Integrating nitrate uptake over time in the oceans. *Continental Shelf Research*. https://doi.org/10.1016/S0278-4343(00)00086-8

Yamazaki, K., Katsumata, K., Hirano, D., Nomura, D., Sasaki, H., Murase, H., Aoki, S. (2024). Revisiting circulation and water masses over the East Antarctic margin (80–150°E). *Progress in Oceanography* (225). https://doi.org/10.1016/j.pocean.2024.103285

Yuan-Huili, D., Karl, D. M., Winn, C. D., Mackenzie, F. T., & Gans, K. (2000). Remineralization ratios in the subtropical north pacific gyre. *Aquatic Geochemistry*, *6*(1). https://doi.org/10.1023/A:1009676300859

Zenk, W., Siedler, G., Ishida, A., Holfort, J., Kashino, Y., Kuroda, Y., Miyama, T., & Müller, T. J. (2005). Pathways and variability of the Antarctic Intermediate Water in the western equatorial Pacific Ocean. *Progress in Oceanography*, *67*(1–2). https://doi.org/10.1016/j.pocean.2005.05.003

Zhang, J., Liu, Q., Bai, L. li, & Matsuno, T. (2018). Water mass analysis and contribution estimation using heavy rare earth elements: Significance of Kuroshio intermediate water to Central East China Sea shelf water. *Marine Chemistry*, *204*. https://doi.org/10.1016/j.marchem.2018.07.011

Zheng, X. Y., Plancherel, Y., Saito, M. A., Scott, P. M., & Henderson, G. M. (2016). Rare earth elements (REEs) in the tropical South Atlantic and quantitative deconvolution of their non-conservative behavior. *Geochimica et Cosmochimica Acta*, *177*. https://doi.org/10.1016/j.gca.2016.01.018

Zhou, Q., Hattermann, T., Nøst, O. A., Biuw, M., Kovacs, K. M., & Lydersen, C. (2014). Wind-driven spreading of fresh surface water beneath ice shelves in the Eastern Weddell Sea. *Journal of Geophysical Research: Oceans*, *119*(6). https://doi.org/10.1002/2013JC009556

Zhou, S., Meijers, A. J. S., Meredith, M. P., Abrahamsen, E. P., Holland, P. R., Silvano, A., Sallée, J. B., & Østerhus, S. (2023). Slowdown of Antarctic Bottom Water export driven by climatic wind and sea-ice changes. *Nature Climate Change*, *13*(7). https://doi.org/10.1038/s41558-023-01695-4

APPENDIX

Station	Bottom Depth (m)	Station	Bottom Depth (m)
1	4242	**21**	FISH only
2	4291	**22**	3427
3	4659	**23**	3907
4	4602	**24**	4476
5	4532	**25**	4590
6	5129	**26**	4221
7	5138	**27**	4741
8	5635	**28**	FISH only
9	5575	**29**	4688
10	5356	**30**	4495
11	5130	**31**	FISH only
12	5057	**32**	5034
13	4688	**33**	FISH only
14	3987	**34**	4067
15	3661	**35**	3999
16	3228	**36**	4142
17	FISH only	**37**	3345
18	2596	**38**	93
19	FISH only		
20	3131		

Supplementary Table 3.1 Bottom depths (m) of depth profile stations along GP17-OCE transect. All stations designated "FISH only" have a single reading at 3 m and no corresponding depth profile.

Study	CT	SA	Phosphate	Nitrate	Oxygen	Silica
Reyes-Macaya et al., 2021	24	24	2	2	7	3.5
Evans et al., 2020	24	24	2	7	-	-
Karstensen and Tomczak 1999	24	24	2	2	7	2
Llanillo et al., 2013	24	24	7	7	7	3.5
Evans et al., 2023*	12	8	6	4	2	2
Lawrence et al., 2022* (intermediate/deep)	56	80	5	5	1	3
This study	12	8	6	4	2	2

Supplementary Table 3.2 Comparisons of weighting from previous OMPA studies. Weightings used in this study are taken from the Evans et al., 2023 study, which used the same pyOMPA format in the Pacific Ocean Basin that is used for this water mass analysis. '*' indicates pyOMPA used in study.

Study	Phosphate	Nitrate	Oxygen	Silica	Area
Rubin et al., 1998	1	11.8-14.2			South Pacific
Li et al., 2000	1	12-14	161-179		HOT
Li and Peng 2002	1	14-16	128-138		Pacific Ocean
WOCE data 2001	1	13.5-14.5	126-146		South Pacific (10°S-70°S)
Carter et al., 2014	1	14.9-16.1	82-126		Southeast Pacific
Boulahdid and Minster 1989	1	14.7	118		South Pacific
Demuynck et al., 2020				~16, N:Si is 1:1	Southern Ocean
Freeman et al., 2018				~16, N:Si is 1:1	Southern Ocean

Supplementary Table 3.3 Comparisons of remineralization ratios from previous Pacific Ocean basin literature.

CONCLUSIONS

The understanding of iodine redox species distribution in the surface ocean is important for consideration of its use in climatological models and its use in a paleoredox proxy for understanding distribution of oxygen in ancient oceans. The measurement of modern concentrations of I^- and IO_3^- in the world oceans, especially those that are currently under characterized, can give us a sense of the processes that govern distribution of trace elements such as iodine and the flow of oxygen through marine systems. As oxidized iodine as IO_3^- is secluded into carbonates and stored can be used as an ancient record of ocean oxygenation, insight into the rates and methods of *in situ* IO_3^- formation helps us to discern how and where IO_3^- is likely initially formed. As rates of I^- oxidation to IO_3^- directly are known to be slow, and likely found only in "hotspots" of formation such as areas of high biogeochemical activity, ODZ's, and pore waters (Schnur et al., 2024), an additional understanding of the *ex situ* movement of ocean waters that may carry IO_3^- from formation zones into larger oceanic systems is also necessary.

This dissertation explores several possible rates and mechanisms of IO_3^- formation and distribution throughout two ocean systems; first, *in situ* rates of IO_3^- formation with possible formation by ROS in the oligotrophic Bermuda Atlantic Time Series (BATS) in the Atlantic Ocean, and second, *ex situ* methods of I^- and IO_3^- distribution throughout the entire Pacific Ocean Basin through measurement of iodine concentrations across the GEOTRACES GP15 and GP17-OCE cruise transects.

Chapter 1 presented insights into *in situ* rates and pathways of IO_3^- formation in surface ocean seawater, with a focus on the role of reactive oxygen species was given to IO_3^- formation in natural systems. In order to track I^- oxidation to IO_3^-, the radioactive tracer ^{129}I was added to incubations of natural seawater to track its incorporation into systems with an abundance of naturally occurring ^{127}I through $^{129}I/^{127}I$ ratios of I^-, IO_3^-, and DOI, from the Bermuda Atlantic Time Series (BATS) in the Atlantic Ocean. As iodine redox species are in disequilibrium at the sea surface, where there is an abundance of I^- that would not be expected if oxygen was the leading oxidant of I^- to IO_3^-, it was important to consider other mechanisms that support oxidation in natural settings, such as extracellularly-produced reactive oxygen species (ROS). Oxidation of I^- to IO_3^- by ROS had yet to be tested under ambient marine conditions, although it had previously been reported in culture (Li et al., 2014). Results showed a discernible lack of I^- oxidation to IO_3^- stimulated by ROS, with an overall slow rate of environmental oxidation of less than 2.99 nM day$^-$

[1]. Because of this slow rate of I^- oxidation, it seems likely that the bulk of IO_3^- formation is occurring in formation "hotspots", like as areas of very high biogeochemical activity, ODZ's, and in pore waters (Hardisty et al., 2021), instead of ubiquitously and commensurably throughout the ocean. Because of this, it appears likely that *ex situ* sources of transportation were likely large drivers of iodine redox species distribution throughout the ocean, a premise that was explored in Chapters 2 and 3.

Chapter 2 expands upon the idea of *ex situ* sources of water mass movement with a completion of the first full basinal transect of iodine redox species measurements through the undercharacterized Pacific Ocean at 152°W and a look into rates of upwelling and vertical diffusion in the South Pacific using the complimentary tracer ^7Be. Concentrations of I^- and IO_3^- from surface samples taken during the GP15 (Alaska to Tahiti) and GP17-OCE (Tahiti to Antarctic waters) were measured and the values compared with previous measurements of iodine from other studies of the open ocean across latitudes. The values that were measured showed good agreement with previously reported trends of iodine distribution (Chance et al., 2014, Moriyasu et al., 2023, He et al., 2013, Chance et al., 2010, Moriyasu et al., 2020, Tsunogai and Henmi 1971), and a full transect of iodine measurements was made for the Pacific Ocean. With this clarity on natural distribution, insights into the rates of upwelling and vertical diffusion, *ex situ* sources of water mass movement that could contribute to the dispersion that was captured by the transect, were explored. The tracer ^7Be was used as a tool for tracking these rates of upwelling and vertical diffusion, and a full mass balance of the Southern Pacific Ocean was obtained because of the analogous profiles of ^7Be and IO_3^- in the ocean with depth. It was found that the rate of IO_3^- flux was in range of a previous study at the Hawaii Ocean Time Series (HOT) done in the Pacific, although the iodine:carbon ratio measured in this mass balance was found to be higher than previously reported in open ocean waters (Campos et al., 1996). Even so, the results of this study point importantly towards the significance of mixing and water mass movement as a source of IO_3^- distribution, especially from deeper waters where iodine is almost completely found as IO_3^-. As these processes of upwelling and vertical diffusion are important but, in terms of basinal scale processes, are small, the next step was to consider the movement full water masses in the South Pacific and the effect of incorporated iodine into large basinal-scale movement of ocean water.

Chapter 3 dove heavily into the definition and discernment of the water masses of the South Pacific through a water mass analysis using an Optimum Multi-parameter Analysis (OMPA) tool for calculating water mass percentage of samples taken from the GP17-OCE cruise. Hydrographic data from across a latitudinal transect at 152°W and a pseudo-longitudinal transect at 67°S ending at the coast of Chile were used with a surface cutoff of 250 m to define eight water masses in the South Pacific. The definition of these water masses and visualization of their movement throughout the South Pacific Basin has major implications for understanding the movement of all conservative and semi-conservative nutrients that are incorporated into these water masses, for which we know that iodine is one. [IO_3^-] profiles measured across the transect at most high latitude stations (a majority of GP17-OCE's transect), were found to be nearly uniform at around 400 nM concentration from surface to depth. Subduction of IO_3^- by way of "excess iodine" in the water masses therefore could not be measured, as no change was visible from surface values to those in the deep.

The initial insight gained from these studies indicates that I^- oxidation to IO_3^- is slow, not expected to be aided in a significant way by ROS, and likely occurring in only in specific areas, or "hotspots" of formation, rather than ubiquitously across the world oceans. In order for the well-understood distribution of iodine redox species across latitudes to occur, it is likely that *ex situ* methods of movement are more important than previously thought. In this case, insights from the GP15 and GP17-OCE cruises show that upwelling and vertical diffusion play a role in IO_3^- movement from depth to the surface causing high concentrations of IO_3^- especially at high latitudes, and water mass movement, as it heavily influences many conservative elements in the South Pacific, likely influences the distribution of conservative IO_3^- as well as it is subducted with arctic surface waters to the deeper northern waters of the Pacific. More quantification, likely with I^- – which is more variable over depth profiles at high latitudes – may be needed.

In addition to the undercharacterization of the Pacific Ocean in regards to iodine redox species concentrations, iodine in the world ocean in general is not well characterized, and the rates of IO_3^-'s oxidation from I^- and movement throughout large scale bodies are not well understood. Further basic measurement of iodine in more areas of the worlds oceans would help tremendously in the characterization of these species, and aid in comparison of the values of rates and distribution that are already reported. As other studies have reported varying levels of I^- oxidative activity both in and outside the presence of intermediates (Fentske et al., unpublished, Ştreangă et al., 2024, Hardisty et al., 2021) and the presence of ROS (Schnur et al., 2024, Li et al., 2014), more study of the reactions of iodine in ambient conditions and, especially, a deeper examination of the importance of iodine intermediates in the oxidative process would allow for more precise understanding of IO_3^- formation in the surface ocean.

As large scale *ex situ* sources of movement seem to be the driving factor of iodine species distribution throughout the ocean, a deeper study of the incorporation of iodine, specifically I^-, into water mass forming regions would be a good step in furthering understanding of iodine's movement through ocean basins. As more is learned about the distribution of iodine and its redox species throughout the ocean, interpretations of its formation will directly impact what is known of its importance through geological history as part of atmospheric processes and a paleoredox proxy, specifically as a tracer for past oxygenation and, therefore, tracer of life on this planet.

REFERENCES

Campos M. L. A. M., Farrenkopf A. M., Jickells T. D., Luther G. W. (1996). A comparison of dissolved iodine cycling at the Bermuda Atlantic Time-series Station and Hawaii Ocean Time-series Station. Deep Sea Res. Part II: Topical Stud. Oceanography. 43, 455–466. doi: 10.1016/0967-0645(95)00100-x

Chance, R., Weston, K., Baker, A. R., Hughes, C., Malin, G., Carpenter, L., Meredith, M. P., Clarke, A., Jickells, T. D., Mann, P., & Rossetti, H. (2010). Seasonal and interannual variation of dissolved iodine speciation at a coastal Antarctic site. Marine Chemistry. https://doi.org/10.1016/j.marchem.2009.11.009

Chance, R., Baker, A. R., Carpenter, L., & Jickells, T. D. (2014). The distribution of iodide at the sea surface. In Environmental Sciences: Processes and Impacts. https://doi.org/10.1039/c4em00139g

Hardisty, D. S., Horner, T. J., Evans, N., Moriyasu, R., Babbin, A. R., Wankel, S. D., Moffett, J. W., & Nielsen, S. G. (2021). Limited iodate reduction in shipboard seawater incubations from the Eastern Tropical North Pacific oxygen deficient zone. Earth and Planetary Science Letters, 554, 116676. https://doi.org/10.1016/j.epsl.2020.116676

He, P., Hou, X., Aldahan, A., Possnert, G., & Yi, P. (2013). Iodine isotopes species fingerprinting environmental conditions in surface water along the northeastern Atlantic Ocean. Scientific Reports 2013 3:1, 3(1), 1–8. https://doi.org/10.1038/srep02685

Li H. P., Daniel B., Creeley D., Grandbois R., Zhang S., Xu C., et al. (2014). Superoxide production by a manganese-oxidizing bacterium facilitates iodide oxidation. Appl. Environ. Microbiol. 80, 2693–2699. doi: 10.1128/AEM.00400-14

Moriyasu, R., Evans, N., Bolster, K. M., Hardisty, D. S., & Moffett, J. W. (2020). The Distribution and Redox Speciation of Iodine in the Eastern Tropical North Pacific Ocean. Global Biogeochemical Cycles, 34(2), e2019GB006302. https://doi.org/10.1029/2019GB006302

Moriyasu, R., Bolster, K. M., Hardisty, D. S., Kadko, D. C., Stephens, M. P., & Moffett, J. W. (2023). Meridional Survey of the Central Pacific Reveals Iodide Accumulation in Equatorial Surface Waters and Benthic Sources in the Abyssal Plain. Global Biogeochemical Cycles, 37(3). https://doi.org/10.1029/2021GB007300

Schnur AA, Sutherland KM, Hansel CM and Hardisty DS (2024) Rates and pathways of iodine speciation transformations at the Bermuda Atlantic Time Series. Front. Mar. Sci. 10:1272870. doi: 10.3389/fmars.2023.1272870

Ştreangă I-M, Repeta DJ, Blusztajn JS and Horner TJ (2024) Speciation and cycling of iodine in the subtropical North Pacific Ocean. Front. Mar. Sci. 10:1272968. doi: 10.3389/fmars.2023.1272968

Tsunogai, S., & Henmi, T. (1971). Iodine in the surface water of the ocean. *Journal of the Oceanographical Society of Japan*. https://doi.org/10.1007/BF02109332